CHEMICAL REVIEWS

Review

pubs.acs.org/CR

Odyssey of Multivalent Cathode Materials: Open Questions and Future Challenges

Pieremanuele Canepa,*[,†,‡,@] Gopalakrishnan Sai Gautam,[†,‡,§,@] Daniel C. Hannah,[†,@] Rahul Malik,[‡] Miao Liu,[∥] Kevin G. Gallagher,[⊥] Kristin A. Persson,[∥] and Gerbrand Ceder*[,†,‡,§]

[†]Materials Science Division, Lawrence Berkeley National Laboratory, Berkeley, California 94720, United States

[‡]Department of Materials Science and Engineering, Massachusetts Institute of Technology, Cambridge, Massachusetts 02139, United States

[§]Department of Materials Science and Engineering, University of California Berkeley, California 94720, United States

[∥]Energy and Environmental Science Division, Lawrence Berkeley National Laboratory, Berkeley, California 94720, United States

[⊥]Chemical Sciences and Engineering, Argonne National Laboratory, Lemont, Illinois 60439, United States

ABSTRACT: The rapidly expanding field of nonaqueous multivalent intercalation batteries offers a promising way to overcome safety, cost, and energy density limitations of state-of-the-art Li-ion battery technology. We present a critical and rigorous analysis of the increasing volume of multivalent battery research, focusing on a wide range of intercalation cathode materials and the mechanisms of multivalent ion insertion and migration within those frameworks. The present analysis covers a wide variety of material chemistries, including chalcogenides, oxides, and polyanions, highlighting merits and challenges of each class of materials as multivalent cathodes. The review underscores the overlap of experiments and theory, ranging from charting the design metrics useful for developing the next generation of MV-cathodes to targeted in-depth studies rationalizing complex experimental results. On the basis of our critical review of the literature, we provide suggestions for future multivalent cathode studies, including a strong emphasis on the unambiguous characterization of the intercalation mechanisms.

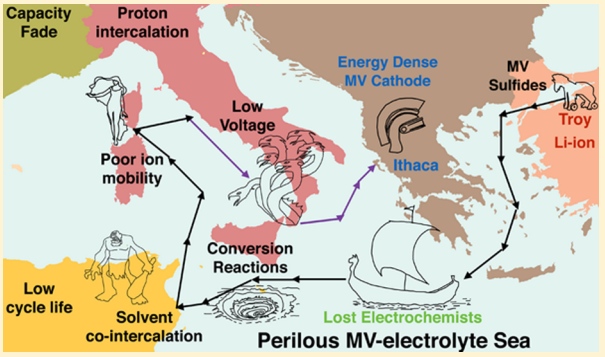

CONTENTS

Received: September 6, 2016
Published: February 13, 2017

DOI: 10.1021/acs.chemrev.6b00614
Chem. Rev. 2017, 117, 4287−4341

1. INTRODUCTION

Secondary (i.e., rechargeable) intercalation batteries convert chemical energy into electricity via three main components: the cathode (the intercalation cathode of Figure 1) where the working ion is inserted/extracted, an electrolyte transporting working ions between anode and cathode, and the anode. During the battery discharge, working ions are released at the anode and migrate to the cathode through the electrolyte, producing an electrical current in the external circuit to power a load (Figure 1). The battery recharges by applying an external electrical potential.

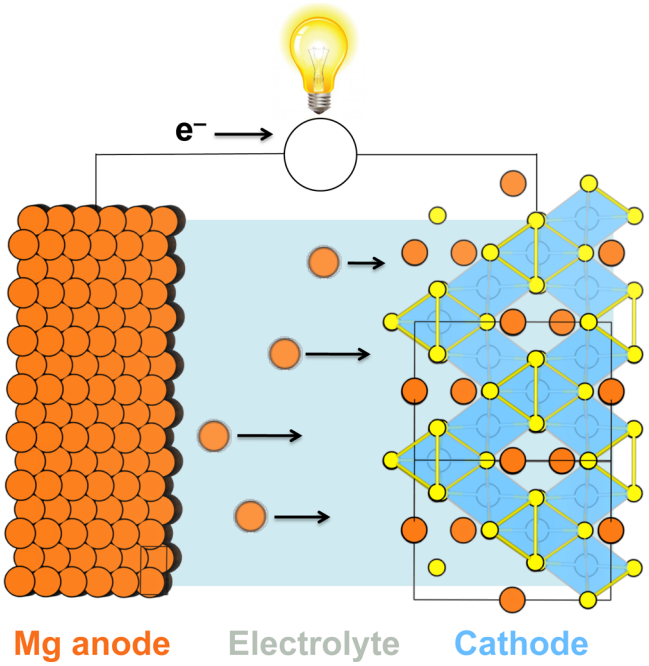

Figure 1. Representative schematic of a discharging MV battery utilizing a Mg anode, electrolyte, and an intercalation cathode.

While early battery technology used aqueous electrolytes, Li-technology with nonaqueous electrolytes has now largely outpaced (in terms of market share) all aqueous chemistries except for Pb-acid. After the rapid expansion of Li-ion in the portable electronics industry over the past decade, Li-ion batteries have now made commercial deployment of electric vehicles (EV) an imminent reality. Since 2007, leading manufacturers have achieved ~8% annual reduction in pack-level costs, reaching approximately US $300/kWh in 2014.[1] The source of these cost reductions is primarily attributed to the economies of scale associated with increased production volumes and engineering advances at the cell and pack scale.[1,2]

The cost of input materials contributes significantly to the overall total, and to continue the path toward cost parity with conventional gasoline powered vehicles, scientists[3] and industrialists[4] alike concede nonincremental improvements in battery technology must be made at the active material level, specifically by developing electrode chemistries that can support both increased gravimetric and volumetric energy densities while maintaining (and improving) the safety, power, lifetime, and cost of state-of-the-art Li-ion batteries. Since advancements at the materials level are approaching a fundamental limit in Li-ion batteries,[3,5,6] achieving even higher energy densities has spurred on investigation into the so-called "beyond Li-ion" technologies, such as Li-O_2 and Li-S.[7−11]

The most appealing "beyond Li-ion" technology for EVs (and portable electronics) will not only offer a significant energy density improvement and cost reduction but will also be compatible with existing, highly optimized Li-ion battery architecture (and fabrication) to take advantage of the knowledge accrued over the past 20 years of Li-ion battery manufacturing. From this perspective, intercalation batteries based on new multivalent (MV) chemistries, such as Mg^{2+}, Ca^{2+}, Zn^{2+}, etc., are especially interesting because they have the potential to meet the aforementioned criteria. While current commercial Li-ion batteries operate with a graphitic anode and an intercalation transition-metal oxide cathode separated by a nonaqueous electrolyte, an analogous MV cell can be envisioned with each component now based on a MV chemistry, as shown in Figure 1. MV batteries will be able to electrochemically store energy through its three main components: the intercalation cathode where MV ions are inserted/extracted, a metal anode (e.g., Mg), and an electrolyte transporting MV-ions between anode and cathode (Figure 1).

1.1. Multivalent Anode and Electrolytes

A MV chemistry can offer significant improvement in volumetric energy density simply by using a metallic anode (~3833 mAh/cm^3 theoretical volumetric energy density for Mg compared to ~2046 mAh/cm^3 for Li metal). This is feasible because early evidence indicates that the metallic form of common MV intercalation ions (Mg, Ca) deposits more uniformly than metallic Li during electrochemical cycling.[12−15] The surface area of lithium metal anodes grows substantially upon cycling, leading to an increase in the surface reactions with the electrolyte. The instability of this surface layer with increased temperature, accelerates thermal runaway, and can even lead to fire.[14,16−19] While Li metal anodes are frequently used in lab-made Li-cell prototypes, they so far have been practically unusable in commercial batteries because of lack of cycle life and safety concerns. As a result, current Li-ion batteries operate with lower volumetric energy density graphite anodes (~800 mAh/cm^3). Several attempts at development and commercialization of full electrochemical cells with lithium metal as the anode and a liquid electrolyte have often led to disastrous results.[14,16−19]

Although MV cells can potentially achieve high-energy densities using metallic anodes,[12−15] discovering electrolytes capable of reversible MV metal plating/stripping at the anode and supporting reversible intercalation against a high voltage cathode remains a significant and fundamental scientific challenge. The development of versatile MV electrolytes has been curbed by a multitude of factors such as limited chemical and electrochemical compatibility with the electrodes (i.e., narrow electrochemical stability window), lack of reversible MV metal stripping and plating, instability against current collectors, low MV (Mg) mobility leading to the formation of ionic

DOI: 10.1021/acs.chemrev.6b00614
Chem. Rev. 2017, 117, 4287−4341

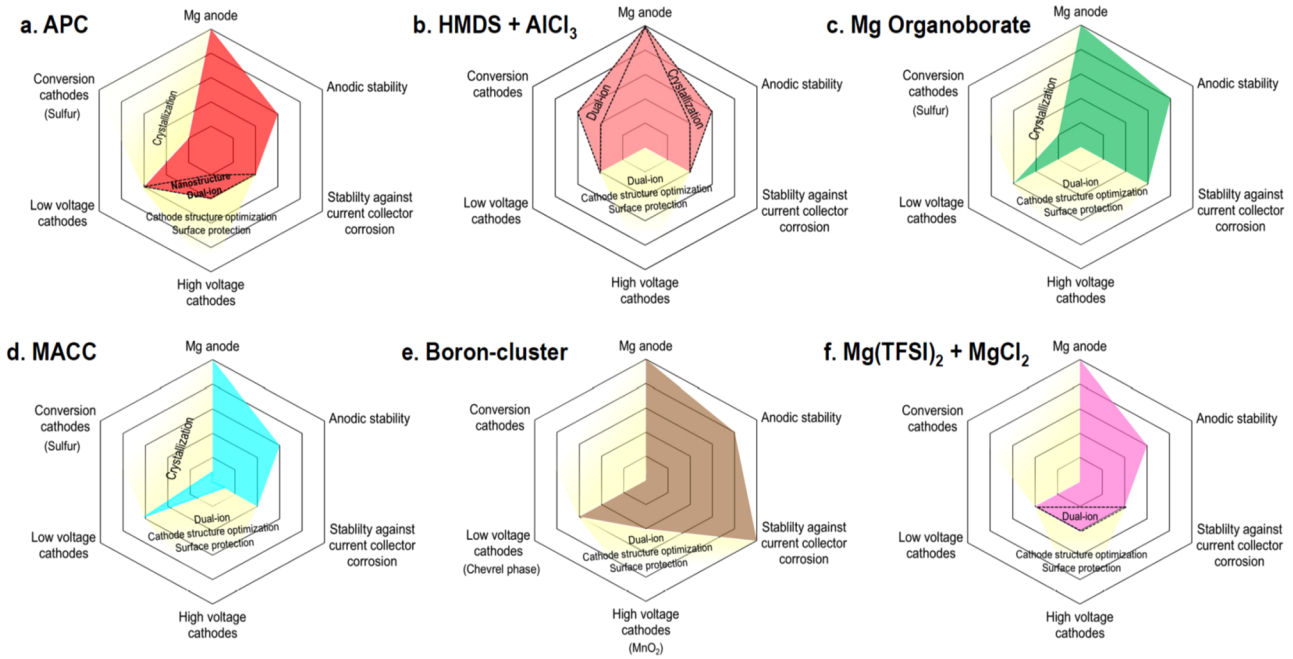

Figure 2. Radar plots charting useful metrics to assess Mg electrolyte fitness for full-cell Mg-ion batteries. (a) All phenyl complex (APC),[20−22] (b) HMDS,[23,24] (c) Mg organoborate,[25,26] (d) MACC,[27−33] (e) Boron-cluster,[34,35] and (f) $Mg(TFSI)_2$.[36−38] Adapted from ref 39. Copyright 2016 American Chemical Society.

couples (i.e., low MV transference number),[40] and low Coulombic Efficiency (CE) as highlighted in Figure 2. While a detailed analysis of the challenges and accomplishments associated with MV electrolyte development is beyond the scope of this work, several comprehensive reports exist in the literature[13,15,20−34,36,38−51] and we summarize the major advancements in MV electrolytes below.

The peculiar electrochemistry of Mg imposes nontrivial limitations on electrolytes, such as being compatible with high-voltage cathode materials and simultaneously achieving reversible Mg deposition at the metal anode. Indeed, Mg electrolytes that are analogous to their Li-ion counterparts (e.g., $LiPF_6$ in PC/DMC solutions) tend to decompose irreversibly at the Mg metal, producing passivating layers resistant to Mg-ion conduction.[24,52] However, Keyzer et al.[48] recently showed reversible Mg stripping and deposition at the metal anode using a solution of $Mg(PF_6)_2{\cdot}(CH_3CN)_6$ in CH_3CN and CH_3CN/tetrahydrofuran (THF) mixtures, with conductivities up to 28 mS cm^{-1} and an anodic stability of ∼4 V vs Mg on Al electrodes.

Historically, Gregory and collaborators[53] at Dow Chemical made a breakthrough in showing quasi-reversible Mg-plating from Grignard's reagents in 1990. It took more than ten years of methodical refinements by Aurbach and co-workers to increase the Coulombic efficiency as well as the anodic stability of the Grignard's electrolytes, leading to the ethereal solutions of organic magnesium aluminum chloride salts (or organo-magnesium-chloride complexes), namely the "dichloro complex" DCC[54] and the "all phenyl complex" APC.[20,22] Subsequently, Doe[27,55] and collaborators at Pellion Technology studied the electrochemistry of a much simpler combination, the magnesium aluminum chloride complex (MACC), formed from a mixture of $AlCl_3$ and $MgCl_2$ in ethereal solvents. The MACC electrolyte exhibits a similar anodic stability (∼3.1 V) to its predecessors (i.e., DCC and APC) and with a high degree of reversible Mg deposition/stripping. In parallel, Kim and co-workers at Toyota R&D[23] developed a non-nucleophilic electrolyte, radically different from the chloride complexes, which was composed of a mixture of hexamethyldisilazide magnesium chloride (HMDSMgCl) and $AlCl_3$ and primarily targeted usage in high-energy density Mg−S batteries. Although the DCC, APC, and MACC electrolytes can be utilized in state-of-the-art Mg-battery prototypes,[12] they are known to corrode various metals, including stainless steels and common current collectors.

The limitation of chloride electrolytes fueled interest in alternative chemistries. For example, Shao et al.[56] demonstrated reversible magnesium deposition from a diglyme solution of $LiBH_4$ and $Mg(BH_4)_2$, albeit with poor anodic stability (∼1.8 V). Meanwhile, Mohtadi, Carter, Tutusaus, and co-workers at Toyota R&D discovered a series of promising halogen-free electrolytes,[34,35,42] such as Mg boron-clusters and carboranes (see Figure 2, panels c and e), which are less corrosive against current collectors and show the highest anodic-stability windows (∼3.8−4.0 V) reported so far.[40] Also, the increasing attention for MV chemistries has stimulated research toward the search of electrolytes capable of reversible Ca-stripping and deposition.[15,57,58]

While the last 20 years have witnessed an increasing focus in the development of new Mg electrolytes, the array of electrolytes compatible with high voltage Mg-cathodes (e.g., MnO_2, V_2O_5, etc., see Section 5) is rather limited (Figure 2),[13,24,43,44] with researchers normally employing the usual suspects of $Mg(ClO_4)_2$, $Mg(NO_3)_2$, or $Mg(TFSI)_2$ dissolved in acetonitrile (ACN), THF, or glymes (with water inclusion in a few cases). As such, experiments on high-voltage cathodes rely on complex 3-electrode setups that can separate the incompatible chemistries of Mg metal deposition (and stripping) and Mg intercalation in the cathode, leading to the lack of routine protocols to prepare Mg cells (see the discussion in section 7). Moreover, Lipson et al.[40] have clearly demonstrated that the anodic stability reported for some Mg

DOI: 10.1021/acs.chemrev.6b00614
Chem. Rev. 2017, 117, 4287−4341

electrolytes aforementioned largely depends on the nature of the working electrode, suggesting that particular care is required while performing and reporting new experiments. Additionally, the literature on the passivation of MV cathodes is particularly scarce,[38,59−61] despite a few studies attempting to unravel the complex interactions of Mg^{2+} and a few cathode materials with electrolyte salts and solvents (e.g., Figure 7, later),[31,33,40,51,61−67] emphasizing the need for more systematic studies of the cathode-electrolyte interfacial processes.

1.2. Multivalent Cathode

Significant energy density gains can be realized only if a MV anode can be paired with a MV-insertion cathode material capable of yielding high-capacity at a sufficiently high voltage and with reasonable rate performance.[68−72] While the literature reports a few working multivalent cathode materials (discussed in the following sections), the MV intercalation host space is relatively unexplored compared to Li ion,[73] creating a higher potential for the discovery of new functioning cathode materials. As a consequence of transferring two (or more) electrons per ion, MV-intercalation can potentially achieve higher capacities than Li-ion cathodes even when occupying a similar number of intercalant sites. Redox reactions permitting, such gains can be combined with the energy density increase associated with the use of a high-capacity metal anode.

This review focuses primarily on existing Mg^{2+} intercalation systems widely studied in the literature, alongside examining the possibility of other MV chemistries such as Zn^{2+}, Ca^{2+}, etc., when possible. The increased focus on Mg reflects the volume of burgeoning MV-related research published in the past few years, as presented in Figure 3.

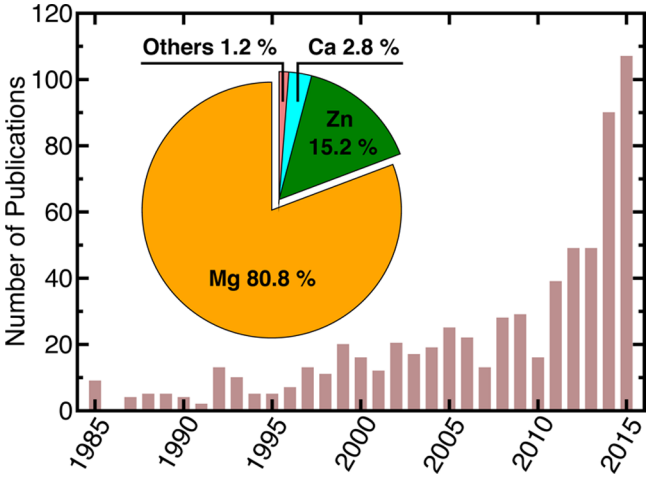

Figure 3. Number of publications from 1985 until 2015 featuring MV electrochemistry. The pie-chart in the inset shows the partition of MV publications for different reversible chemistries (i.e., Mg, Zn, and Ca). The subset "others" comprises Al, Sr, and Ba electrochemistries. The plotted data is retrieved using Web of Science by Thomson Reuters.

The review effort begins by revisiting the large volume of literature published, chiefly by Prof. Doron Aurbach and collaborators, on the chalcogenide-based Chevrel-phase cathodes in section 3, which enabled the realization of the first working Mg (MV)-battery prototype in 2000.[12] To improve upon the energy density of the Chevrel-phase (with only 128.8 mAh/g of the theoretical capacity at ∼1.1 V), while maintaining comparable kinetic performance, intercalation into more compact frameworks such as chalcogenide spinels has been sought, as discussed in section 4.

Our analysis then proceeds to recent work on transition-metal oxides as possible MV cathode materials, both in layered and close-packed lattices (section 5). In general, the rather ionic character of common transition-metal oxides enables MV-insertion at desirable high voltages at the cost of dramatically reduced bulk diffusion properties. Polyanion cathode materials are explored in section 6. The presentation of the MV literature on intercalation cathodes concludes with section 7, which discusses the common issues of developing novel multivalent cathodes, offering potential solutions and newer avenues to explore the chemical space of inorganic materials.

Throughout this review, the gravimetric capacities (in mAh/g) and energy densities (in Wh/kg) of specific cathode materials are reported for the charged stoichiometry (not intercalated) unless explicitly noted. Whenever the cathode experimental densities are accessible, either from the Inorganic Crystal Structure Database (ICSD) or the literature, the volumetric energy densities (in Wh/l) are reported for the charged state to complement the gravimetric values, thereby helping us to chart the performance of each cathode chemistry against energy density guidelines from the techno-economic models of section 2. Notably, all energy densities and the current status of cathode candidates encompassed in this review have been compiled in Table 3.

The scope of this review is intended not only to present a collection of MV-cathode materials ranked by their energy density and electrochemical performance to meet the minimal standard charted by techno-economic models but also to critically analyze the fundamental science behind the complex intercalation reactions occurring in MV cathode materials. As our critical analysis of the MV literature will demonstrate, a sufficiently deep understanding of MV intercalation often requires the utilization of multiple characterization techniques in addition to routine electrochemical measurements and established cathode engineering procedures. Whenever possible, the review emphasizes the importance of integrating electrochemistry experiments with theoretical investigations and characterization to prove that MV intercalation actually takes place. The review encompasses a variety of aspects ranging from charting the design metrics for developing novel MV-cathodes to targeted in-depth studies rationalizing complex experimental and theoretical results.

2. TECHNO-ECONOMIC MODELING OF MV BATTERIES

Techno-economic models, such as the Battery Performance and Cost (BatPaC) model, developed by some of us,[74−78] can aid in underlining the cost-effectiveness of an upcoming battery technology, such as the MV technology in this review. The peer-reviewed and validated material-to-system BatPaC model[77] is a publicly available bottom-up design and cost model developed through support by the U.S. Department of Energy Vehicle Technologies Office. Additionally, BatPaC has been sponsored (2017−2025) by the U.S. Environmental Protection Agency and will be used to evaluate the cost and performance of Li-ion batteries for light duty vehicles in the United States. It is worth noting here that other, simpler models exist in the literature, such as the one by Berg and co-workers,[79] which are amenable to a large scale analysis of many battery configurations. Their model yields a similar value to the BatPaC model when applied to a cell employing graphitic

DOI: 10.1021/acs.chemrev.6b00614
Chem. Rev. 2017, 117, 4287−4341

carbon anode, and $LiNi_{1/3}Mn_{1/3}Co_{1/3}O_2$ (NMC333), a common state-of-the-art Li battery cathode material. While the model by Berg et al.[79] model has not yet been applied to Mg batteries, as the MV field matures and reliable data on more Mg batteries becomes available, it would be interesting to compare different techno-economic models to Mg battery cathodes to examine how practical costs and energy densities vary across chemistries. Indeed, a practical MV battery is expected to use different current collectors, separators, electrolytes, etc. compared to current Li-ion systems, which will change both energy densities and costs. However, at present, we focus our economic analysis on the BatPaC model, which is explained below, to arrive at tentative metrics.

BatPaC estimates the cost of a complete system, producing direct current (DC) electricity, which has been manufactured in a high volume, competitive market future state. In our analysis, we studied a range of hypothetical positive electrodes by examining system-level properties as a function of cell voltage (vs Mg metal) for various theoretical specific energies (an intrinsic material property).[76] A crystal density of ~4 g/cm^3, as encountered in spinel-$LiMn_2O_4$,[80] is assumed, while a 50% excess capacity at the anode is chosen. Although our review covers a variety of cathode chemistries, we targeted oxide cathodes in our techno-economic analysis because oxides represent the upper bound for cathode energy density. As we will discuss, the utilization of a nonoxide cathode can improve kinetics at the expense of energy density. However, the present analysis seeks to explore the practical limits of energy density for multivalent batteries, and so an oxide cathode is assumed. In addition to a detailed analysis based upon these assumptions, we will also present the effects of varying the cathode density, which is one of the major differences between, for example, an oxide and a sulfide cathode. The model also accounts for a 10 μm thick Cu and a 15 μm thick Al current collector for the anode and cathode, respectively, in addition to a 15 μm thick separator.[74,75,78] More details of the BatPaC model are available in refs 74−78 and http://www.cse.anl.gov/batpac.

Figure 4a illustrates the potential of a multivalent system utilizing a magnesium metal negative electrode to meet the United States Advanced Battery Consortium (USABC) and Department of Energy's battery technology targets for electric vehicles (i.e., $ 100/kWh and 750 Wh/l at the cell level based on usable energy).[81] For comparison, a current state-of-the-art Li-ion cell utilizing a graphitic carbon anode and a $LiNi_{1/3}Mn_{1/3}Co_{1/3}O_2$ cathode has a cell-level energy density of ~480 Wh/l (~200 Wh/kg)[75,82] at an estimated cost of ~230 $/kWh for 2017−2018.[1]

Notably, Figure 4a shows the results of two scenarios obtained with BatPaC, illustrating maximum theoretical energy densities from different cell designs: (i) solid lines show the energy densities at optimum electrode thickness calculated by BatPaC to meet pulse power requirements at 80% open circuit voltage (OCV) and sustained discharge at a C/2 rate, assuming impedances and electrolyte transport properties in state-of-the-art lithium-ion energy cells (thus accounting for polarization effects and other losses),[74,75,78] and (ii) the dashed lines correspond to a simplified model that arbitrarily assumes a constant positive electrode thickness of 100 μm and 100% OCV. Note that the hypothetical 100 μm scenario (dashed lines) has been included solely for the purpose of comparison with the BatPaC model. For each active-materials-only specific energy (in Wh/kg), the corresponding active-materials-only volumetric energy density in Figure 4a (in Wh/l, indicated in brackets) is presented as an averaged value across the range of voltages considered (2−4.5 V vs Mg). While this is an approximation, in practice, the active-materials-only volumetric energy density varies by less than 8% for the aforementioned voltage range (at a given specific energy) and does not qualitatively affect the comparisons. For some cases (e.g., 1000 Wh/kg ≈ 3200 Wh/l at low voltages, ~ 2.0 V) seen for the 100 μm model of Figure 4a, the curvature reflects Mg metal becoming a higher fraction of the total mass, thus lowering the

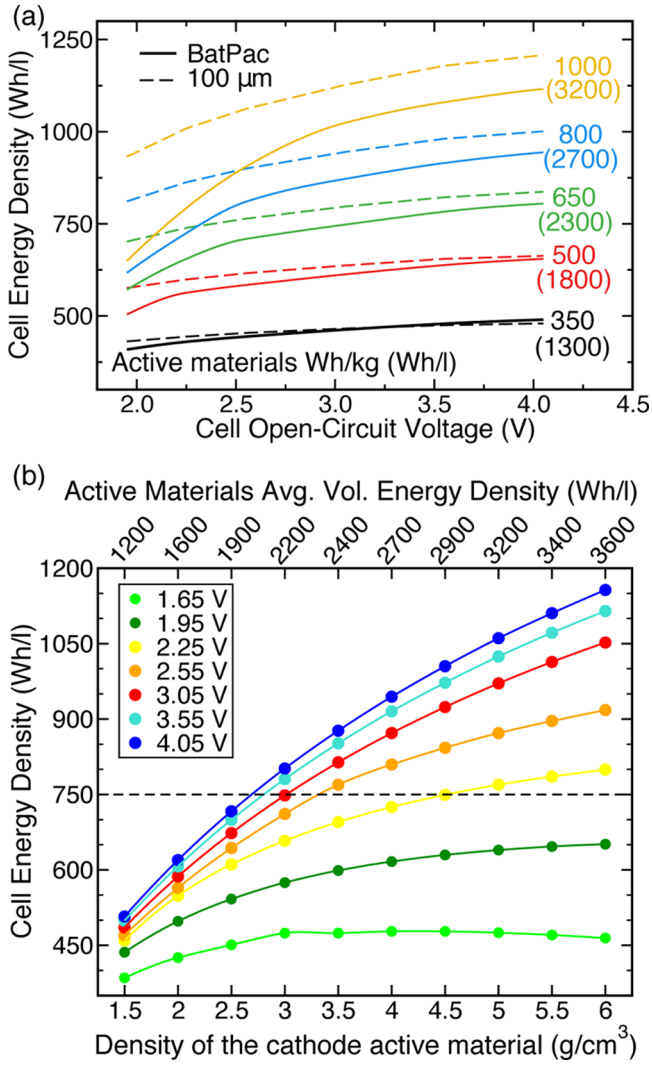

Figure 4. (a) Cell level energy density as a function of the average open-circuit cell voltage. Multiple curves are shown for different active materials-only specific energies (average volumetric energy density across the voltage range shown in parentheses). The specific energy accounts for the weight of anode and cathode only. These values were calculated with BatPaC at the cell level for a 50 kWh battery pack with a 120 kW pulse capability (solid lines) or using a cathode of 100 μm thickness (dashed lines), respectively. (b) Variation of the volumetric cell energy density as a function of the density of the active cathode material, as calculated by BatPaC, at 800 Wh/kg active-materials-only cell specific energy. The different colors in (b) represent the change in the cell energy density as a function of the OCV vs Mg metal anode, ranging from 1.65 V (light green) to 4.05 V (blue), with the dashed line representing the USABC target. The top x axis of (b) shows the corresponding volumetric energy density at a specific energy of 800 Wh/kg and the particular cathode density.

DOI: 10.1021/acs.chemrev.6b00614
Chem. Rev. 2017, 117, 4287−4341

total energy density of the cell (Mg's density is 1.74 g/cm^3 vs ~4 g/cm^3 for an oxide cathode).

The analysis suggests a magnesium metal negative electrode (with a capacity of 2205 mAh/g) coupled with a positive electrode that yields a materials-only cell specific energy greater than 800 Wh/kg (or a volumetric energy density of 2700 Wh/l), and voltage greater than 3.1 V is a potential pathway to meet the USABC cell-level target of 750 Wh/l. The overall gravimetric capacity of the cell is calculated by taking the reciprocal sum of both gravimetric capacities of the cathode and anode (~2205 mAh/g for Mg). As a result, a materials-only cell-level specific energy of 800 Wh/kg at 3.1 V OCV vs Mg metal anode will set a gravimetric capacity of ~298 mAh/g for the positive electrode active material, which will in turn reflect a volumetric capacity of ~1192 Ah/l for a 4 g/cm^3 oxide cathode. Hence, for achieving the 750 Wh/l USABC cell-level target, a 4 g/cm^3 dense cathode active material should have an energy content of ~908 Wh/kg and ~3632 Wh/l, respectively. In comparison, current Li-ion intercalation systems nominally yield ~200 Wh/kg at the cell-level, with (practical) positive electrode active material energy densities of ~565 Wh/kg and ~2600 Wh/l for NMC333.[75]

Multiple pathways do exist to achieve the USABC targets using MV systems, such as using a 650 Wh/kg cell specific energy system at OCV greater than 3.5 V vs Mg (indicated by the solid green line in Figure 4a), and each specific chemistry requires an independent, focused analysis. The ability of a cell design to achieve our target at lower voltages is nominally hindered by impedance effects. Mitigating engineering efforts such as nanoarchitectures and/or increased operating temperatures may be required below 2.75 V to capture higher fractions of the active-material specific energy at the system level.

For a more complete analysis of the Mg-cathode chemistries encompassed by this review, we will compare both gravimetric and volumetric energy densities of candidates against the target values of ~908 Wh/kg and ~3632 Wh/l, as suggested by the techno-economic analysis based on current Li-ion technology (solid blue line in Figure 4a). Note that the target materials-only cathode energy densities may change according to the density of the specific positive electrode candidate and the porosity assumed (~32 vol % void or ~53 vol % active cathode material at 4 g/cm^3) in the BatPaC model. For example, Figure 4b illustrates the variation of the volumetric energy density of the cell with the change in the density of the cathode active material, at various OCV vs Mg metal, for a materials-only cell specific energy of 800 Wh/kg. Interestingly, an increase in the density of the positive electrode active-material reduces the minimum OCV required to achieve the targeted 750 Wh/l at the cell level. Indeed, at a cathode active material density of 6 g/cm^3, the USABC target can be potentially achieved at OCV, cathode gravimetric, and cathode volumetric energy densities of ~2.25 V vs Mg, ~ 954 Wh/kg, and ~5722 Wh/l, respectively, in comparison to the minimum of ~2.55 V, ~ 932 Wh/kg, and ~3731 Wh/l required for a 4 g/cm^3 cathode. Furthermore, a decrease in cathode active material density to ~2 g/cm^3 prohibits reaching the 750 Wh/l cell-level target even at an OCV of ~4.05 V vs Mg, indicating the importance of a dense MV cathode. Although materials with densities ranging from ~5.2 g/cm^3 (Chevrel-Mo_6S_8,[83] section 3) to ~1.7 g/cm^3 (Prussian Blue,[84] section 6) have been attempted as MV-cathodes, for the sake of benchmarking, we will use values of ~908 Wh/kg and ~3632 Wh/l as reference (as obtained based on current Li-ion architecture) and detail-significant discrepancies for each cathode material.

Calculations for calcium-based chemistries are expected to show similar results: the higher mass of calcium should be offset to a large extent by the lower electrochemical potential of Ca metal. According to our techno-economic models, Mg batteries based on Mg metal coupled with a high-voltage cathode host can achieve the targets specified by the USABC.[77] Although the USABC targets are for electric vehicles, it is worth noting that the superior volumetric energy density offered by multivalent batteries (as compared to Li-ion batteries utilizing graphitic carbon anodes) would also be favorable for portable electronics.

3. STATE-OF-THE-ART MV BATTERIES: CHEVREL STRUCTURES

Although the concept of a rechargeable magnesium battery was proposed as early as 1990,[53] the first working demonstration of a prototype Mg full cell battery was only achieved in 2000 by Aurbach et al.[12] using a magnesium metal anode, an electrolyte based on a solution of Mg organo-halo-aluminate salts in THF, and a Chevrel $Mg_xMo_6S_8$ cathode ($0 < x_{Mg} \leq 2$). With these innovations at the electrolyte and cathode, the authors were able to achieve good kinetics and cycle life (>2000 cycles) operating at approximately 1.1 V vs Mg metal and with ~70 mAh/g (128.8 mAh/g theoretical capacity),[12] corresponding to ~77 Wh/kg and ~400 Wh/l energy content at Chevrel's density of ~5.2 g/cm^3.[83] This landmark result strengthened the credibility of MV technology and also laid a definitive benchmark to evaluate novel candidate MV cathode materials.

On the process of discovering the Chevrel phase as a Mg intercalation host, the authors remarked that it was the result of "a lot of unsuccessful experiments of Mg ions insertion into well-known host for Li^+ ions insertion, as well as from a thorough literature analysis concerning the possibility of divalent ions intercalation into inorganic materials."[72] Of note, batteries based on Chevrel compounds were proposed and demonstrated to function for Li-ion as early as 1985,[85] and several different monovalent, divalent,[86,87] and trivalent cations[88] have shown mobility within the Chevrel structure.[89] For example, the electrochemically extracted diffusivities for Co^{2+}, Ni^{2+}, Fe^{2+}, Cd^{2+}, Zn^{2+}, and Mn^{2+} ions are quite high in Mo_6S_8, ~10^{-9} cm^2/s,[90] compared to ~10^{-11}–10^{-13} cm^2/s for Mg^{2+}.[91]

Unlike today's commercialized Li-ion cathode materials, which are almost entirely structures with close-packed oxygen anion sublattices (e.g., layered, spinel, and olivine), the Chevrel phase has a unique "cluster" structure as shown in Figure 5. The Chevrel structure is comprised of Mo_6T_8 blocks (T = S, Se, and Te; gray cubes in Figure 5, panels a and b), with 6 Mo forming an octahedron on the faces of the cubes and 8 T anions occupying the corners.[94−96] The Mo_6S_8 blocks are arranged such that they are separated by three types of "cavities", as illustrated in Figure 5b, with each cavity bound by 8 anion atoms forming pseudocubes. Type 1 cavities are the farthest away from Mo atoms as they share corners with the Mo_6T_8 cubes, whereas type 2 and type 3 cavities share edges and faces, respectively. Intercalant ions are normally hosted within the cavities of type 1 and 2 since type 3 cavities are destabilized by high electrostatic repulsions with the face-sharing Mo atoms. The specific site position within each cavity varies with the size of the cation species,[97] with the sites for Mg^{2+} shown in the insets of Figure 5 (panels b and c).[93,94,96,97] For example, a ring of six "inner sites" within cavity 1 and two "outer sites" in cavity

DOI: 10.1021/acs.chemrev.6b00614
Chem. Rev. 2017, 117, 4287−4341

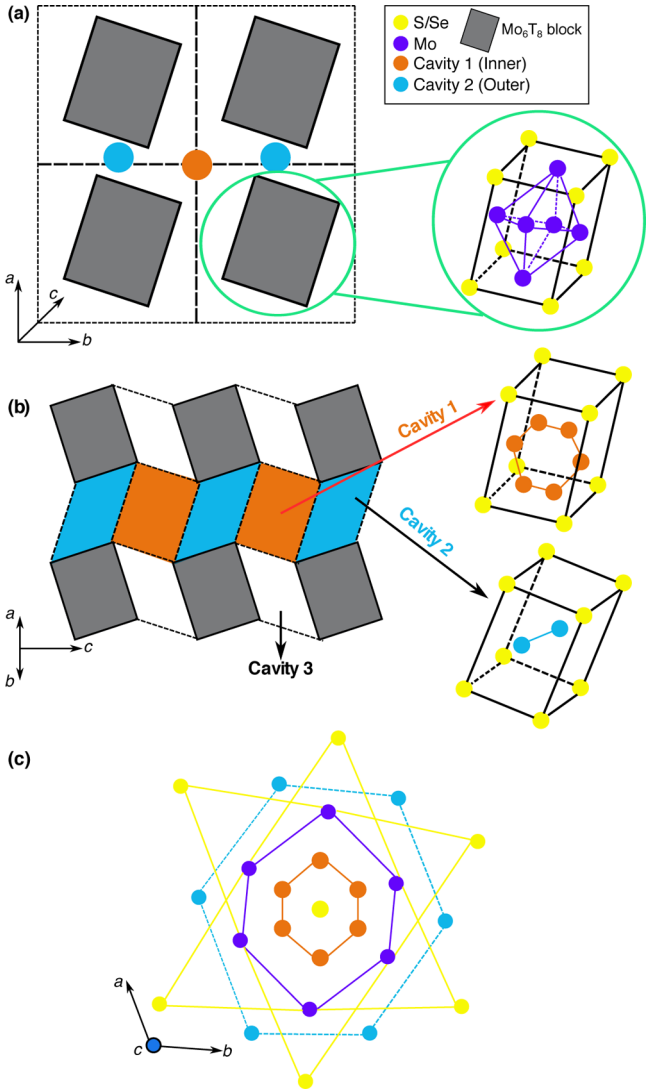

Figure 5. The crystal structure of the Chevrel host, with the gray rectangles representing Mo_6T_8 blocks (T = S, Se), comprising the Mo_6 octahedra enclosed within a T_8 cube. (a) Displays a projection of the structure on the a–b plane, where orange and blue circles indicate the centers of the cavity sites of type 1 and type 2, respectively, adapted from ref 92. (b) Indicates the 6 "inner" (type 1) and 2 "outer" (type 2) cavity sites.[92] (c) Shows a top view of the structure, highlighting the distorted hexagonal patterns made by the inner and outer cavities.[93] (a) and (b) Reprinted with permission from ref 92. Copyright 2015 Wiley-VCH. (c) Reprinted and adapted with permission from ref 93. Copyright 2014 Elsevier.

2 can be occupied by small ions (such as Li^+, Mg^{2+}, or $Cu^{1+/2+}$), while larger ions (Pb^{2+} or Sn^{2+}) normally occupy the center of each cavity (Figure 5b). Considering the topology of Mo_6S_8 blocks, where each block is corner-sharing with 8 cavity cubes of type 1 and edge-sharing with 12 cubes of type 2, there are 12 possible sites (6 inner and 6 outer, as illustrated in Figure 5c) between each Mo_6S_8 block where the intercalating ion (such as Li^+ and Mg^{2+}) can reside.[93]

The unintercalated Chevrel Mo_6S_8 structure is thermodynamically metastable and can be obtained by first synthesizing $Cu_2Mo_6S_8$ through element solid-state reaction (or alternatively through lower-temperature precipitation methods),[98] followed by the acid-leaching of Cu from the synthesized phase.[99−101] Also, the Mo octahedral clusters exhibit metallic bonding and are each capable of accommodating a total of 4 electrons.[102] Accordingly, two Mg^{2+} ions can be inserted per Mo_6S_8 block with the first ion accommodated preferentially in the inner sites and the second in the outer sites, which is reflected in the voltage plateaus observed during Mg discharge at ∼1.4 and ∼1.1 V, respectively (see Figure 6a).[83,96]

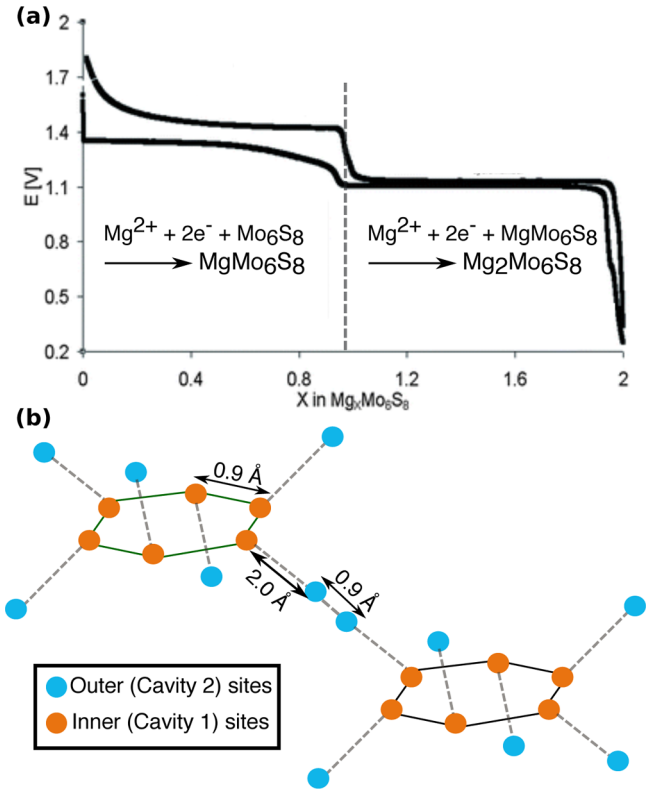

Figure 6. (a) Voltage-capacity curve of Mg insertion into Mo_6S_8 from ref 13 and (b) a schematic illustration of the hop distances between similar (inner → inner, outer → outer sites) and dissimilar (inner → outer) hops.[96] (a) Reproduced and adapted with permission from ref 13. Copyright 2013 The Royal Society of Chemistry. (b) Reprinted from ref 96. Copyright 2006 American Chemical Society.

As mentioned earlier, different cations occupy different sites within cavity 1 and cavity 2 (Figure 5), which contributes to the complex mobility behavior observed across varying cation species in the Chevrel structure.[89] For example, poor mobility is observed for large cations such as Pb^{2+}, Sn^{2+}, and Ag^+ compared to smaller cations such as Ni^{2+}, Zn^{2+}, and Li^+ in the ternary structure (e.g., MMo_6T_8), but in mixed cation systems (e.g., $M'MMo_6T_8$) coupled diffusion of small and large cations is possible as observed in insertion-displacement reactions.[83,103,104] Notably, the presence of Cu in the host structure has a beneficial effect on the Mg^{2+} intercalation kinetics.[83,104,105]

Certain intercalating species, such as Cd^{2+}, Na^+, and notably Mg^{2+}, can undergo a "trapping" behavior, where ion insertion into the Chevrel may be feasible, but complete extraction is difficult.[72,89,93,98,103,105] For $Mg_xMo_6S_8$ ($0 < x_{Mg} < 2$), facile extraction of Mg^{2+} at room temperature is possible between $Mg_2Mo_6S_8$ and $Mg_1Mo_6S_8$, but Mg^{2+} mobility is observed to be poor between $0 < x_{Mg} < 1$, which limits capacity.[91] In this concentration regime where Mg occupies the inner sites, steric changes in the host structure cause the barrier for a Mg^{2+} hop to the outer sites to be higher than for a hop within the inner

DOI: 10.1021/acs.chemrev.6b00614
Chem. Rev. 2017, 117, 4287−4341

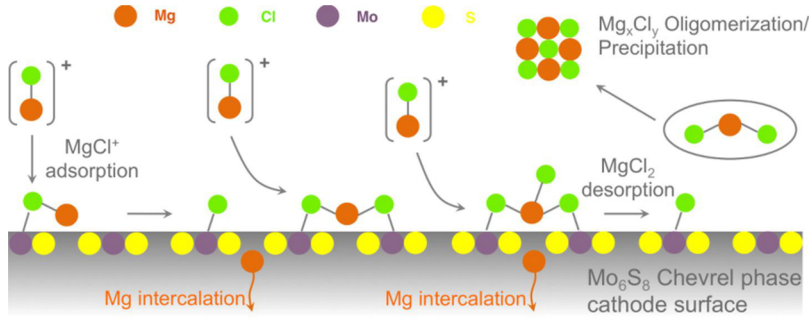

Figure 7. Proposed mechanism for Mg desolvation and absorption in Mo_6S_8 from Cl^--containing electrolyte from Wan et al.[59] $MgCl^+$ adsorbs on the Mo_6S_8 surface, where the Cl^- atoms adsorb preferentially on the Mo atoms and the Mg intercalates along the S_8 cubes. (b) Reprinted from ref 59. Copyright 2015 American Chemical Society.

ring, with the outer sites estimated to be ~275 meV higher in energy compared to the inner sites (using first-principles calculations).[96,106] In addition, inner−inner (and outer−outer) site hops are relatively shorter in distance (~0.9 Å) compared to the inner−outer site hop (~2.0 Å), reducing the likelihood of the inner−outer hops (see Figure 6b).[13,96] Consequently, Mg^{2+} ions preferentially hop within the inner ring, which limits the net displacement of the ion and causes the kinetically accessible capacity to be reduced.[89] The full theoretical capacity can be extracted at elevated temperature (~60 °C), albeit with significant voltage hysteresis between the charge and discharge cycles in the $0 < x_{Mg} < 1$ range (as in Figure 6a). In the Mo_6Se_8 host, these steric changes are less significant which lessens the effect of locally correlated Mg hops that occur in the Mo_6S_8 system, and consequently, the full theoretical capacity is accessible at room temperature.[96,107]

A recent report by Nikolowski et al.[108] attempted to identify the structural transformation of Mo_6S_8 during Mg insertion by means of in situ Synchrotron XRD. Particularly, Rietveld refinements on the XRD data allowed the authors to identify 3 distinct phases (all with the $\bar{R}3$ space group) forming during Mg discharge: at $x_{Mg} \leq 0.1$, $0.2 \leq x_{Mg} \leq 0.3$, and $0.4 \leq x_{Mg} \leq 0.8$, with all three phases coexisting between $0.4 \leq x_{Mg} \leq 0.5$. In parallel, using in situ neutron diffraction, Levi et al.[109] studied the rhombohedral → triclinic (R → T) distortion that occurs in $MgMo_6Se_8$ at approximately 80 °C. Levi and co-workers attributed the R → T transition, which normally occurs on cooling, to the strong distortions of the $MgSe_4$ tetrahedra that occur in combination with a "critical delocalization" of Mg^{2+} ordering in the R structure, in contrast to the more popular hypothesis of cation "freezing" at low temperatures resulting in Mg^{2+} mobility loss.[109]

Recent first-principles investigations of MV intercalation into the Chevrel structure have not only studied the changes in the electronic structure[110,111] and the surface adsorption properties[59] during Mg intercalation but have also explored the intercalation of other alkaline-earth metals such as Ca^{2+}, Sr^{2+}, and Ba^{2+}.[112] Thöle et al.[110] predicted metallic behavior for pristine Mo_6S_8 and a S redox center. In contrast, Smeu et al.[112] predicted not only a semiconducting (pristine) Mo_6Se_8 and a Mo_6 redox center but also a remarkable increase of voltage with Ca^{2+} intercalation, inconsistent with thermodynamic principles. A recent comparison of simulated and experimental X-ray absorption near edge spectroscopy (XANES) data[111] confirms the electron transfer from Mg to S atoms in the Chevrel host, in agreement with ref 110. Adsorption of the Mg_xCl_y electrolyte complexes on the Chevrel surface, as calculated by Wan and co-workers,[59] indicate the importance of the presence of Mo atoms on the surface, which aid in breaking the Mg−Cl bond, while the S atoms facilitate the intercalation of Mg into the bulk structure with a migration barrier of ~500 meV (as shown in Figure 7). However, the bulk Mg migration barrier has been recently estimated as ~360 meV.[106]

Mg intercalation in Chevrel structures represents state-of-the-art performance in MV batteries, displaying excellent reversibility and intercalation kinetics, but its present form provides energy densities below the desired energy density targets outlined in Figure 4 (for MV systems). Subsequent sections of this review will explore alternative chemistries to the Chevrel-phase, namely chalcogenides (sulfides and selenides), oxides, and polyanion host frameworks that can potentially achieve higher voltages and reversible capacity, while maintaining reasonable rate-performance.

4. CHALCOGENIDES

A viable alternative to improve upon the Chevrel electrochemical performance is by utilizing other transition metal chalcogenides, AMT_2, with A the multivalent ion, M the transition metal ion, and T = S, Se, and Te. Similar to the Chevrel-phase (section 3), the increased covalency and larger volume per anion of chalcogenides, in comparison to oxides, tends to decrease the electrostatic interactions between the diffusing MV ion and the anion lattice,[113] thus reducing the migration barriers for MV diffusion. Accordingly, the ion polarizabilities, the ability to deform the anion electronic charge density by an external electric field or potential (e.g. the charge of a diffusing MV ion), increase moving down the chalogenide group, as depicted in Figure 8. Nevertheless, as demonstrated for the Chevrel-phase in section 3, and by the large volume of research on Li-intercalation in chalcogenides,[115−117] the increase of intercalating ion mobility comes at the expense of lower voltages, thereby reducing the energy densities of chalcogenide materials. However, sulfur containing cathodes, including the Chevrel and TiS_2 (see below), are the only materials to date that have demonstrated reversible Mg^{2+} intercalation against a Mg metal anode.

This section encompasses both experimental and computational works on MV intercalation in chalcogenide cathodes, highlighting the most recent findings and unsolved challenges.

4.1. Layered and Spinel TiS_2

Mg intercalation in bulk layered-(TiS_2), spinel-(Ti_2S_4), and nanotube-titanium sulfides has been the subject of both experimental[72,118−123] and theoretical investigations,[124] in analogy to the well-known Li cycling in TiS_2.[115,117] In 1991,

DOI: 10.1021/acs.chemrev.6b00614
Chem. Rev. 2017, 117, 4287−4341

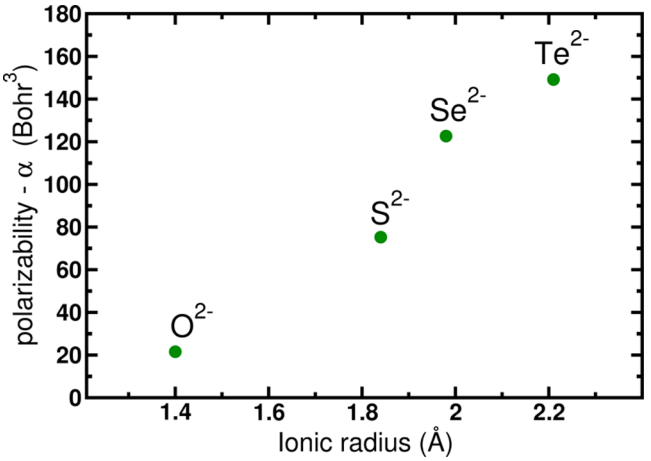

Figure 8. Computed polarizabilities (using a 6-311+G(2d,2p) basis-set at the DFT/B3LYP level of theory) of isolated anion vs experimental ionic radius in a 6-coordinated environment.[114]

Bruce and collaborators[118,119] were able to chemically magnesiate spinel-Ti_2S_4 using dibutyl-magnesium, demonstrating the existence of a continuous $Mg_xTi_2S_4$ solid solution for $0 < x_{Mg} < 0.5$. In contrast, magnesium intercalation in layered-TiS_2 did not yield a single phase product, the magnesiated TiS_2 coexisted with the as-synthesized phase but with expansion of the layer spacing, consistent with recent XRD measurements on electrochemical Mg intercalated layered-TiS_2[123] and DFT calculations.[124]

Later Amir and Aurbach et al.,[72,120] using a full-cell comprising of a Mg-anode and $Mg(AlCl_2BuEt)_2$:THF as electrolyte, studied reversible Mg intercalation in a variety of sulfides, selenides, and their solid solutions (i.e., $CuFeS_2$, $CuFe_2S_3$, Cu_9S_8, Cu_2S, NiS, layered-TiS_2, spinel-Ti_2S_4, TiSSe and NiS_xSe_y solid solutions). According to the authors,[72,120] all these materials showed some degree of reversible Mg intercalation, but voltage profiles were only reported for layered-TiS_2 (with 1st discharge capacity of ~20 mAh/g) and spinel-Ti_2S_4 (~90 mAh/g) at 60 °C, as shown in Figure 9a. Despite the large capacity fade upon cycling (Figure 9a), Amir et al.[120] claimed that Mg undergoes intercalation reactions only in titanium sulfides, whereas Mg displaces the transition metals in $CuFeS_2$, $CuFe_2S_3$, Cu_9S_8, Cu_2S, and NiS, with some degree of electrochemical reversibility. The X-ray diffraction (XRD) patterns and other characterization results, useful to assess Mg intercalation in the TiS_2 phases, were not reported.[72,120]

Though historical attempts of Mg intercalation in the TiS_2 polymorphs had failed, recent experimental work by Sun et al.[121,123] has shown extensive reversible Mg cycling in these cathode materials (Figure 9, panels b and c), in agreement with theoretical calculations.[124]

Highly reversible Mg intercalation in spinel-Ti_2S_4 with an All Phenyl Complex (APC) electrolyte in THF utilizing a coin-cell

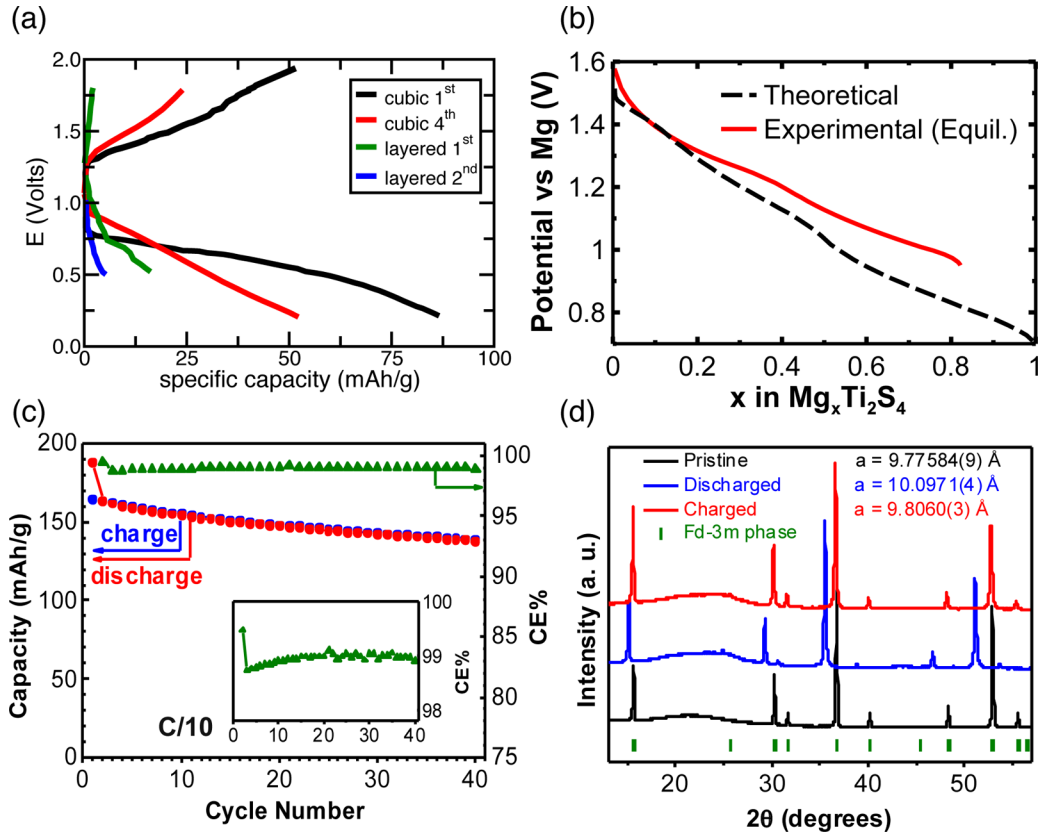

Figure 9. Electrochemistry of (a) layered-TiS_2 and (a, b, and c) spinel-Ti_2S_4 with a Mg anode at 60 °C. (a) Discharge and charge curves of the first four cycles in $Mg(AlCl2BuEt)_2$:THF electrolyte are digitized from ref 120. (b) Voltage curves for spinel $Mg_xTi_2S_4$ (black line) calculated at 300 K with Monte Carlo simulations parametrized on DFT data and using Galvanostatic Intermittent Titration Technique (GITT) at 60 °C (red line) from ref 121. (c) Capacity and CE evolution at a C/10 rate in APC/tetraglyme electrolyte, with inset showing 99% CE.[121] (d) Comparison of the XRD patterns of the pristine Ti_2S_4 spinel (black), with the discharged (blue) and charged (red) states.[121] (a) Reprinted and adapted with permission from ref 120. Copyright 2007 Elsevier. (b, c, and d) Reproduced with permission from ref 121. Copyright 2016 The Royal Society of Chemistry.

DOI: 10.1021/acs.chemrev.6b00614
Chem. Rev. 2017, 117, 4287−4341

setup with a Mg counter electrode was recently reported.[121] A first discharge capacity of ~200 mAh/g ($Mg_{0.84}Ti_2S_4$) was obtained at 60 °C with capacity retention for more than 40 cycles, as seen in Figure 9c. At an average voltage of ~1.2 V vs Mg and at a density of 3.24 g/cm^3 for spinel-Ti_2S_4,[125] a ~ 200 mAh/g capacity corresponds to an energy content of ~228 Wh/kg and ~731 Wh/l, far above the energy values of the Chevrel (see section 3). The solid solution character observed in both chemical magnesiation experiments by Bruce et al.,[118,119] and the more recent Galvanostatic Intermittent Titration Technique observations (GITT) by Sun et al.[121] fall in excellent agreement with the computed voltage profile of Figure 9b.[124] The strategy adopted to synthesize the metastable spinel Ti_2S_4 phase, less stable than layered-Ti_2S_4 by ~18 meV/atom,[124] was to extract Cu from $CuTi_2S_4$ by chemical oxidation. Reversible Mg intercalation was confirmed by XRD and EDX analysis, indicating retention of the characteristic cubic $Fd\bar{3}m$ symmetry upon magnesiation (Figure 9d), while Rietveld refinement demonstrated that Mg ions occupy both tetrahedral 8*a* (with 20% occupation) and octahedral 16*c* sites (~30%) corresponding to a composition of $Mg[oct]_{0.6}Mg[tet]_{0.19}Cu_{0.1}Ti_2S_4$, in good agreement with the electrochemical capacity reported ($Mg_{0.84}Ti_2S_4$). Complementary DFT-based calculations suggested Mg occupation of the 16*c* sites throughout the $Mg_xTi_2S_4$ solid solution, but the small energy difference between the 16*c* and 8*a* sites could lead to Mg disorder over the two sites, in accordance with experimental XRD observations at $x_{Mg} > 0.5$.[121] Figure 10a shows the activation energy for Mg migration in cubic Ti_2S_4 extracted from the self-diffusion Mg^{2+}(D_{Mg}) coefficients (obtained from GITT measurements), which are in remarkable agreement with values obtained by DFT (~550 meV, as seen in Figure 10b).[121]

In parallel, Sun et al.[123] reversibly intercalated Mg in the layered-TiS_2 phase, utilizing a similar coin-cell setup used previously for the spinel polymorph.[121] The initial discharge capacity of ~270 mAh/g ($Mg_{0.56}TiS_2$, measured at a rate of C/20) was higher than for the spinel-phase (~200 mAh/g for $Mg_{0.80}Ti_2S_4$)[121] at a similar voltage of ~1.2 V. Reversible Mg intercalation was assessed by XRD and EDX characterization measurements. Nevertheless, successive cycles showed a decreased but constant capacity of ~160 mAh/g ($Mg_{0.33}TiS_2$), which varies substantially at different C rates (i.e., ~140 mAh/g at C/10 and ~90 mAh/g at C/5, respectively), indicating some irreversible capacity in the initial cycles. Given that the densities of spinel and layered-TiS_2 are similar,[125,126] the energy content of layered-TiS_2, ~192 Wh/kg and ~623 Wh/l, are comparable to the values of the spinel phase. We note that although the computed voltage curve at 300 K for magnesiated layered-TiS_2 (not shown here)[124] predicted steps at various Mg compositions (x_{Mg} = 1/6, 1/3, and 1/2) that correspond to specific x_{Mg} orderings, only the Mg = 0.33 ordering was observed experimentally.[123]

Nevertheless, qualitative trends indicate higher Mg migration barriers in the layered-TiS_2(~1200 meV) compared to spinel-Ti_2S_4(~800 meV),[124] with more than 50% reduction in barriers possible via volume expansion in the layered phase. Increasing the interlayer distance represents a strategy to improve ion mobility, for instance through insertion of organic molecules which has been achieved previously in layered-V_2O_5,[127] and may be a potential strategy for improving Mg mobility in layered-TiS_2.

In conclusion, successful reversible electrochemical Mg intercalation in the close-packed spinel-Ti_2S_4 gives hope for other chalcogenides, expanding the repertoire of Mg (and MV) cathode materials.[106] The excellent agreement between experimental observation and theoretical prediction gives credibility to first-principles calculations combined with high-throughput methods as a powerful tool to screen novel chalcogenide cathodes.

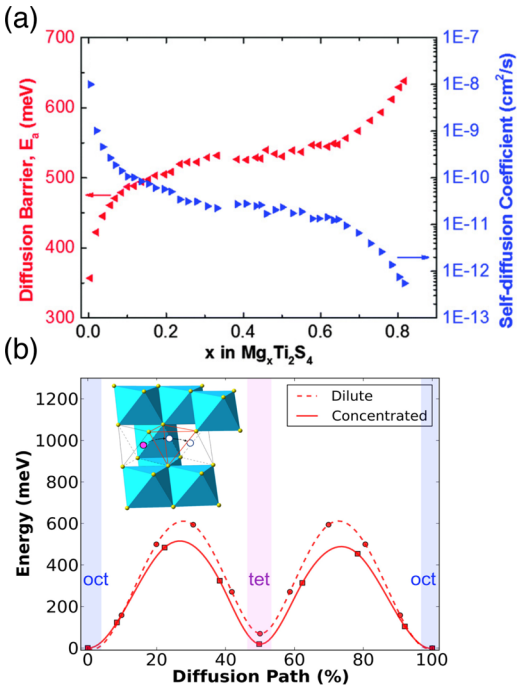

Figure 10. (a) Experimental and (b) theoretical Mg migration energy in spinel-Ti_2S_4 from ref 121. (c) Variation of the energy difference between the octahedral (stable) and tetrahedral (intermediate) sites during Mg migration (for the high vacancy regime) in spinel-Ti_2S_4 at increasing volumes.[124] In (b) migration barriers were computed in the dilute (thick line) and concentrated (dashed line) Mg limits. (a and b) Reproduced with permission from ref 121. Copyright 2016 The Royal Society of Chemistry.

4.2. Other Sulfides

Attempts have been made to reversibly intercalate Mg in both layered[128,129] and 2D MoS_2.[130] Typically, after the first Mg discharge in MoS_2, a substantial capacity fade is observed, and low voltages (typical of sulfides), ~2.0 V and ~0.7 V for 2D and layered-MoS_2, respectively.[128−130] First-principles calculations[129,131,132] of Mg migration in MoS_2 predict that increasing the layer spacing can improve the migration barriers substantially, from 1.22 eV for a layer separation of 6.5 Å to 0.22 eV at 9 Å, similar to the predictions for layered-TiS_2 (see discussion above). Furthermore, Liang et al.[129] demonstrate through experiments that the insertion of polymer molecules (e.g., polyethylene oxide, PEO) to push apart the MoS_2 layers may be a viable strategy to improve Mg diffusivity and hence capacity in MoS_2 (from ~20 mAh/g for pristine-MoS_2 to ~80 mAh/g with polymer intercalated MoS_2).[127] Mg intercalation is not clearly demonstrated with appropriate characterization (e.g., XRD) in these investigations,[128−130] leaving it undecided whether they can function as Mg intercalation compounds. In addition, the typical voltages and capacities observed are low, resulting in energy densities of ~14 Wh/kg and ~70 Wh/l, which are far-off from the desired energy densities outlined in section 2.

DOI: 10.1021/acs.chemrev.6b00614
Chem. Rev. 2017, 117, 4287−4341

4.3. Selenides

Gu et al.[133] attempted to intercalate Mg in layered-$TiSe_2$, reporting a voltage and capacity of ~1.0 V vs Mg/Mg^{2+} and ~108 mAh/g, respectively (Figure 11a), which corresponds to an energy content of ~108 Wh/kg and ~566 Wh/l, respectively. Using a coin-cell with a Mg-metal anode and a Grignard-based [$Mg(AlCl_2EtBu)$:THF] electrolyte, the intercalation of Mg in the layered structure was assessed by monitoring the change in the layer spacing with *in operando* XRD, which indicated a shift of the (004) peaks as a function of Mg content intercalated (Figure 11b). Although it was claimed that 0.83 mol of Mg can be inserted per formula unit of $TiSe_2$ (theoretical capacity for $MgTiSe_2$ is ~260.5 mAh/g), the capacity reported (~108 mAh/g) corresponded only to ~0.41 x_{Mg} insertion. Nevertheless, both the voltage and capacity reported for $TiSe_2$ were similar to what has already been observed for the Chevrel-Mo_6S_8 (~128 mAh/g at 1.1 V).[91]

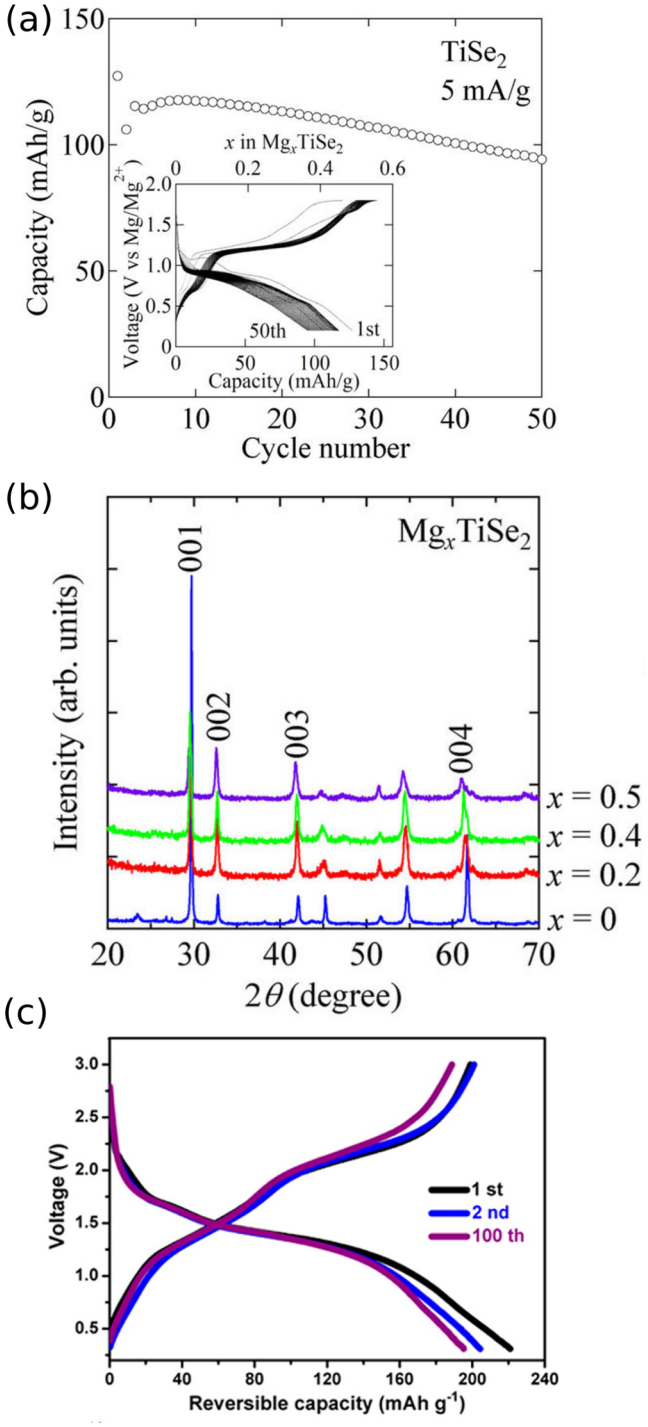

Figure 11. (a) Cyclic voltammetry (CV) and capacity as a function of cycle number and (b) XRD data for Mg intercalation in $TiSe_2$ as reported by Gu et al.[133] (c) Voltage vs capacity for Mg insertion in WSe_2 nanowire from Liu et al.[134] (c) Reprinted from ref 134. Copyright 2013 American Chemical Society.

Similarly, Liu and colleagues[134] reported Mg intercalation in WSe_2 nanowires in a full-cell setup comprising of a Mg-anode and $Mg(AlCl_2EtBu)$:THF electrolyte (see Figure 11c). The authors claimed that Mg can be inserted into the nanowire WSe_2 up to $x_{Mg} = 0.67$ at ~1.6 V and with 203 mAh/g capacity for 160 cycles without appreciable capacity fade, whereas lower capacity accompanied by capacity fade was observed for bulk-WSe_2. Complementary first-principles calculations suggested that the nanowire cathodes could undergo a semiconductor-to-metal transition during Mg insertion, increasing the electrical conductivity of the cathode. Despite the excellent cycling performance reported by the authors (Figure 11c), no spectroscopic characterization of the nanowire WSe_2, at different states of (dis)charge, was presented. Specifically, the operative voltage window used (~0.3—3.0 V) was well above the anodic limit of the electrolyte employed (~2.5 V), which increases the contributions of parasitic electrolyte side reactions. Additionally, as highlighted by Muldoon et al.,[43] the reported amount of Mg intercalated (x_{Mg} = 0.67) corresponds to ~105 mAh/g, which is inconsistent with the reported capacity of 203 mAh/g.[134] Although the gravimetric specific energy of WSe_2 is low (~168 Wh/kg), its high density (~9.39 g/cm^3)[135] sets a volumetric energy of approximately 1578 Wh/l for a ~105 mAh/g capacity.

In summary, a number of sulfide and selenide compounds have been investigated and experimentally attempted as alternative cathodes to the Chevrel structure for MV ion intercalation. These include TiS_2, MoS_2, $TiSe_2$, and WSe_2. Spinel-Ti_2S_4 is by far the only candidate that can reliably intercalate Mg (at ~1.2 V and ~190 mAh/g capacity, as well as ~228 Wh/kg and ~731 Wh/l energy content), demonstrating an energy density approximately twice that of the Chevrel compounds. Additionally, a recent theoretical study on other sulfide spinel compounds as Mg (MV) cathodes[106] indicates favorable Mg mobility at similar predicted energy densities compared to Ti_2S_4, establishing sulfur spinels as a class of compounds that are promising as MV intercalation compounds. In particular, Cr_2S_4 is pointed at in ref 106 as a compound that has favorable voltage, stability, and migration barriers. So far we are not aware of any successful attempts to synthesize and test this compound.

Selenide compounds, such as $TiSe_2$ and WSe_2, which can potentially intercalate Mg (MV) ions with higher mobilities at similar voltages and capacities compared to the Chevrel, are reported to have promising electrochemical performance. However, the actual contribution of Mg intercalation to the electrochemical capacity observed in WSe_2 is unclear, owing to the lack of rigorous characterization data.

Finally, it is worth mentioning that Mg metal combined with a S cathode has recently been considered as a high-energy density technology.[23,39,41,43,136−138] With an experimentally observed capacity of ~300 mAh/g[137] after 20 cycles at a discharge voltage of ~1.65 V (compared to the theoretical

DOI: 10.1021/acs.chemrev.6b00614
Chem. Rev. 2017, 117, 4287−4341

~1671 mAh/g at ~1.89 V[139]), Mg/S systems can achieve energy densities of ~495 Wh/kg and ~990 Wh/l, respectively.[137] While Mg/S can greatly supersede the energy densities of sulfide-based Mg-intercalation systems (e.g., ~192 Wh/kg and ~623 Wh/l, for TiS_2, see discussion above), major obstacles related to the undesired and rapid capacity fade still remain.[23,137]

5. OXIDES

One strategy to improve upon the electrochemical performance of chalcogenide MV batteries is to target intercalation materials with higher theoretical voltage and capacity. The possibility of increasing the intercalation voltage by switching the anion species from sulfur to oxygen[116] and increasing the theoretical capacity by considering structures with a higher ratio of intercalant to transition metal makes oxide materials especially appealing as MV cathode materials. Previously, this approach was successfully implemented in the development of Li-ion cathode materials, which began with $LiTiS_2$[115,117] and led to today's commercial oxide-based cathode materials (e.g., $LiCoO_2$ and NMC333).[140] To go beyond the performance of Chevrel cathodes, it is not sufficient to only identify candidate MV host systems that possess high theoretical voltage and capacity, but the material must also be synthesizable, allow MV-intercalation at reasonable rates, and be stable over many electrochemical cycles. An additional challenge for identifying good MV cathodes comes from the limited stability of MV-ion electrolytes against high-voltage MV cathode materials,[24,31,32,38,39,43,141] which is an ongoing and parallel research challenge that sometimes prevents reliable electrochemical data from being extracted in MV systems. The general considerations and challenges associated with MV intercalation in oxide hosts is discussed below.

Mobility

Based on extensive research on Li^+-ion conductors,[113] which consistently show sulfides to have much better Li^+ mobility than oxides, one would expect Mg^{2+} mobility to decrease similarly when switching from sulfides to oxides. Indeed, the limited mobility of MV ions in oxide host structures is generally considered the chief obstacle in finding an oxide cathode capable of supplanting sulfides.[72,142] Requirements for reasonable battery performance allow us to establish minimal values for MV ion mobility. For a given (dis)charge time t, the cathode particle size will determine a maximum tolerable barrier (E_m) for MV ion migration, since the diffusion length scales as $\sqrt{Dt}$ (where D is the diffusivity). Here, the radius of a spherical particle is used as the required diffusion length. We approximate the diffusivity D as $D \approx \nu \times a^2 \times \exp(-E_m/kT)$, where ν is the atomic jump frequency and a is the atomic jump distance. Assuming (reasonable) values of 10^{12} s^{-1} for ν and 3 Å for a, the relationship between E_m and the maximum particle size feasible for MV ion extraction is displayed in Figure 12 for several charging rates. In discussing the process of (dis)charge, current is often expressed as a C-rate in order to normalize against the electrode capacity.

The C-rate measures the rate at which the material is discharged relative to its maximum capacity, and 1C indicates a complete discharge of a battery in 1 h. Therefore, the C-rate is defined independently of the volumetric capacity (Ah/l) of the cathode under consideration. As such, a material with twice the (volumetric) capacity will require twice as much current at the same C-rate, which directly translates to twice the ionic flux

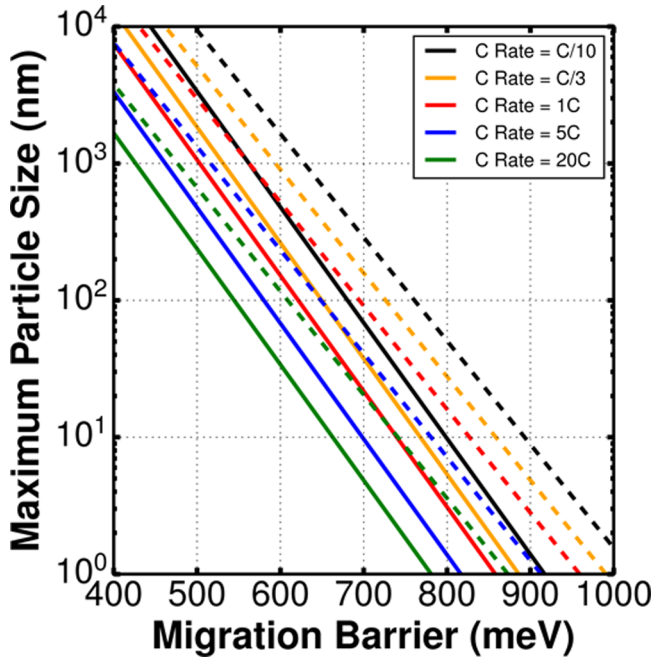

Figure 12. Relationship between MV ion migration barrier E_m and the maximum particle size permitting reasonable diffusivity in the context of battery performance. Various charging rates are displayed and color-coded as indicated in the figure legend. Solid lines indicate the relationship between migration barrier and particle size at 298 K, while dashed lines indicate 333 K.

needed at the particle surfaces. Consider Fick's 1st law, $J = -D\frac{dc}{dx}$, where J is the ionic flux (in mol cm^{-2} s^{-1}), D the ionic diffusivity (cm^2 s^{-1}), c the ionic concentration (mol cm^{-3}), and x is distance (cm). A material with twice the volumetric capacity will have twice the concentration of the redox species throughout the material. This in turn doubles the concentration gradient(s) throughout the material which subsequently doubles the ionic flux (and the current), at the same value of ionic diffusivity. As a result, under Fickian diffusion conditions, two materials that have the same ionic migration barrier (E_m) will discharge at the same C-rate irrespective of the volumetric capacity. Therefore, our analysis in Figure 12 considers the upper limit of migration barriers at which a steady-state ionic diffusion can occur throughout a cathode particle of a given size, in a specified time interval (as implied by the C-rate), which is independent of volumetric capacity.

For a primary particle size of ≈100 nm, charge rates of C/3 (as in the USABC for electric vehicles[81]) can be obtained for migration barriers in the 600−750 meV range and below. Of course, this criterion implies that no other kinetic factors such as desolvation and charge transfer across the electrolyte/electrode interface, or phase boundary motion in the case of two-phase electrode reactions, are rate-limiting. With these assumptions in place, Figure 12 displays the maximum particle size (y axis) which would permit ion extraction against a particular barrier (x axis). Curves are shown for multiple charging rates and temperatures. Considering the generally low mobility of MV ions in oxide hosts, the relationship in Figure 12 demonstrates the potential importance of nanosizing as a means to achieve viable MV battery cathodes. However, pseudocapacitive contributions to capacity will naturally be more prominent when high surface-area electrodes are

DOI: 10.1021/acs.chemrev.6b00614
Chem. Rev. 2017, 117, 4287−4341

employed, and must be carefully considered when discussing measured values.[143,144] The advantages and drawbacks of nanostructured electrodes are discussed in more detail later in the review.

Solvent Cointercalation

A commonly adopted strategy to enhance MV ion mobility is by incorporating shielding water molecules in the structure, either by cointercalation or directly in synthesis. Although the findings of water intercalation aiding Mg insertion in various cathode materials, such as layered MoO_3, xerogel-V_2O_5, birnessite, and spinel-MnO_2, are exciting (see respective sections), the observed improvements in capacity and kinetics could indicate the occurrence of proton (or hydronium) intercalation[145] in these cathode materials, highlighting the need for critical interpretation of the experimental results. From the experimental studies discussed in the following sections, it is not clear whether water actively participates in electrochemical reactions, the potential for electrochemical decomposition of water (according to $2H_2O \rightarrow O_2 + 4H^+ + 4e^-$) is only approximately −1.229 V vs standard hydrogen electrode (SHE). In addition, there has been no clarification with vibrational spectroscopy methods on whether structural water exists in the form of OH^- and H^+ adsorbed on the oxide surfaces, thus creating a source of readily cyclable ions. Proton cycling can also possibly explain the excess capacity reported for organic electrolytes mixed with increasing water concentrations.[146,147] While thermodynamic models can clarify voltage dependencies and driving forces for water cointercalation in cathodes, it is challenging for theoretical frameworks to explain observed variabilities in capacities with electrolytic water content. Even if water is not directly involved in any redox reactions, but simply aids Mg intercalation, strategies to avoid water contact with the Mg-metal anode need to be envisioned before water addition to the system would become practical. If solvent cointercalation can indeed promote Mg^{2+} mobility then research should focus on the incorporation of stable solvent in solutions which do not lead to spurious side reactions in the electrochemistry and do not passivate the Mg metal anode.

Conversion Reactions

In addition to poor MV-ion mobility, another issue that can afflict oxide intercalation hosts is the tendency to undergo irreversible oxide conversion reactions instead of reversible MV intercalation. The occurrence of undesired conversion reactions as opposed to MV intercalation can be rationalized in terms of competing thermodynamic forces, largely driven by the very low free energy of MgO formation. For example, Figure 13 shows the competition between intercalation and conversion reactions for one mole of Mg reacting (i.e., a 2 electron transfer) with a mole of transition metal oxide (TMO_2), where the average voltages are V_{conv} and V_{int} (with respect to Mg metal), respectively.

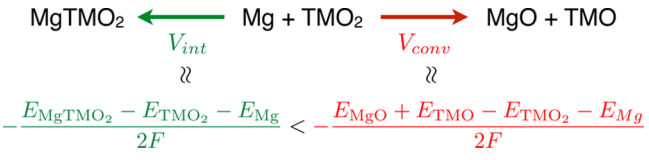

Figure 13. Schematic of competing intercalation and conversion reactions for a 2 electron transfer process with Mg. $E_{species}$ is the internal energy of a species from DFT calculations and F the Faraday constant.

$E_{species}$ in Figure 13 is the free energy of the species at 298 K, and approximated as the internal energy at 0 K computed by DFT,[116,148] with F the Faraday constant. If $V_{conv} > V_{int}$, the conversion reaction is thermodynamically favored against the desired MV intercalation, and vice versa if $V_{int} > V_{conv}$. Generally, MV ions form their respective oxides at a comparable voltage to Li, while intercalating at lower voltages. For example, Mg and Ca react with O_2 to form MgO at ∼3.16 V vs Mg and CaO ∼ 3.35 V vs Ca, respectively, compared to ∼3.15 V vs Li for the formation of Li_2O, which are obtained from the experimental free energies tabulated by Kubaschewski and Alcock.[139] Thus, the oxide formation voltage is similar for MgO and Li_2O, even though Li^+ is ∼0.7 V lower than Mg^{2+} on the SHE scale. This reflects the tremendous thermodynamic stability of MgO compared to the other oxides. The competition with conversion reaction is less of an issue for Ca^{2+}, given that Ca^{2+} is only ∼0.2 V lower than Li^+ vs SHE. In TMO_2 cathodes, the chemical potential of oxygen is set by the energy difference between the TMO_2 and TMO (reduced) specie, which quantifies the ability of the TMO_2 host to transfer oxygen to the working ion. Thus, MV intercalation reactions must compete against the formation of highly stable oxides.

Figure 14 charts the competing nature of conversion (V_{conv}) and intercalation (V_{int}) reactions of several transition metal oxides (MoO_3, V_2O_5, and several layered and spinel TMO_2) for Li^+ and MV ions (Mg^{2+}, Ca^{2+}, and Zn^{2+}) obtained by utilizing the lowest DFT energies from the Materials Project database,[149] to construct intercalation voltages and conversion reaction paths.

Trends in Figure 14 indicate that while both Li and MV ions are not expected to undergo conversion in most 1 electron reduction processes (i.e., 1 mol of Li or 0.5 mol of MV, left panel), MV conversion is preferred when two electrons are transferred per TM (i.e., 1 mol of MV, right panel). This does not necessarily imply that conversion will take place, as many Li^+ intercalation states are metastable, but it does require a reliance on kinetic stabilization. Additionally, the voltage difference between intercalation and conversion reactions ($V_{int} - V_{conv}$, width of green bars in the left panel of Figure 14) is nominally higher for Li than for MV ions, making Li-intercalation cathodes very tolerant to degradation due to local polarization, which could potentially drop the actual potential below V_{conv}.

While most MV ions are not expected to undergo conversion reactions in most oxide hosts at low MV content (or $1e^-$ reduction), local accumulation of MV ions can occur during intercalation due to poor MV mobility. A significant increase in local concentration of MV ions (and the number of electrons transferred locally) can indeed result in local conversion reactions, given the tendency for most transition metal oxides to convert at high MV content (Figure 14, right panel). This analysis points at a key challenge for Mg^{2+} intercalation in oxides. Even though its intercalation kinetics is expected to be much worse than Li^+, its tolerant polarization window upon discharge is considerably smaller than for Li^+ intercalation due to the very negative formation energy of MgO. To compound the problem, MgO is considered to have extremely low mobility for Mg^{2+} ions.[150] While this has never been proven rigorously, the difficulty in operating Mg metal anodes is attributed to the ease by which a blocking MgO layer forms on it in many solvents.[13] While still present, the conversion challenge seems to be less of an issue for Ca^{2+}, particularly in hosts such as V_2O_5 and MoO_3.

DOI: 10.1021/acs.chemrev.6b00614
Chem. Rev. 2017, 117, 4287−4341

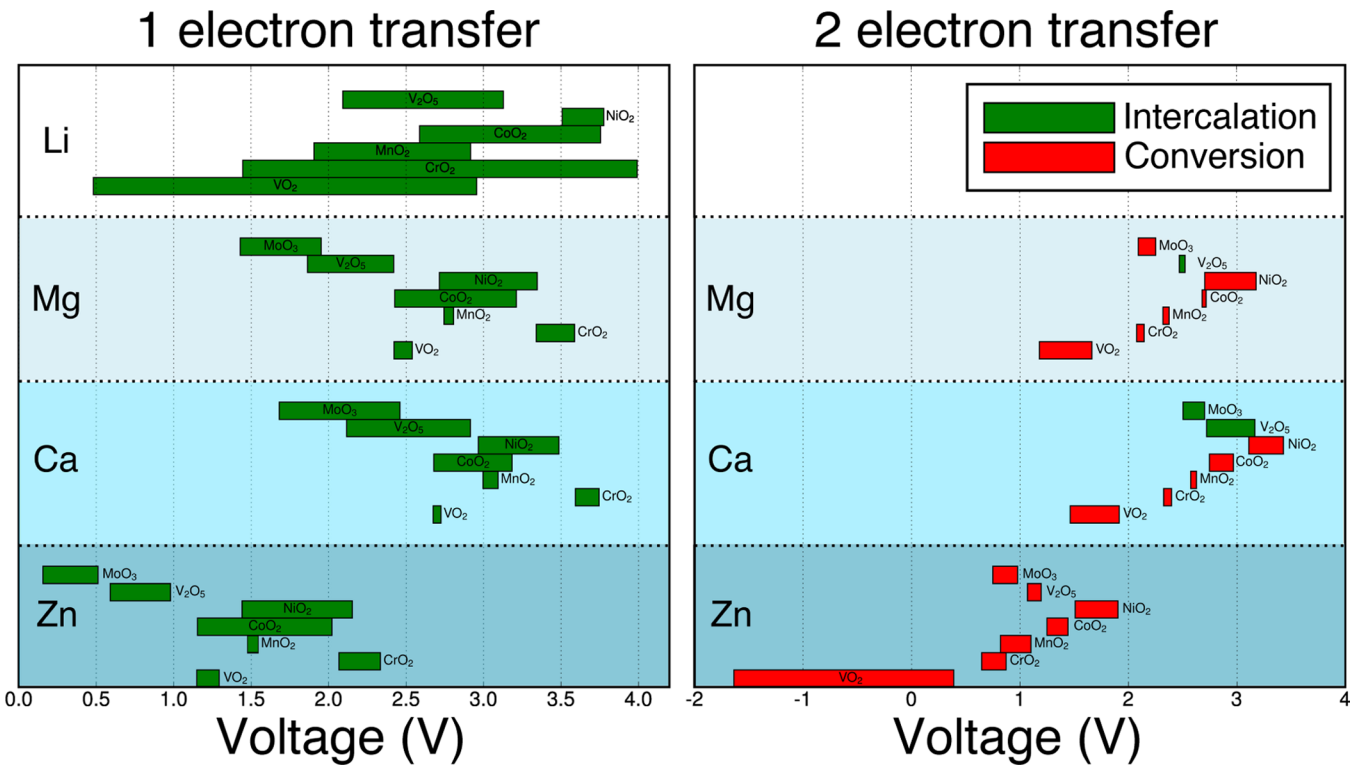

Figure 14. Competition between intercalation and oxide conversion reactions for Li, Mg, Ca, and Zn, as quantified by V_{int} and V_{conv} of Figure 13. For the green bars, the minimum voltage (left of the bar) is V_{conv}, while V_{int} is the maximum (right of the bar). In this condition, intercalation is preferred since $V_{int} > V_{conv}$. Similarly, red bars signify conversion as V_{conv} (maximum of the bar) is greater than V_{int} (minimum). Left and the right panels are for 1 electron (e.g., $TM^{4+} \rightarrow TM^{3+}$) and 2 electron (e.g., $TM^{4+} \rightarrow TM^{2+}$) redox processes, respectively.

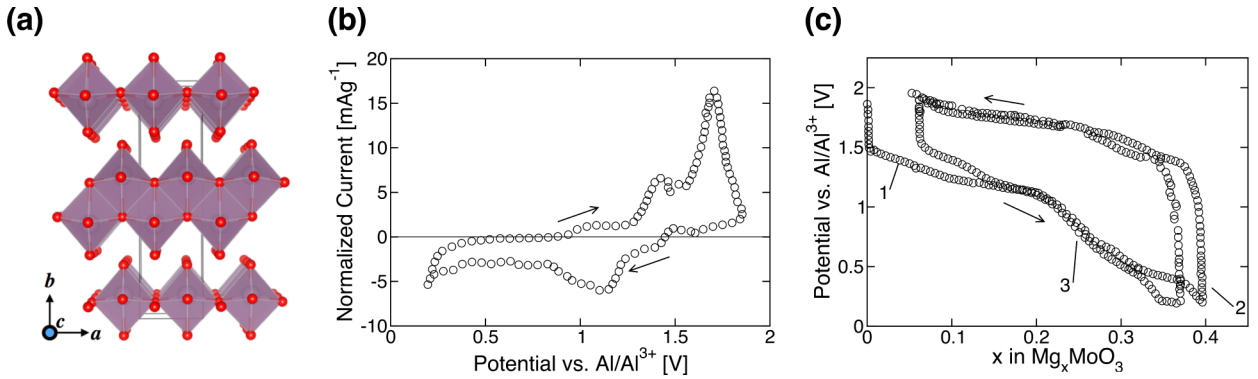

Figure 15. (a) Crystal structure of layered MoO_3 (with Mo ions in violet six-coordinated by oxygens in red); layers stack along the *b* axis. (b) Cyclic voltammogram of Mg intercalation in MoO_3 and (c) first three galvanostatic Mg cycles in MoO_3 using $MgCl_2$:EMIC:$AlCl_3$ electrolyte (with EMIC as 1-ethyl-3-methylimidazolium chloride), respectively. (b and c) Redigitized and adapted with permission from ref 151. Copyright 1995 Elsevier.

Note that for the purpose of plotting Figure 14, we considered only the formation of Li_2O_2 in Li-TMO_2 systems and other simple oxide reduction reactions, such as $TMO_2 \rightarrow$ TMO, while there could be other competing conversion reactions that could impact the trends in Figure 14 (such as the formation of Li_2O in Li-TMO_2 and $MgVO_3$ in Mg-V_2O_5). Since the formation of Li_2O_2 (~3.38 V) occurs at a higher voltage compared to Li_2O (~3.15 V),[139] we adopted Li_2O_2 as the compound of choice for conversion reactions of Li in Figure 14, but the qualitative trends should not change if Li_2O is considered as the conversion product. Also, the cathode materials could undergo (ir)reversible phase transformations during intercalation, which could influence the energetics, such as $\alpha \leftrightarrow \delta$ in Li-V_2O_5 and spinel $\rightarrow$ layered or spinel $\rightarrow$ rock-salt in Mg-oxide spinels (see discussion later). These considerations suggest that careful interpretation of the observed electrochemical and structural data is always required, and rigorous analysis of characterization measurements (XRD and other spectroscopic techniques) is a must to check for conversion products.

The section continues by discussing the intercalation of MV ions (mostly Mg and Zn) into promising layered oxides such as MoO_3 and V_2O_5. The analysis then moves onto the vast space of MnO_2 polymorphs that encompasses compact, layered, and hollow structures. The oxide section terminates by discussing the chemical space of transition metal spinels and their high-pressure phases, the so-called postspinels.

DOI: 10.1021/acs.chemrev.6b00614
Chem. Rev. 2017, 117, 4287−4341

5.1. Layered MoO_3

Among the proposed host materials for Mg^{2+} intercalation, layered α-MoO_3 offers one of the highest theoretical capacities, with ~372.3 mAh/g (for 2 electrons, $Mo^{4+} \leftrightarrow Mo^{6+}$). With multiple reports of measured capacity in excess of 200 mAh/g at an average voltage of 2.25 V,[62,151] layered MoO_3 has also exhibited one of the highest attainable capacities for Mg^{2+} intercalation. For example, a capacity of ~220 mAh/g at 2.25 V corresponds to an energy content of ~495 Wh/kg and ~2332 Wh/l, respectively, which is approximately six times greater than the state-of-the-art Chevrel cathode. Furthermore, Mg^{2+} intercalation has been shown to be at least partly reversible,[62,152] creating a great deal of interest in this material as a multivalent electrode. Despite the promising theoretical capacity of this material, α-MoO_3 is plagued by sluggish diffusion kinetics and demonstrations of reversible Mg^{2+} insertion/removal have typically required nanoscale films of MoO_3 to facilitate ionic mobility.[62,152,153]

The layered structure of α-MoO_3, displayed in Figure 15a appears suitable for cation intercalation. Double layers of MoO_3, which comprise of covalently bonded edge and corner sharing MoO_6 octahedra,[151] are held together by weak van der Waals forces, with an interlayer distance determined by XRD to be ~6.929 Å.[151]

Like the Chevrel-phase materials, α-MoO_3 was initially studied as a cathode for Li-ion batteries[154] and showed reversible Li^+ intercalation at a voltage of ~2.7 V with a capacity of ~300 mAh/g. More than 20 years later, a comparative study by Spahr et al.[151] of Li^+ and Mg^{2+} intercalation into α-MoO_3 reported for the first time Mg^{2+} intercalation into this material. Using a dry $AlCl_3$/EMIC/$MgCl_2$ (with EMIC as 1-ethyl-3-methylimidazolium chloride) electrolyte and Mg metal counter electrode, a first discharge capacity of ~160 mAh/g was observed, although this capacity faded below 100 mAh/g within four cycles.[151] Similar capacity fading was also observed for Li^+ cycling in multiple studies.[151,154] Generally, the observed capacity fade is attributed to structural changes in the host during cycling. This explanation is supported by complex shape changes in potentiostatic and galvanostatic curves for Mg^{2+} intercalation, as shown in Figure 15 (panels b and c, respectively). It is worth remarking that side reactions between electrolyte and electrode materials may also produce such curve changes.

The precise influence of the electrolyte on MoO_3 cycling remains ambiguous. While previous work reports no electrochemical activity with electrolytes based on propylene carbonate (PC),[151] later studies obtain non-negligible discharge capacity using various Mg salts [i.e., $Mg(TFSI)_2$[155] and $Mg(ClO_4)_2$],[152,153] where TFSI for bis(trifluoromethane)-sulfonimide) dissolved in PC. Although a recent report finds no electrochemical activity using $Mg(TFSI)_2$ dissolved in ACN as an electrolyte, Gershinsky et al.[62] report promising cycling behavior, which is discussed below, using the same electrolyte together with a Mg metal as counter and quasi-reference electrodes made of activated carbon cloth attached to a Pt wire. Even though the electrolyte can clearly influence intercalation and cycling, no systematic study of electrolytes exists in the context of α-MoO_3.

Utilization of a "wet" electrolyte seemingly improves both the capacity and cycling stability of α-MoO_3. For the intercalation of Mg^{2+} from 1 M $Mg(ClO_4)_2$ in acetonitrile with 3 mol % H_2O (and the same electrochemical setup), Spahr and co-workers[151] reported an improved first-discharge capacity of ~210 mAh/g followed by a decrease to ~155 mAh/g over 14 cycles.[151] Despite the higher capacity observed in this case, drastic changes in the shape of successive cyclic voltammetry curves suggest that irreversible structural changes in the host also occur with the wet electrolyte. A possible reason for the improvement in capacity is the attenuation of the strong polarization induced in the host lattice by a divalent intercalating ion. However, as the work by Spahr et al.[151] does not present a comparative study with Li^+ (which would presumably experience relatively less attenuation owing to its smaller charge density) nor does it provide structural analysis proving Mg^{2+} intercalation, it is impossible to rule out the intercalation of protons (resulting from electrolyte degradation) as the source of this additional capacity. Furthermore, water-containing solvents are inappropriate against Mg-metal anodes, as they are a potential source of irreversible passivation.[156] The use of solvent molecules to attenuate host polarization due to divalent intercalants is an important topic for many potential cathode materials and is discussed with greater depth in the xerogel-V_2O_5 and MnO_2 sections. Attempts to draw conclusions about the impact of the electrolyte from existing studies are obfuscated by the usage of varying electrode geometries, such as thin-films, bulk powders, the choice of electrolyte, and current collectors. As we detail below, factors such as particle size and electrode preparation can also significantly affect cycling behavior and observed capacity.

Reports utilizing electrodes pressed from MoO_3 powders have typically exhibited significant capacity fade and poor cycling kinetics.[151,154] Furthermore, these studies have not provided structural evidence of Mg^{2+} intercalation, making it difficult to exclude other sources of capacity such as solvent/proton intercalation. Compelling evidence of Mg^{2+} intercalation has been shown in more recent studies using a thin film electrode having an ~100 nm thickness.[62,152,153] The use of a thin film electrode provides high relative surface area and reduces the diffusion path for extraction of the intercalating ion, mitigating somewhat the sluggish kinetics suggested by earlier studies.[151,154] The thin film geometry also provides the additional benefit of eliminating other potentially obscuring factors such as carbon, binder, and substrate. Caution is warranted as reversible capacity observed for thin-film electrodes can be a result of pseudocapacative phenomena stemming from the large surface-to-volume ratio of the nanoscale film.[157]

Multiple studies report an increase in the XRD-derived interlayer spacing of thin-film α-MoO_3 following discharge in the presence of a Mg-containing electrolyte as shown in Figure 16.[62,152,153] Increases in the interlayer spacing were also found to be mostly (although incompletely) reversed by demagnesiation.[152,153] A later report by Gershinsky et al.[62] finds a complete return of the (020) reflection peak (indicative of the interlayer spacing) to its original position (Figure 16) during charge, although Raman measurements (in the same report) suggest that some Mg nevertheless remains in the structure. Because XRD is primarily sensitive to bulk materials and Raman spectroscopy has a comparatively higher surface sensitivity, the observation of remnant Mg in the charged material by Raman spectroscopy (and not XRD) indicates Mg buildup near particle surfaces, likely indicative of poor diffusion in the bulk material, and perhaps the occurrence of conversion reactions as observed in some MnO_2 polymorphs upon Mg intercalation.[158] Using energy dispersive spectroscopy (EDS), Gershinksy and co-workers[62] also carried out an elemental analysis of α-MoO_3

DOI: 10.1021/acs.chemrev.6b00614
Chem. Rev. 2017, 117, 4287−4341

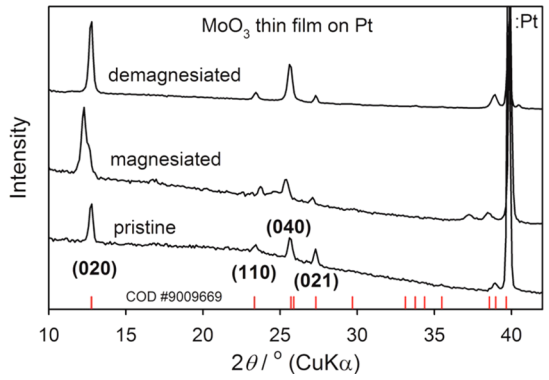

Figure 16. XRD of pristine, magnesiated (x_{Mg} = 0.5), and demagnesiated MoO_3 thin-film electrodes from ref 62. Reprinted from ref 62. Copyright 2013 American Chemical Society.

films before and after Mg discharge and observed the presence of Mg in the latter, but it is worth noting that EDS provides poor differentiation of surface and bulk Mg (a fact the authors readily acknowledge). Furthermore, these studies utilized a dry electrolyte, reducing the probability of proton intercalation. Considering these thin film results, it is reasonable to conclude that reversible intercalation of Mg^{2+} into α-MoO_3 does occur, albeit with sluggish diffusion kinetics.

The thin film electrodes described above exhibit superior cycling performance and capacity relative to pressed powders. While Sian and co-workers do not report charge/discharge capacity values, their study presents cyclic voltammetry (CV) data which remains unchanged for 200 cycles.[152] Gershinsky et al.[62] reported capacities of ~220 mAh/g with more than 95% Coulombic efficiency for more than 20 cycles, indicating reversibility of the intercalation reaction. Despite promising capacity values and evidence of cycling stability, thin films of α-MoO_3 still exhibit slow diffusion kinetics, as evidenced by significant overpotentials observed for Mg insertion/removal.[62,152]

Spectroscopic studies provide some evidence as to the microscopic origins of sluggish kinetics. Core-level photoemission spectra presented by Sian et al.[152] indicate that only Mo^{6+} is present in pristine films of α-MoO_3. Films intercalated by Mg^{2+} exhibited a range of oxidation states (from +3 to +6), suggesting a variety of local environments for Mo ions. In a more recent study, the same group monitored optical absorption features associated with Mo^{4+} and Mo^{5+} in films annealed at various temperatures.[153] A higher relative amount of Mo^{4+} was observed in films annealed at higher temperatures, attributed by the authors to buildup of Mg at grain boundaries (present in larger amounts in high temperature films), a correlation supported by transmission electron microscopy (TEM) analysis of such films.[153]

Recently, Incorvati et al.[155] attempted Mg^{2+} intercalation in a fluorinated α-MoO_3 structure having the stoichiometry α-$MoO_{2.8}F_{0.2}$ (the only fluorinated composition found to retain the α-MoO_3 structure). Ideally fluorination can mildly reduce the MoO_3 lattice, possibly improving electrical conductivity of the host material as well as Mg diffusivity via reduced electrostatic repulsion. The intercalation of Mg in α-$MoO_{2.8}F_{0.2}$[155] was assessed using XRD, solid-state ^{25}Mg nuclear magnetic resonance (NMR) and first-principles calculations. As in prior studies,[62,152,153] interlayer spacings derived from XRD analysis increase by roughly 3% with discharge, consistent with Mg insertion, and are found to return to their original spacing upon charging. Although the interpretation of ^{25}Mg NMR is very challenging, a broad peak at ~50 ppm in the NMR spectrum of the discharged compound ($Mg_x[MoO_{2.8}F_{0.2}]$) could indicate Mg intercalation. Nevertheless, this measurement was only benchmarked against the ^{25}Mg NMR spectrum of the model compound $Mg_2Mo_3O_8$, a completely different structure to α-MoO_3. In addition, some of the ^{25}Mg NMR peaks at ~26 ppm resemble a typical MgO response, which the authors claim are a result of exposure of the sample to air. However, it is possible that MgO forms as a product of irreversible conversion reactions upon Mg intercalation, as has already been observed for other oxide cathodes.[158] Incorvati and co-workers reported a first-discharge capacity of ~40 mAh/g for the fluorinated material, which increases to ~70 mAh/g with further cycling and shows stability for 18 cycles.[155] While these capacities are lower than those observed in earlier reports,[62,152] it is worth noting that earlier studies utilized thin-films of α-MoO_3 as electrodes, whereas Incorvati et al. make use of an electrode pressed from a ball-milled powder, yielding micrometer-sized particles much larger than the nanosized particles utilized in Gershinsky's work. Furthermore, the same study[155] reports a first-discharge capacity of ~10 mAh/g for micron-sized α-MoO_3, which fades rapidly, indicating that fluorination may nevertheless be a viable strategy for improving the performance of this material.

α-MoO_3 is one of only a handful of oxide materials to show reversible Mg^{2+} intercalation behavior, along with some V_2O_5 and MnO_2 polymorphs (see later sections). With numerous works reporting capacities in excess of 200 mAh/g stable for multiple cycles,[62,152] this material remains a promising cathode candidate. However, all studies report some degree of irreversibility, and long-term cycle stability has only been demonstrated in thin films.[62,152,153] None of the studies utilizing electrodes pressed from powders have demonstrated capacities exceeding 200 mAh/g without utilizing a "wet" electrolyte,[151] and in these cases, proton intercalation has not been ruled out as a source of capacity. From Raman and NMR measurements,[62,155] it is not possible to exclude the occurrence of deleterious conversion reactions at the surface of the α-MoO_3 particles during Mg discharge, a phenomenon already reported for other oxide materials.[158] Nevertheless, variations in electrolyte formulation and electrode geometry have yielded a ~100% increase in attainable capacity for Mg^{2+} intercalation into α-MoO_3, and chemical fluorination of the host lattice has been shown to improve cycling performance as compared to the unmodified material.[155] These improvements provide some hope that good cycling behavior and large capacities may yet be obtained from this material, and as one of few oxides to exhibit reversible Mg^{2+} intercalation, it is worth investigating whether modifications similar to those detailed above can enable this material to achieve its theoretical potential.

Other Mo Oxides. A mixed Mo−V microporous material having the stoichiometry $Mg_xMo_{2.5+y}VO_{9+\delta}$ was recently investigated, with some success, as a Mg intercalation cathode.[159] Elemental analysis revealed the exact composition used in the study to be $Mo_{2.48}VO_{9.93}$. Electrochemical insertion of Mg was attempted in a 3-electrode cell setup with activated carbon cloth for the counter and reference electrodes. $Mg(TFSI)_2$ in ACN was used as the electrolyte. These experiments yielded a first discharge capacity of ~397 mAh/g at a rate of C/70 and an average voltage of 2.5 V. The capacity decreases with cycling and stabilizes at ~235 mAh/g for at least 15 cycles, corresponding to energy contents of ~587 Wh/kg

DOI: 10.1021/acs.chemrev.6b00614
Chem. Rev. 2017, 117, 4287−4341

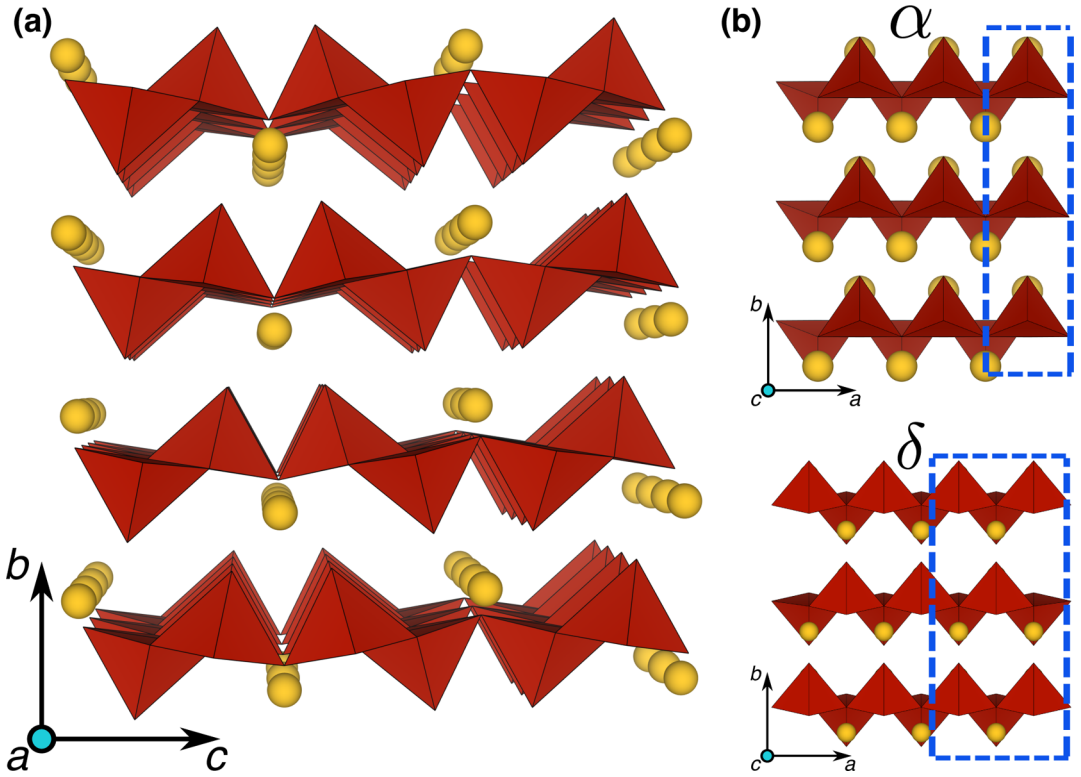

Figure 17. (a) Displays the structure of orthorhombic V_2O_5, with the red pyramids indicating VO_5 polyhedra and the yellow spheres corresponding to the intercalant atoms. (b) Illustrates the difference between the alpha and delta polymorphs of orthorhombic V_2O_5.[170] (a and b) Reproduced from ref 170. Copyright 2015 The Royal Society of Chemistry.

and ~2344 Wh/l. The authors speculatively assign the capacity loss to Mg trapped in small, three-membered tunnels, but do not further investigate the issue.[159] The attainable capacity drops markedly to ~114 mAh/g and 90 mAh/g at rates of C/40 and C/12, respectively. The sensitivity of the practical capacity to charging rate, and possible Mg trapping in the material suggest slow diffusion of Mg.

XRD analysis of chemically magnesiated $Mg_xMo_{2.48}VO_{9.93}$ at various states of magnesiation ($0 < x < 3$) reveals continuous peak shifts with increasing Mg concentration, indicative of an intercalation (rather than conversion) reaction. Structural refinement suggests an increase of the *a* and *b* lattice parameters with the *c* parameter remaining largely unchanged. This indicates that some structural rearrangement occurs. Electrochemical cycle stability nevertheless indicates reversible Mg intercalation, although careful analysis of electrochemically discharged and charged samples would be required to prove this point. Although the work of Kaveevivitchai et al.[159] suggests that Mg mobility in the material is potentially low, $Mo_{2.5+y}VO_\delta$ likely warrants further theoretical and experimental investigation in light of its high capacity and cycle stability.

Unsuccessful electrochemical experiments have also been reported for MV (de)intercalation in Mo-oxides, such as Mg and Ca removal from layered-$Mg_2Mo_3O_8$[160] and perovskite-$CaMoO_3$,[161] respectively. While chemical extraction of Mg was possible in $Mg_2Mo_3O_8$, no electrochemical activity was observed, which the authors attributed to the high Mg migration barriers induced by the "dumbbell" O−Mg−O transition state during Mg diffusion.[160] Perovskite-$CaMoO_3$ was theoretically evaluated as the best candidate for Ca cycling among several MO_3 perovskite structures (with M = Mn, Cr, Fe, Co, Ni, and Mo) based on first-principles average voltage and volumetric strain calculations.[161] However, no electrochemical activity was observed on charging $CaMoO_3$, in agreement with the calculated high Ca migration barriers.[161] The aforementioned works indicate the important role played by ab initio calculations in screening for false candidates.

5.2. Layered V_2O_5

Orthorhombic-V_2O_5. Although the volume of research published on MV intercalation materials pales in comparison to the Li-ion battery literature, Mg (and MV) intercalation in orthorhombic V_2O_5 is one of the few oxide materials (apart from MoO_3 and MnO_2) that has received focused attention in the literature. Similar to the Chevrel, orthorhombic V_2O_5 has been reported to electrochemically intercalate several MV-ions,[162,163] including Mg^{2+}, Ca^{2+}, and Y^{3+}, albeit with limited experimental evidence for Ca^{2+} insertion.[162,164] Multiple moles of Li can be intercalated per V_2O_5 formula unit with a reversible capacity of ~130 mAh/g at ~3.3 V,[162,165−167] while various $Li_xV_2O_5$ polymorphs, such as α ($x_{Li} \sim 0.0$), ϵ ($0.4 < x_{Li} < 0.7$), δ ($x_{Li} \sim 1.0$), γ ($1.0 < x_{Li} < 2.0$), and ω ($2.0 < x_{Li} < 3.0$), have been characterized using both XRD[165,167] and neutron diffraction[168] measurements on discharged samples. Thus, the potentially high energy densities (~660 Wh/kg and ~2335 Wh/l) that the material can achieve by reversibly intercalating one mole of Mg (capacity ~294.7 mAh/g at a theoretical voltage of ~2.5 V[169,170]) or other MV ions have made V_2O_5 a material of interest in MV cathode studies. Nevertheless, most electrochemical Mg insertion experiments into orthorhombic V_2O_5 have suffered from poor kinetics,[141,171] typically attributed to sluggish Mg diffusion into the cathode host, with successful intercalation experiments employing either nanosized V_2O_5 particles,[62,162] solvent (water) cointercalation,[146,171] or high temperatures[172] to improve Mg diffusivity.

DOI: 10.1021/acs.chemrev.6b00614
Chem. Rev. 2017, 117, 4287−4341

The crystal structures of the α and δ polymorphs orthorhombic V_2O_5 are illustrated in Figure 17. The V_2O_5 lattice is comprised of layers of alternating edge- and corner-sharing VO_5 pyramids, as indicated by the red polyhedra in Figure 17, with the intercalant atoms (yellow spheres) located between the layers. Differentiation of the α and δ polymorphs arises through changes in the stacking of layers along the *a*-direction (perpendicular to the *b*-*c* plane shown in Figure 17a), orthorhombic as highlighted by the dashed blue rectangles in Figure 17b. While $Li_xV_2O_5$ undergoes irreversible $\delta \rightarrow \gamma$ and $\gamma \rightarrow \omega$ transformations for $x_{Li} > 1$ and $x_{Li} > 2$, respectively,[167] the γ and ω polymorphs have not yet been reported in the Mg (MV)-V_2O_5 system.

In 1987, Pereira-Ramos et al.[172] first demonstrated reversible electrochemical Mg intercalation into orthorhombic V_2O_5 at 150 °C, intercalating up to $x_{Mg} \sim 0.5$ (~130 mAh/g) at a low rate of 100 μA/cm^2. XRD analysis of discharged samples (at $x_{Mg} \sim 0.2$) revealed minor peak shifts, similar to those observed at $Li_{0.45}V_2O_5$. Further refinement of the XRD data revealed a slight expansion of the lattice along the *b*-direction, consistent with later experimental observations (Figure 18b)[62] and theoretical predictions (see Figure 19b).[169] In 1990, Gregory et al.[53] reported chemical insertion into V_2O_5 up to $x_{Mg} \sim 0.66$, using a 0.7 M dibutyl-magnesium in heptane as electrolyte but provided no characterization-based evidence of Mg-intercalation. Both the aforementioned experiments[53,172] reported Mg intercalation only under nonambient electrochemical conditions, such as high temperature or direct chemical reaction.

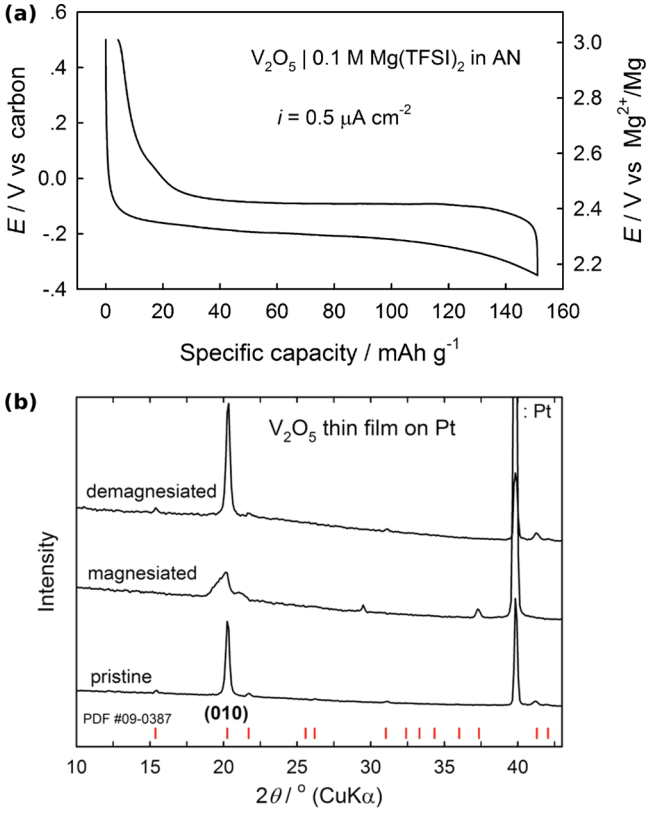

Figure 18. (a) Experimental voltage curve for Mg cycling in orthorhombic V_2O_5 and (b) XRD measurements on pristine, discharged, and charged samples by Gershinsky et al.[62] (a and b) Reprinted with permission from ref 62. Copyright 2013 American Chemical Society.

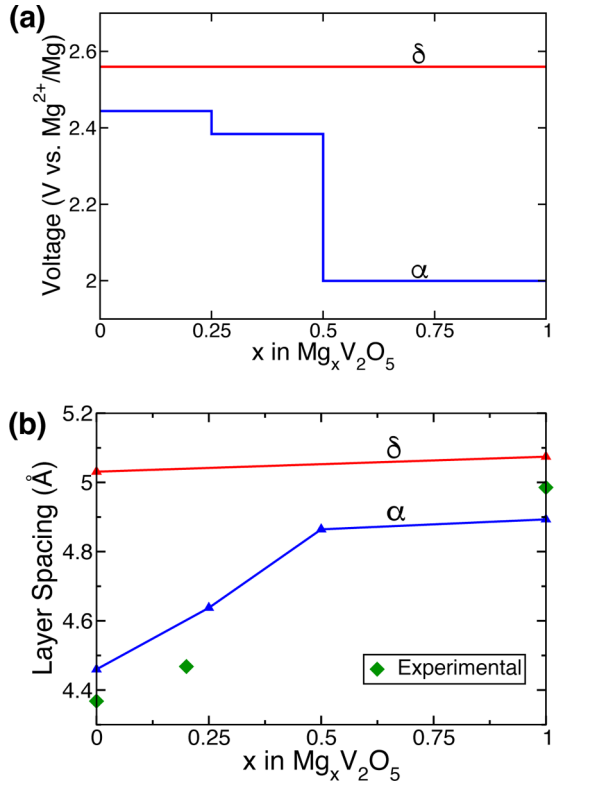

Figure 19. (a) Computed voltage curves for Mg-intercalation in α (blue) and δ (red) polymorphs of V_2O_5. The voltage drop at $x_{Mg} = 0.5$ in the α curve corresponds to the formation of the ϵ-phase. (b) Layer spacing as a function of Mg concentration in both α and δ, including van der Waals corrections, where there is good agreement with experimental data (green triangles).

In an effort to improve the room temperature Mg diffusivity in orthorhombic V_2O_5, Novák et al.[146,171,173] spearheaded attempts to use water as a cointercalating medium to shield the Mg^{2+} charge during its migration in the cathode lattice. Using an electrolyte consisting of magnesium perchlorate ($Mg(ClO_4)_2$) combined with water dissolved in acetonitrile (ACN), Novák et al. were able achieve a capacity higher than 170 mAh/g at room temperature[146] and attributed the improvement in electrochemical performance to optimization of the water content.[171] The authors further elaborated that the improvement in capacities achieved a maximum when the ratio of Mg^{2+} content in the electrolyte to the water content was ~1. Similar improvements in capacity were also observed by Yu et al.[174] when water was introduced in a $Mg(ClO_4)_2$-PC based electrolyte. Although Novák and co-workers claimed Mg^{2+} insertion based on atomic emission spectroscopy (AES)[146] and EDS[173] measurements, no quantitative data was made available. In addition, XRD measurements[173] indicating insignificant layer expansion on Mg-intercalation in V_2O_5 are seemingly in contradiction with first-principles estimations of ~9% increase up to $x_{Mg} \sim 0.5$ (see Figure 18).[169] Furthermore, experiments on hydrated polymorphs of V_2O_5, such as the xerogel (see section below), report significant layer spacing changes during water cointercalation in the structure,[175] potentially disputing the previously made arguments[146,171,173] that water cointercalation is responsible for improvements in capacity, since there is no indication of notable layer spacing variations.[146,173] Given the well-known incorporation of H atoms into the orthorhombic V_2O_5 structure in acidic media,[176]

DOI: 10.1021/acs.chemrev.6b00614
Chem. Rev. 2017, 117, 4287−4341

it is possible that a portion of the capacity observed in electrochemical experiments is a result of proton intercalation, as discussed at the beginning of section 5. Hence, detailed theoretical and experimental studies are required to understand and verify the role of water in cointercalating Mg, as briefly deliberated in the xerogel section below.

As was observed in α-MoO_3, reducing the particle size of V_2O_5 seems to mitigate poor Mg^{2+} diffusivity, as demonstrated in V_2O_5 nanopowders[162] (although no structural evidence of Mg^{2+} intercalation was provided) and thin films.[62] On the basis of visual observations of reversible electrode color changes, high-resolution-SEM imaging of charged and discharged samples, X-ray photoelectron spectroscopy (XPS) and XRD measurements, Gershinsky et al.[62] argued that reversible Mg intercalation occurs into V_2O_5. The authors reported a flat voltage curve at an average of ~2.35 V with a ~140 mAh/g capacity beyond which the voltage drops (Figure 18a), in agreement with first-principles calculations which predict a voltage drop at $x_{Mg} \sim 0.5$ due to the formation of a stable Mg-vacancy ordering, referred to as the ϵ-phase (see, Figure 19a).[169] Furthermore, Gershinsky et al.[62] reported an expansion of the interlayer distance due to the shift in the (010) peak during XRD measurements of the discharged samples alongside the formation of additional peaks at ~29.5° and 37.2° (Figure 18b), which are in accordance with theoretical calculations that indicate an increase in the interlayer distance upon the formation of the Mg-vacancy ordered ϵ-phase (Figure 19b).[169] Nevertheless, the presence of Cl^- and O^{2-} peaks in the XPS spectra of discharged samples,[62] combined with the known capacitor-like behavior of V_2O_5 structures with large surface area[144] indicate that a part of the measured capacities could arise from both electrolyte decomposition and the pseudo-Faradaic behavior of V_2O_5 thin films.

Recent first-principles calculations on Mg-V_2O_5 have reported several properties such as Mg insertion voltages, barriers for Mg (and MV) diffusion[169,170,177−179] and the temperature−composition phase diagram,[169] which can be benchmarked effectively with available experimental data. While Wang et al.[178] predicted similar barriers for Mg diffusion in single-layered and bulk orthorhombic V_2O_5, the authors in ref 179 benchmarked the lattice parameters (including the interlayer spacing) with and without van der Waals corrections in DFT calculations. From Carrasco's calculations,[179] it can be concluded that using a vdW-DF2 exchange-correlation functional to account for van der Waals interactions causes discrepancies in predicted voltages despite agreement with experimental structure parameters. Gautam et al.[169] calculated the Mg intercalation phase diagram in orthorhombic V_2O_5 and attributed the experimentally observed sluggish Mg kinetics within the host to high Mg migration barriers in α-V_2O_5. Further, the authors concluded that the experimentally observed drop in the voltage profile at $x_{Mg} \sim 0.5$ was due to the formation of the metastable ϵ-phase, resulting in a kinetic hindrance to the equilibrium $\alpha \rightarrow \delta$ transition. Additionally, they reported lower Mg migration barriers in δ(~600−760 meV) than in α(~975−1120 meV). An extension of the voltage and mobility calculations to other MV systems, such as Ca^{2+} and Zn^{2+}, indicates that the δ-polymorph could be a better host for MV-cations compared to α, owing to the superior mobilities predicted for Mg^{2+} and Ca^{2+} (~200 meV in δ compared to ~1700−1900 meV in α for Ca).[170] Earlier calculations by Zhou et al.[177] reported a higher Mg^{2+} migration barrier in δ compared to α, and a facile $\alpha \rightarrow \delta$ transition in Mg−V_2O_5, in contrast to the results of refs 169 and 170. However, Zhou et al.[177] predict higher open circuit voltages for Mg^{2+} insertion in V_2O_5 compared to Li^+, contradicting available experimental data.[62,162,167]

Parallel experiments on Ca-cycling in orthorhombic-V_2O_5 have reported qualitatively different results, such as ~400 mAh/g capacity at ~2.0 V by Hayashi et al.,[164] in comparison to the ~200 mAh/g at ~3.0 V reported by Amatucci and co-workers.[162] However, both experiments report poor Ca^{2+} mobility in V_2O_5, characterized by high overpotentials on Ca^{2+} discharge and low current densities. The sluggish kinetics are in agreement with theoretical predictions of a high Ca^{2+} migration barrier in the thermodynamically stable α-V_2O_5.[170]

Despite several experimental attempts to achieve Mg (MV)-intercalation in orthorhombic V_2O_5, there exist numerous open questions as to the practicality of V_2O_5 as a MV cathode material. While initial Mg-insertion attempts used a higher operating temperature to improve poor Mg migration within the structure, the reversibility of the intercalation process was quite limited.[172] The use of solvent cointercalation, especially water,[146,171,173] poses several challenges not only in characterizing the electrode to determine the actual impact of water on improving Mg mobility but also in verifying that proton intercalation is indeed not contributing to any of the capacity observed. Also, the presence of water in the electrolyte will create detrimental passivation at the Mg metal anode.[52] Co-intercalating aprotic nonpassivating solvents to improve Mg mobility is therefore a strategy that warrants a deeper exploration both theoretically and experimentally.

Further clarification is required to decouple capacitance effects from redox intercalation in experiments using nanoscale orthorhombic V_2O_5, which have indeed reported reliable reversible intercalation data.[62] Comparisons of available experimental results with DFT lattice parameters, insertion voltages, and phase stabilities, indicate that experimentally cycled V_2O_5 remains in the α polymorph.[169] However, at $x_{Mg} = 1.0$ the δ phase is thermodynamically stable and chemically synthesizable,[180] with first-principles mobility calculations indicating lower migration barriers than α (refer to discussion above).[170] Thus, theoretical predictions suggest a possible strategy to improve the rate-performance and accessible capacity of orthorhombic V_2O_5 by synthesizing the cathode in the discharged state and (de)intercalating Mg^{2+} in δ-V_2O_5. Given the evidence of reversible $V^{5+} \leftrightarrow V^{3+}$ redox plateaus,[181] the versatility of the structure in intercalating a variety of MV ions and the potentially high energy densities that the material can achieve as a cathode, orthorhombic V_2O_5 still holds promise for MV batteries.

Xerogel-V_2O_5. A principal problem in most oxide cathode materials for MV batteries, including orthorhombic V_2O_5, is the expected slow ionic diffusion within the structure (compared to Li^+) which in turn adversely impacts the electrochemical performance.[12] The poor mobility of MV ions has largely been attributed to the high positive charge density that causes severe local distortions in the cathode host, as discussed earlier in section 5. One strategy to mitigate the sluggish migration of MV ions is to provide "solvent" molecules in the cathode structure that "shield" the charge on the MV ion electrostatically and attenuate the structural distortions.[141] Solvent cointercalation is a known phenomenon in Li- and Na-ion batteries,[182−185] enabling otherwise thermodynamically prohibited intercalation reactions[186] and causing structural transformations (such as spinel → layered in MnO_2,[145] see MnO_2

DOI: 10.1021/acs.chemrev.6b00614
Chem. Rev. 2017, 117, 4287−4341

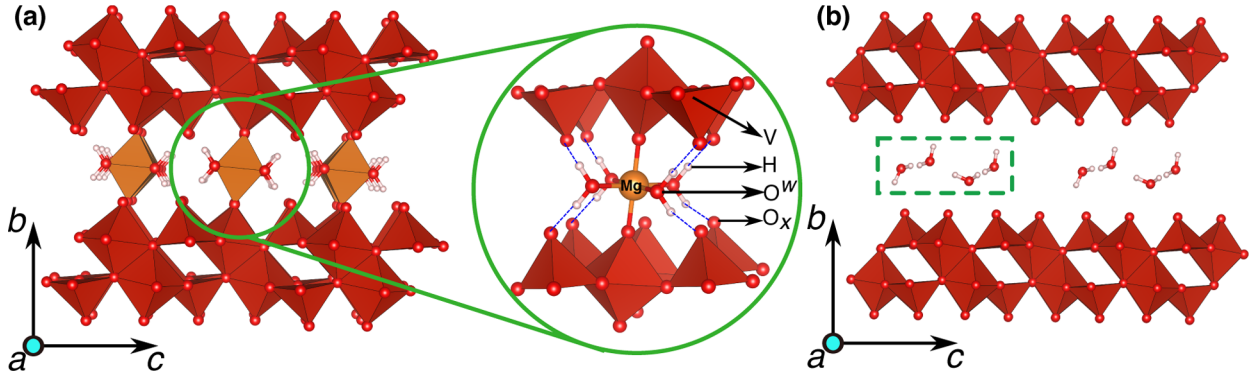

Figure 20. The structures of the fully magnesiated (x_{Mg} = 0.5) and the fully demagnesiated xerogel structures, with 1H_2O per formula unit of V_2O_5 are displayed in (a and b), respectively.[187] A closer view of the Mg coordination environment in the xerogel is displayed within the green circles of (a). (a and b) Reprinted from ref 187. Copyright 2016 American Chemical Society.

section below) that improve capacity.[147] Thus, layered structures which have a solvent intercalated already, such as xerogel-V_2O_5 and birnessite-MnO_2, provide a potential pathway to design cathodes with fast MV mobility.

The xerogel form of V_2O_5, with a chemical formula of $V_2O_5 \cdot nH_2O$ comprises a "bilayered" arrangement of V_2O_5 layers, as shown in Figure 20.[187,188] Being metastable, the xerogel loses structural H_2O on heating and eventually transforms irreversibly to orthorhombic V_2O_5 at ~350 °C,[175] while the structure has been reported to insert several MV cations, including Mg^{2+}, Ca^{2+}, Ni^{2+}, and Zn^{2+}.[189−199] A single bilayer of V_2O_5 in the xerogel is made up of two individual V_2O_5 monolayers (red polyhedra in Figure 20) bound by layer-bridging V−O bonds. Spacing between the bilayers (*b*-direction in Figure 20) is set by both the amount of intercalated H_2O[175] and the type (and quantity) of intercalant ions present in the structure.[195] While each mole of H_2O added (removed) to (from) the structure results in an increase (decrease) of the interbilayer spacing by ~2.8 Å,[175] the spacing was found to increase further upon Na^+ intercalation, but decrease with Mg^{2+} insertion.[195] Though the positions of the H_2O molecules in the interbilayer space are known, the positions of intercalant ions are not well-resolved from experiments, with some structural models proposed in refs 189, 200, and 190.

MV intercalation into the xerogel structure has been attempted with organic[193,195,198,200−202] and aqueous electrolytes.[192,196] Imamura et al.,[200,201] were one of the first to report electrochemical Mg cycling in xerogel-V_2O_5, as shown in Figure 21a, using a three electrode setup comprising a Mg ribbon counter, $Ag/AgNO_3$ reference, and $Mg(ClO_4)_2$ dissolved in ACN as the electrolyte. While the authors claimed a first discharge capacity of ~540 mAh/g, corresponding to inserting ~1.84 mol of Mg into the structure, the capacity faded rapidly in the next few cycles and eventually converged to ~300 mAh/g. At a voltage of ~2.8 V vs Mg, a capacity of approximatively 300 mAh/g corresponds to energy densities of ~840 Wh/kg and ~2303 Wh/l. The authors also reported nearly 80% capacity retention at the 35th cycle (compared to the capacity achieved at the 10th cycle) during charge−discharge tests. XRD measurements by Imamura et al. display slight peak shifts, indicating decreasing interbilayer distance with Mg^{2+} intercalation, consistent with other experimental[195] and theoretical[187] studies, although the peak intensities reduce drastically with magnesiation. Fourier Transform Infrared Spectroscopy (FTIR) measurements by the authors indicate ClO_4^- peaks, which the authors attribute to cointercalation of

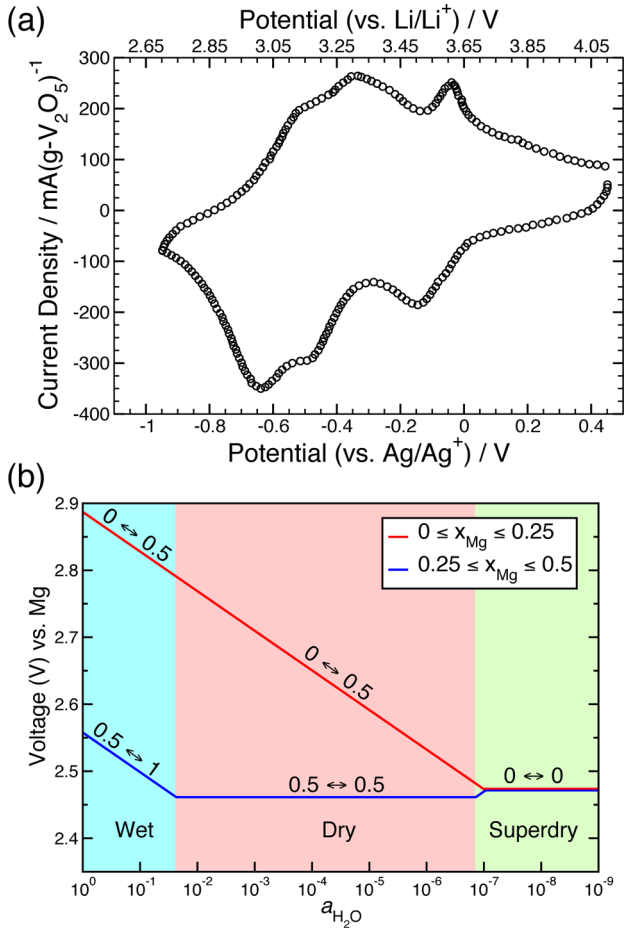

Figure 21. (a) Cyclic voltammogram upon Mg cycling in xerogel-V_2O_5 as reported by Imamura et al.[200] and (b) voltage curves from first-principles calculations for Mg insertion in the xerogel, plotted as a function of water activity in the electrolyte.[187] The text annotations on the voltage plateaus in (b) reflect the changes in the water content within the xerogel for the corresponding change in Mg content. (a) Reprinted and digitized with permission from ref 200. Copyright 2003 Elsevier. (b) Reprinted from ref 187. Copyright 2016 American Chemical Society.

the ClO_4^- ions into the structure. From the FTIR and XRD data, the role of ClO_4^- during Mg intercalation remains unclear. Furthermore, the peak splitting of the V−O−V and the V═O bonds, observed in the FTIR spectrum as new peaks at lower

DOI: 10.1021/acs.chemrev.6b00614
Chem. Rev. 2017, 117, 4287−4341

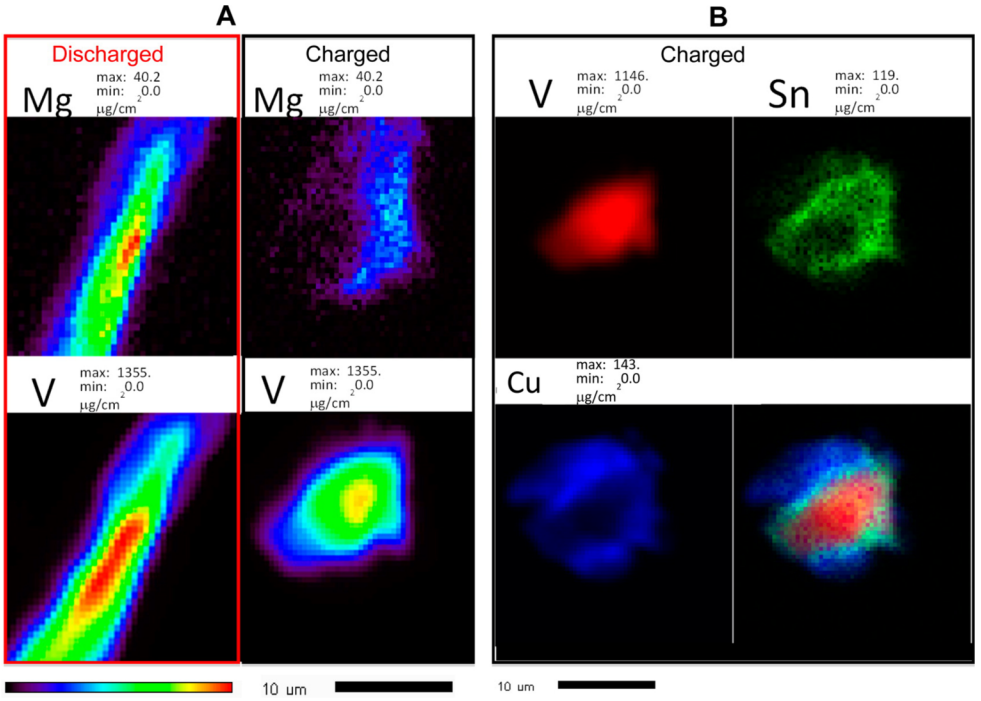

Figure 22. (a) XRF maps of (left) Mg and V in a discharged sample and (right) charged samples obtained with soft (top) and hard (bottom) energy X-rays.[195] (b) XRF images of elemental distribution of V (top left), Sn (top right), and Cu (bottom left) and their overlay (bottom right) obtained using hard X-rays. (a and b) Reprinted and adapted from ref 195. Copyright 2015 American Chemical Society.

wavenumbers, could arise from proton intercalation into xerogel-V_2O_5 instead of the expected Mg^{2+} insertion.

Subsequent Mg intercalation experiments using organic electrolytes into the xerogel report qualitatively different results.[195,198] For example, Tepavcevic et al.[195] cycled Mg in a voltage window of ~0−2.2 V vs Mg yielding a capacity of ~80−120 mAh/g over 50 cycles, while Sa et al.[198] reported a higher average voltage (~1.9 V vs Mg) and a lower capacity (~50 mAh/g) over 10 cycles. Both experiments[195,198] report lower Mg intercalation voltages and capacities in comparison to the cyclic voltammetry of Imamura et al.,[200,201] conducted in the range of ~1.9−3.4 V vs Mg, yielding ~300 mAh/g. Using a full cell setup made of a nanocrystalline Sn anode, $Mg(ClO_4)_2$ dissolved in ACN electrolyte and a Mg-discharged xerogel cathode, Tepavcevic and co-workers[195] claimed reversible Mg intercalation based on a multitude of X-ray fluorescence (XRF), XANES, high-angle annular dark-field imaging (HAADF), small-angle X-ray scattering (SAXS), wide-angle X-ray scattering (WAXS), and energy-dispersive analysis of X-rays (EDAX) measurements. The authors initially discharged a pristine xerogel galvanostatically against a Mg metal anode, with intercalation verified by the presence of Mg^{2+} in bulk XRF maps and changes in the V-oxidation evidenced by XANES measurements and then cycled the discharged xerogel against a Sn anode with Cu impurities. On cycling, the observed capacity attenuated from an initial value of ~160 to ~80 mAh/g by the 20th cycle before recovering to ~120 mAh/g at the 50th cycle, which the authors attributed to the nanocrystalline nature of both the anode and cathode used. However, XRF measurements on the cycled xerogel indicate the presence of Sn and Cu after cycling (Figure 22), suggesting possible contributions to observed capacities by the anode constituents in addition to Mg^{2+}, which might explain the capacity recovery with prolonged cycling. Also, EDAX measurements[195] indicating an increased presence of C and O peaks in the discharged samples (in comparison to the charged), probably indicate the occurrence of electrolyte decomposition, despite insignificant changes to the Cl^- peak.

Sa et al.[198] performed galvanostatic cycling of coin cells comprising a Mg metal anode, $Mg(TFSI)_2$ dissolved in diglyme electrolyte, and a pristine xerogel-V_2O_5 as the cathode. On the basis of XANES, XRD, and NMR results (Figure 23), the authors concluded reversible Mg^{2+} intercalation into the xerogel, with slight capacity enhancement over multiple cycles despite observations of a surface film formation at the Mg/diglyme interface. Further, the authors reported the existence of three distinct phases, based on observations of three distinct interbilayer spacing values on discharge [obtained through pair distribution function (PDF) analysis of the XRD data], which qualitatively agree with first-principles predictions of changes in the interbilayer spacing with Mg content and the formation of stable Mg-ordered configurations at intermediate Mg concen-

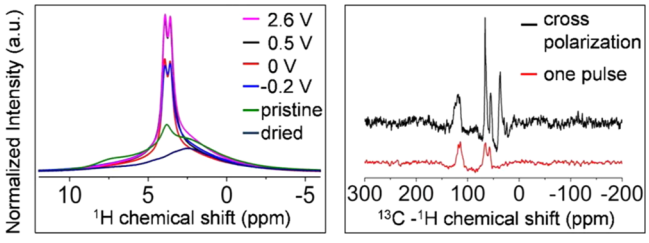

Figure 23. ^1H NMR for $V_2O_5{\cdot}nH_2O$ at various charged/discharged states (2.6 V to −0.2 V) (left panel) from ref 198. The right panel displays ^{13}C NMR spectra of discharged sample (0 V). The data in red represents one pulse experiment, and data in black represents $^1H-^{13}C$ cross-polarization experiment, which indicates the presence of TFSI carbons. Reprinted and adapted from ref 198. Copyright 2016 American Chemical Society.

DOI: 10.1021/acs.chemrev.6b00614
Chem. Rev. 2017, 117, 4287−4341

trations.[187] Interestingly, ^{25}Mg, ^{13}C, and ^{1}H NMR studies (Figure 23) by the authors revealed not only an increase in proton double peak intensities, probably from diglyme decomposition, upon discharge but also a lack of MgO formation within the xerogel, leading the authors to claim cointercalation of a Mg-diglyme complex alongside the displacement of the lattice water. However, the authors report the appearance of aliphatic chains, based on $^{1}H-^{13}C$ cross-polarization NMR spectra, resulting from diglyme decomposition in the cathode host, which would affect the electrochemical data presented. Also, the observed capacity increase with cycling could be a result of electrolytic decomposition at the anode or cathode, despite the authors attributing the increase to improved electrolyte percolation into the cathode.

Lee et al.[193] performed cyclic voltammetry of a hydrated V_2O_5 electrode using a Ag/Ag^+ reference and a Pt counter electrode and various electrolytes. The cathode material, $Mg_{0.1}V_2O_5{\cdot}1.8H_2O$ xerogel, was prepared by dissolving crystalline MgV_2O_6 in water followed by treatment with an ion-exchange resin, with Yin et al.[202] reporting a similar synthesis route. Lee and co-workers[193] determined the cathode composition by a combination of thermogravimetric analysis (TGA) and ICP-optical emission spectroscopy (OES) measurements. The electrolytes used include $Mg(ClO_4)_2$ and $Mg(TFSI)_2$, dissolved in ACN and ethylene carbonate:dimethyl carbonate (EC:DMC) solvents, with $Mg(ClO_4)_2$ in ACN displaying the best electrochemical performance among those considered. The authors[193] also claimed an initial Mg discharge capacity of ~300 mAh/g, based on galvanostatic charge−discharge tests with $Mg(ClO4)_2$ in ACN, with an immediate capacity fade to ~230 mAh/g in the second cycle and subsequent capacity recovery to ~280 mAh/g by cycle 7, qualitatively similar to previous cycling tests by Imamura et al.[200,201] The solitary anodic (~0.0 V vs Ag/Ag^+) and cathodic (~0.5 V) peaks reported by the authors during cyclic voltammetry with $Mg(ClO_4)_2$ in ACN disagree both qualitatively and quantitatively with previously reported experimental data,[200] which is not addressed by the authors. Also, XRD measurements by the authors[193] indicating a lack of change in the interbilayer spacing with Mg cycling is in contrast with significant layer contraction (expansion) on Mg insertion (removal) reported by other experiments[195,198] and theoretical predictions.[187] Similar to a few other works,[53,192,196,197,203,204] the claim of Mg intercalation in hydrated V_2O_5 is based mainly on electrochemical data and without sufficient characterization of discharged (charged) samples to ascertain Mg presence (absence) is symptomatic of the challenges involved in understanding Mg intercalation in oxide hosts in general.

Mg cycling in xerogel-V_2O_5 using aqueous electrolytes was reported by Mentus and co-workers,[192,196] employing a Pt counter electrode, a Calomel reference electrode, and a $Mg(NO_3)_2$ electrolyte, achieving nominally higher voltage compared to organic electrolytes.[195,198,200] While Stojković et al.[192] reported reversible electrochemical Mg intercalation in the xerogel based on an observed capacity of ~107 mAh/g in cyclic voltammetry experiments, no characterization evidence for Mg insertion was provided. Using a similar setup, Vujković et al.[196] compared the electrochemical performance of Li^+, Mg^{2+}, K^+, and Na^+ intercalation in the xerogel employing aqueous electrolytes and claimed reversible Mg^{2+} intercalation based on cyclic voltammetry and chronopotentiometry measurements. However, apart from visual observations of color changes of the xerogel electrode upon charge (and discharge), similar to those reported for Mg intercalation in orthorhombic V_2O_5,[62] Mg intercalation was not supported with robust characterization experiments. Hence, it remains unclear as to whether reversible Mg intercalation can indeed occur into the xerogel using aqueous electrolytes.

The lack of structural knowledge of Mg- and H-positions in the xerogel, limited by the difficulties in characterization due to the nanocrystalline nature of the material, has constrained the theoretical studies on Mg intercalation in the xerogel. Recently, Gautam et al.[187] used a 3-step computational strategy to resolve the Mg-intercalated xerogel structure (Figure 20), with a maximum of $x_{Mg} = 0.5$ and $n_{H_2O} = 1$ per V_2O_5, and subsequently employed a thermodynamic framework based on grand-potential phase diagrams to study $Mg-H_2O$ cointercalation (Figure 21b). These authors find that while water shuttling along with the Mg^{2+} is thermodynamically favored when wet electrolytes are used (with activity of water $a_{H_2O} \sim 1$), water cointercalation does not occur at higher x_{Mg} in dry electrolytes ($a_{H_2O} \sim 10^{-4}$). A superdry electrolyte that has minimal traces of water ($a_{H_2O} \sim 10^{-8}$) not only causes all the water in the xerogel structure to exit the electrode but also effects a slight change in the phase behavior of the Mg-xerogel system in comparison to wet and dry electrolytes.[187] In regimes where water cointercalates with Mg^{2+}, first-principles calculations indicate an increase in Mg insertion voltage with increasing a_{H_2O} (see Figure 21b), which supports well the experimental observations.[192,195,196,198,200] The dependence of voltage on both the activity of water in the electrolyte as well as the extent of magnesiation leads to important consequences in the future design of electrode−electrolyte pairs that could calibrate the voltage based on a cointercalating species. Although further studies are required to fully understand Mg-intercalation in the xerogel system, theoretical studies may be particularly useful for solvent cointercalating systems, also pertinent for known Li and Na-ion electrode materials,[145,182,183,186] due to the experimental difficulties in refining the structure.

Recently, researchers at Argonne National Laboratory[199] and University of Waterloo[205] independently reported reversible Zn intercalation in *xerogel*-V_2O_5, consistent with the prediction of high Zn mobility in layered oxides and orthorhombic V_2O_5.[170] Using $Zn(TFSI)_2$ in ACN as the electrolyte, Zn nanofilaments as counter electrode and electrochemically deposited xerogel as the working electrode, the authors observed a reversible capacity of ~170 mAh/g for 120 cycles at 0.7 V vs Zn and C/10 rate. Capacity retention at rates as high as 20C was remarkable (~120 mAh/g), providing substantial experimental evidence that the mobility of Zn^{2+} can be very high when matched with the correct host structure.[142,170] Further, Senguttuvan et al.[199] claimed Zn intercalation based on EDS and XANES measurements, albeit without quantitative structural characterization. Also interesting to note is the shift in the reduction and oxidation voltammetry peaks with Zn cycling, which the authors attributed to a decrease in Zn deposition overpotential and structural rearrangements within the cathode. ACN cointercalation was ruled out based on Raman spectroscopy measurements.[199] Although Zn^{2+} is expected to have high mobilities within orthorhombic-V_2O_5,[170] the high capacities observed can be partly caused by pseudocapacitive behavior, especially at high rates such as 20C.

DOI: 10.1021/acs.chemrev.6b00614
Chem. Rev. 2017, 117, 4287−4341

Nevertheless, the results from ref 199, specifically the development of nonaqueous electrolytes with high anodic stability and the high rate capability of a divalent intercalant, can lead to significant improvements in the development of secondary nonaqueous Zn batteries that are capable of delivering power comparable to Li-ion batteries.

The phenomenon of Mg-water cointercalation leading to better mobilities and higher voltages in the xerogel system presents an important opportunity to utilize solvent cointercalation in designing both the cathode and the electrolyte to achieve energy densities potentially higher than current Li-ion systems. While reversible Zn intercalation in the xerogel seems possible,[199] Mg cycling experiments done with organic electrolytes so far report varied electrochemical data,[193,195,198,200,201] including a wide range of capacities (from ~300 mAh/g[200] to ~50 mAh/g[198]), making it difficult to unravel the mechanism of Mg intercalation in the xerogel structure. Both Lee et al.[193] and Imamura et al.[200] claimed reversible Mg insertion based largely on electrochemical data. The reports by Tepavcevic et al.[195] and Sa et al.[198] documented capacity recovery with Mg cycling, albeit at quantitatively different values of observed capacities, while both experiments may have been affected by other side reactions, such as anodic element cycling (namely, Sn and Cu)[195] and electrolyte (diglyme) decomposition,[198] respectively. Mg cycling in aqueous electrolytes was claimed by Mentus and co-workers,[192,196] without any significant characterization evidence for Mg intercalation (removal) upon discharge (charge). Theoretical studies in Mg-xerogel have been limited, with Gautam et al.[187] calculating the grand-potential phase diagram of the system and observing regimes where Mg-water cointercalation is thermodynamically favored. Nonetheless, it remains unclear whether Mg (Zn) can be reversibly intercalated for a prolonged number of cycles in the xerogel, despite multiple experimental attempts, highlighting the need to decouple side reactions such as proton intercalation, electrolyte decomposition, and pseudo-Faradaic reactions that could significantly affect the electrochemical data observed. Finally, it should be noted that more detailed characterization of the xerogel starting material may be needed as the synthesis of xerogel is more difficult to precisely control than classic solid state reactions. As a result, materials that are reported as xerogels may in fact be substantially different.

5.3. MnO_2 Polymorphs

Multivalent intercalation into MnO_2-compounds is attractive because of their high theoretical voltage (~2.8 V[149]) and capacities (~308 mAh/g for inserting ~0.5 mol or 1 equivalent of Mg, respectively), leading to desirable energy densities of ~862 Wh/kg and ~3630 Wh/l. As with other oxides, ionic diffusion is expected to be impeded by the combination of the highly ionic nature of the oxide host lattice and the large charge density of the MV ion. Electrochemical Li intercalation in MnO_2 was initially investigated as early as 1974,[206−209] while chemical insertion of Mg into a variety of MnO_2 phases was explored by Bruce et al.[118] Motivated by the abundant availability, environmental compatibility, low cost, the aforementioned large theoretical capacity, and structural versatility of a number of known MnO_2 polymorphs, electrochemical intercalation of Mg[147,158,210−227] and Zn[204,228−235] in MnO_2 has received much attention recently. Researchers have suggested that the presence of large structural voids characteristic of some MnO_2 polymorphs, such as Hollandite (α-MnO_2), OMS-5 (a 4 × 2 tunnel structure under the Ramsdellite family), and the layered Birnessite (δ-MnO_2), as seen in Figure 24,

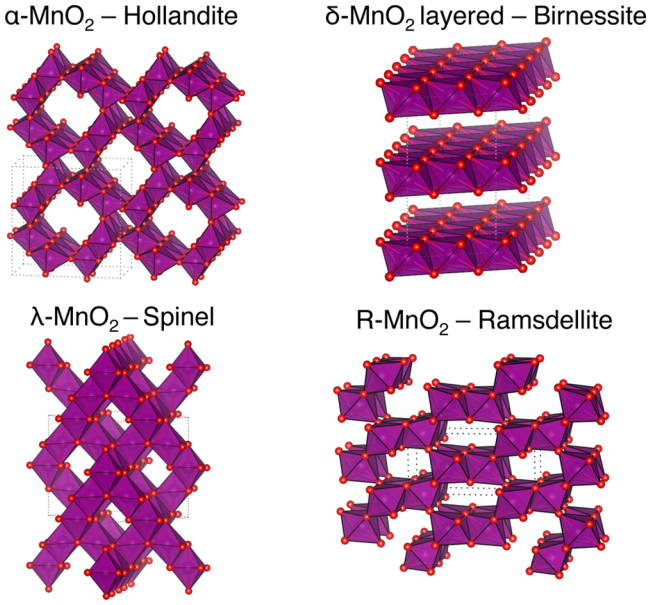

Figure 24. MnO_2 polymorphs investigated as intercalation cathode materials for Mg-ion batteries. MnO_6 octahedra in violet share oxygen (in red) corners and edges in Hollandite α-MnO_2 and Ramsdellite R-MnO_2 and only edges in Spinel λ-MnO_2 and Birnessite δ-MnO_2.

could facilitate the diffusion of Mg^{2+} (MV) ions.[158,218,221,225] However, there is potential for conversion reactions that lead to the irreversible formation of MgO.[158,221] The presence of water in the cathode or electrolyte is reported to significantly affect the electrochemical performance of the MnO_2 system, with experiments claiming notable improvement in Mg-cycling in the layered-δ and the spinel-λ polymorphs[147,227,236] and a possible impact of water on the phase stability of the MnO_2 polymorphs upon Mg insertion.[145,227] Nevertheless, the presence of water can lead to parasitic side reactions, such as Mn^{2+} dissolution[237−239] or proton intercalation (as discussed in previous sections), which can contribute to the electrochemical data observed. Furthermore, reports of high initial Mg discharge capacities (corresponding to x_{Mg} > 0.5 per MnO_2[204,215,216]) may be observing the capacity resulting from electrolyte decomposition, given the low anodic stability (~3.5 V[32]) of most state-of-the-art Mg electrolytes. Such reports underscore the need for careful interpretation of experimental data.

In the following sections, we provide a critical analysis of the present literature on reversible MV intercalation in various MnO_2 polymorphs. Examination of the experimental data presented in Table 1 demonstrates the disparity in the reported voltage, capacity, cycle life, and electrochemical setups employed (i.e., working and counter-electrodes, electrolyte, current collectors, and other battery components), highlighting the need for careful analysis and interpretation of experimental results as well as the standardization of electrochemical measurement protocols for MV batteries.

α-MnO_2 and tunnels structures. Reversible Mg intercalation seems problematic in the α-phase and OMS-5 tunnel polymorphs,[217] given the significant capacity losses (~50% of first discharge) reported.[215,217] Recent investigations have attributed the capacity loss to possible conversion reactions

DOI: 10.1021/acs.chemrev.6b00614
Chem. Rev. 2017, 117, 4287−4341

Table 1. First Discharge Capacity (dis., in mAh/g) and Voltages vs Mg^{2+}/Mg (in V) of a Variety of MnO_2 Polymorphs, Using Various Electrolyte-Solvent Combinations, Reference and Anode Electrodes, Respectively[a]

1st dis.	voltage	electrolyte/counter electrode/anode	fade
		α-MnO_2-Hollandite	
310[215]	2.17	$Mg(ClO_4)_2$:ACN//Ag/$AgNO_3$/Mg	yes
210[216]	~2.00	$Mg(ClO_4)_2$:ACN//Ag/$AgNO_3$/Mg	yes
282[218]	2.80	Mg-HDMS:THF//Mg	yes
330[219]	2.17	$Mg(ClO_4)_2$:ACN//Ag/$AgNO_3$/Pt	yes
		OMS-5-Tunnel	
80[217]	2.17	$Mg(ClO_4)_2$:ACN//Ag/$AgNO_3$/Mg	yes
		δ-MnO_2-Birnessite	
75[215]	2.17	$Mg(ClO_4)_2$:ACN//Ag/$AgNO_3$/Mg	yes
231[147]	2.80	$Mg(ClO_4)_2$:ACN:H_2O//Ag/AgCl/Mg	—
231[147]	2.80	$Mg(ClO_4)_2$:H_2O//Ag/AgCl/Mg-*B*	yes
170[220]	2.27	$Mg(ClO_4)_2$:PC:H_2O//Ag/AgCl/Pt	no
150[227]	~3.00	$Mg(ClO_4)_2$:H_2O//Ag/AgCl/Pt	yes
130[227]	1.55	$Mg(TFSI)_2$:diglyme//Ag/AgCl/Mg	yes
		λ-MnO_2-Spinel	
209[219]	2.17	$Mg(ClO_4)$:ACN//Ag/$AgNO_3$/Pt	yes
35[203]	~2.84	$Mg(NO_3)_2$:H_2O//SCE/Pt	yes
545[204]	~2.84	$MgCl_2$:H_2O//SCE/C(graphite)	yes
190[236]	2.90	$Mg(NO_3)_2$:H_2O//SCE/Pt	—
150[224]	2.22	$Mg(NO_3)_2$:H_2O//Ag/AgCl/Pt	yes
120[224]	~2.60	$Mg(ClO_4)_2$:EC:DEC//Ag/AgCl/Pt	no
250[226]	—	$Mg(TFSI)_2$:PC//C(BP2000)	yes

[a]Occurrence of capacity fade over electrochemical cycling (Fade) is also indicated.[147]

leading to MgO formation[158,221,225] and Mn^{2+} dissolution in the electrolyte with subsequent deposition at the anode.[158,215,217]

In order to explain the observed capacity fade in α-MnO_2, Rasul et al.[215,217] initially suggested that Mg-ions could be "trapped" in the host lattice due to the high electrostatic interactions between the Mg and O atoms. However, computational studies based on first-principles calculations[142,240] have demonstrated that Mg (MV) diffusivity mainly depends on the changes in the MV coordination environment during diffusion, suggesting that more rigorous investigations are needed to unearth the origins of the oft-invoked but vaguely described "Mg trapping" phenomenon.[215,217] If Mg possesses sufficient bulk diffusivity for intercalation then barring the occurrence of substantial bulk structural or surface changes postintercalation, the ion should also be able to diffuse out. Furthermore, EDS, EELES, extended X-ray absorption fine structure (EXAFS), scanning transmission electron microscopy (STEM), X-ray absorption spectroscopy (XAS) and XPS measurements, in recent investigations,[158,218] revealed the formation of MnO at the surface of α-MnO_2 on magnesiation, indicating that irreversible conversion reactions may affect Mg intercalation in MnO_2 tunnels. This observation is consistent with the narrow voltage window within which intercalation into MnO_2 is preferred over conversion (Figure 14). Hence, the "trapped Mg" is most likely Mg that has reacted to form MgO or is locked up in particles that underwent surface passivation by MgO.

Benchmarking experimental observations with first-principles calculations, Arthur and collaborators[158,221,225] corroborated that α-MnO_2 converts to MnO, Mn_2O_3 and MgO after magnesiation and suggested that similar reactions could affect other oxide cathodes on Mg intercalation (as discussed earlier in section 5). TEM and EDS analysis of the MnO_2 nanoparticles revealed the presence of highly ionic and electrically insulating amorphous constituents (attributed to formation of MnO, Mn_2O_3, and MgO). As such, the authors[158,221] proposed that conversion reactions could be occurring only at the MnO_2 surface, where the Mn^{4+} are reduced, with the core part remaining crystalline. A meticulous series of electrochemical, surface area, ICP, and XRD measurements on MnO_2 tunnel polymorphs[221] with various morphologies (Figure 25, panels a and b) revealed that varying

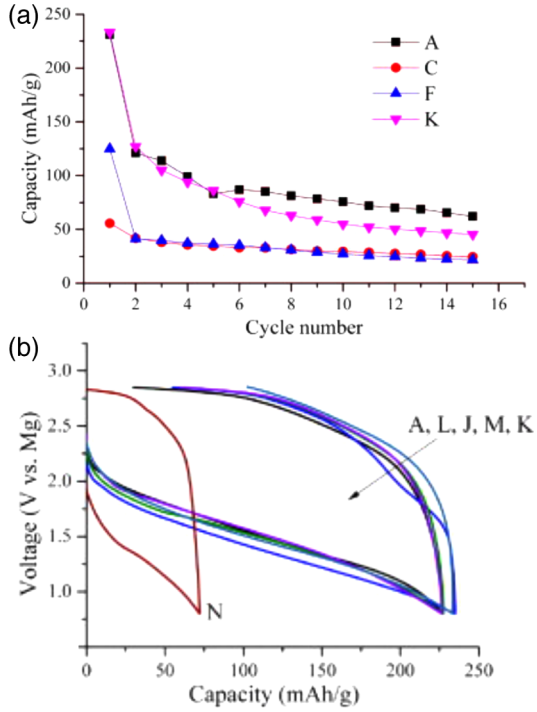

Figure 25. (a) Capacity fade for various samples of α-MnO_2. (b) First discharge−charge cycle of different MnO_2 polymorphs.[221] Letters in (a and b) refer to **A**, 10 × 20 nm^2 commercial α-MnO_2 nanorod; **C**, 60 × 100 nm^2 K^+ stabilized MnO_2 nanorod; **F**, 60 × 100 nm^2 H_2O stabilized α-MnO_2 nanorod; **J**, δ-MnO_2 with particle size >1 μm; **K**, ramsdellite with particle size >1 μm calcinated at 200 °C; **L**, ramsdellite with particle size >1 μm calcinated at 300 °C; **M**, β-MnO_2; and **N**, calcination at 500 °C of sample **J**, respectively.[221] (a and b) Reprinted and adapted with permission from ref 221. Copyright 2015 Elsevier.

the tunnel size (from 2 × 2 in α-MnO_2 to 1 × 1 in β and n × 2 in Ramsdellite) does not affect the initial Mg-discharge capacities (Figure 25b), giving credence to the fact that this is not Mg-bulk diffusivity which limits capacity. It is more likely that oxide conversion reactions are always favored in these polymorphs.

In addition to the aforementioned capacity fade and conversion reactions that afflict the MnO_2 polymorphs, some experiments also report Mn-leaching from α-MnO_2 (the surfaces) into the electrolyte followed by deposition at the Mg anode,[158,215,217] hence contributing to the observed electrochemical capacity and degradation of the cathode material. Given the challenges in ensuring reversible Mg intercalation, it remains to be seen if MnO_2 tunnel structures will ever be practical Mg cathode materials.

DOI: 10.1021/acs.chemrev.6b00614
Chem. Rev. 2017, 117, 4287−4341

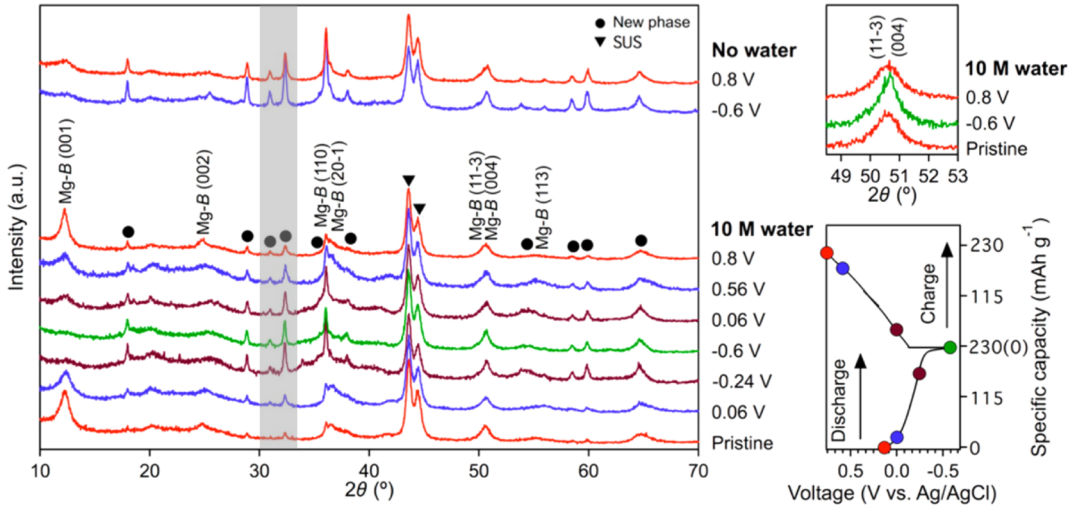

Figure 26. Ex situ XRD of δ-MnO_2 in $Mg(ClO_4)_2$/ACN:H_2O (10 M of water) at various states of charge and discharge from ref 147. Reprinted and adapted from ref 147. Copyright 2015 American Chemical Society.

With a theoretical gravimetric capacity of 308.3 mAh/g for inserting 0.5 mol of Zn per MnO_2, Hollandite and Ramsdellite have been also explored as cathode materials for Zn-ion batteries. Xu et al.[228] showed Zn intercalation in α-MnO_2 from aqueous electrolytes [$ZnSO_4$ and $Zn(NO_3)_2$] against a Zn metal anode followed by characterization of the discharged material with XRD and XPS. While the initial capacity was ~120 mAh/g (with an open circuit voltage of ~1.50 V), subsequent cycles showed a constant capacity of ~100 mAh/g (at 6C, for 100 cycles). Although the XPS results suggested Zn insertion in Hollandite, given the Zn/Mn ratio of ~0.52 measured in the discharged samples, the authors do not discuss the possible occurrence of parallel conversion reactions, which have been reported in ref 235. Because XPS only probes the surface of the cathode particles, these results cannot ensure Zn intercalation. Subsequently, Xu et al.[230] used impedance spectroscopy to investigate Zn insertion in α-MnO_2, reporting Zn ionic diffusivity ranging from 0.84 to 2.58 × 10^{-16} cm^2/s at different states of charge. Although the authors claimed that α-MnO_2 undergoes a phase transformation upon Zn insertion on the basis of impedance measurements, no structural evidence for any Zn intercalation or phase transformation was provided.[230]

More recently, Lee and co-workers[231,232,241] also reported Zn intercalation in Hollandite supported by cyclic voltammetry, ex situ XRD, TEM, and XANES characterization of coin cells comprised of a Zn metal anode, 1.0 M $ZnSO_4$ aqueous electrolyte, and a nanorod of α-MnO_2. The initial discharge capacity (at rate of C/20) of ~194 mAh/g faded to ~150 mAh/g within the first 30 cycles. A plateau at ~1.3 V was observed and has been related to the presence of two distinct phases also detected in the XRD patterns. On the basis of similar XRD patterns between the as-synthesized $Zn_\alpha Mn_2O_4$ and Na-Birnessite ($Na_4Mn_{14}O_{27}\cdot 9H_2O$), the authors claimed a discharged phase of Zn-Birnessite (also known as Zn-chalcophanite)[232,241] and speculated that α-MnO_2 can reversibly transform into Zn-Birnessite upon Zn intercalation. The analysis of the Mn-*K*-edge data showed an increase of the Mn oxidation state during Zn discharge, which is inconsistent with Zn intercalation.[232] Also the atomic absorption measurements of the electrolyte composition at various states of discharge indicated that 1/3 of the Mn from the α-MnO_2 is dissolved in the electrolyte. Though the authors attributed this phenomenon to Mn^{3+} disproportionation into Mn^{4+} and Mn^{2+} and dissolution of the latter in water, others linked similar observations for Mg intercalation in α-MnO_2 to conversion reactions rather than intercalation.[158,221] Similarly, investigations of Zn-intercalation in γ-MnO_2 (a phase originating from the intergrowth of β-MnO_2 and Ramsdellite, Figure 24) by Alfaruqi et al.[233] reported significant Mn presence in the electrolyte upon discharge, which can contribute to the electrochemical response observed. However, based on in situ Synchrotron XRD studies, the authors[233] reported the coexistence of several MnO_2 polymorphs, including γ, layered (Birnessite-like), and spinel, on Zn-discharge and claimed a reversible transformation to γ-MnO_2 on complete charging. Nevertheless, it remains to be seen whether the significant phase transformations (tunnel structures → close-packed spinel) that occur electrochemically in the Zn-MnO_2 system are highly reversible.

***δ*-MnO_2.** Mg-intercalation in Birnessite, or δ-MnO_2, a hydrated layered polymorph, was attempted by Nam, Aurbach, and co-workers[147] and by Sun, Nazar, and collaborators,[227] with significantly better Mg cycling in aqueous electrolytes compared to nonaqueous. As in the case of xerogel-V_2O_5, the presence of H_2O in the structure (and/or the electrolyte) could improve poor Mg intercalation kinetics in MnO_2[146,147,215−217,227] by shielding the divalent Mg-charge and reducing the Mg desolvation energy during (de)-intercalation by the water molecules, though such an effect has not unambiguously been proven.

Nam et al.[147] investigated Mg intercalation in δ-MnO_2, synthesized through aqueous electrochemical transformation of spinel-Mn_3O_4, under two distinct water containing electrolytes: (i) in a mixture of $Mg(ClO_4)_2$/ACN:H_2O and (ii) in aqueous electrolytes. Reversible Mg intercalation was claimed by the authors based on a reversible change in Mn oxidation state (i.e., Mn^{4+}/Mn^{3+}), deciphered from XPS and XANES measurements. Additional characterization, such as XRD (Figure 26) and annular bright field scanning electron transmission microscopy (ABF-STEM) were used to resolve the magnesiated Birnessite structure, including the positions of the Mg atoms and water molecules. Nam et al.[147] reported a continuous increase in capacity for increasing water content

DOI: 10.1021/acs.chemrev.6b00614
Chem. Rev. 2017, 117, 4287−4341

from 56.8 mAh/g in ACN up to ~227.6 mAh/g (at ~2.8 V) in bulk water. Similar observations have been reported for Mg intercalation in α-MoO_3[151] and orthorhombic-V_2O_5.[146,171] Furthermore, the authors claimed highly reversible Mg intercalation (over 10000 cycles at >50% initial capacity), yielding slightly higher capacities (~231 mAh/g) at higher current densities (up to ~2000 mA/g) in aqueous electrolytes. Nevertheless, it cannot be excluded that higher capacities and apparently enhanced Mg cycling capability resulting from increasing water content are a result of proton intercalation, as discussed earlier.

In analogy to ref 147, Mg intercalation in layered-MnO_2, synthesized as $Mg_{0.15}MnO_2{\cdot}0.9H_2O$, was investigated by Sun et al.[227] using a Ag/AgCl reference in a 0.5 M $Mg(ClO_4)_2/H_2O$ electrolyte with a Pt counter electrode. The authors employed XRD, SEM, XPS, high-resolution transmission electron microscopy (HRTEM) and electron energy loss spectroscopy (EELS) to verify Mg intercalation in δ-MnO_2 under aqueous conditions. An initial discharge capacity of ~150 mAh/g (corresponding to x_{Mg} ~ 0.3 per MnO_2) was observed. Subsequent Mg cycling lead to significant capacity fade within 20 cycles, in contrast to what is reported in ref 147. On the basis of observations of Mn accumulation at the anode separator via SEM, the authors attributed the capacity fade to Mn^{2+} dissolution.

More importantly, refs 147 and 227 both observed a large decrease in interlayer distance on Mg intercalation in δ-MnO_2 but proposed slightly different phase transformations. For example, Nam et al. using ICP, ABF-STEM, and TGA speculated that Mg and water cointercalate leading to cation mixing and structural rearrangement on discharge, whereas Sun et al.[227] associated the substantial shrinking of the layer spacing observed to water expulsion during Mg discharge.

Furthermore, the discharged XRD peaks in δ-MnO_2 and λ-$MgMn_2O_4$ spinel (Figure 27b) showed significant similarity with some changes in the stacking scheme, especially indicated by the (103) XRD reflection at ~33° in Figure 27b.[227] Notably, a similar peak was left unidentified by Nam et al.[147] (refer to the gray shade between 30 and 35° in Figure 26), leading Sun and co-workers[227] to conclude the existence of spinel-like domains. On the basis of the XRD findings of refs 147 and 227, we speculate that birnessite may indeed undergo a reversible layered ↔ spinel structural transformations as a function of Mg insertion. Analogously, the observed layered → spinel transformation in $LiMnO_2$ has been explained[242] by the presence of highly mobile Mn^{2+} ions, while the reverse transition (spinel → layered, in Mn_3O_4) has also been recently documented in aqueous solutions.[145,243] Therefore, a series of rigorous experimental and theoretical investigations is needed to fully decipher the role of Mg and water in reversible spinel ↔ layered transformations and their reversibility. If the phase transformation spinel ↔ layered is to occur, the impact of spinel inversion (Mg and Mn exchanging sites in the spinel structure) and/or spinel disorder (Mg occupying empty octahedral instead of tetrahedral sites) may have crucial consequences for other spinel/layered electrode systems (e.g., refer to the chalcogenides section 4).

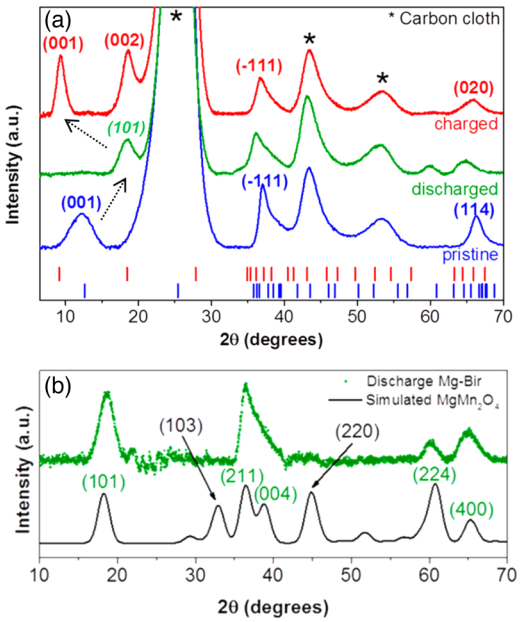

Figure 27. (a) XRD of pristine δ-MnO_2 (blue) and in aqueous setup after discharge (green) and charge (blue) by Sun et al.[227] (b) Comparison of XRD data for the discharged δ-MnO_2 (green) and simulated spinel λ-MnO_2 (black).[227] Reprinted and adapted from ref 227. Copyright 2016 American Chemical Society.

Mg-intercalation in δ-MnO_2 using nonaqueous electrolytes yielded significantly varied results based on the electrochemical setup used. While Nam et al.[147] reported reversible Mg cycling in ACN-based electrolytes, Sun et al.[227] claimed Mg electrochemical cycling with 0.25 M $Mg(TFSI)_2$ in diglyme only after a long process of electrolyte conditioning. Furthermore, water release from the as-synthesized birnessite into the electrolyte (assessed through XRD, XPS, and Karl Fischer titration measurements) could induce passivation at the Mg metal electrode. In parallel, Sun et al.[227] claimed the occurrence of conversion reactions on the MnO_2 surface based on XPS peaks assigned to MnO as well as an increase in hydroxide species. Additionally, experiments using $Mg(TFSI)_2$:diglyme in other oxide cathode materials have reported surface film formation on the Mg-metal anode and electrolyte decomposition at the cathode,[198] highlighting the importance of electrolyte choice and electrochemical setup.

Alfaruqi et al.[244] reported Zn intercalation in δ-MnO_2 using a Zn-metal counter electrode and $ZnSO_4$ aqueous electrolyte, with a 2nd cycle discharge capacity of ~250 mAh/g and continuous capacity fade over 100 cycles (~120 mAh/g at the 100th cycle). Based on ex situ XRD data, the authors speculated the formation of the $ZnMn_2O_4$ spinel, alongside Zn insertion in δ-MnO_2, suggesting a layered → spinel conversion similar to to their previous work[233] and ref 227. Nonetheless, it is difficult to ascertain the formation of the spinel-$ZnMn_2O_4$ phase given the multitude of unindexed/unknown peaks in the XRD data reported,[244] indicating that further investigation is required.

To conclude, reversible Mg intercalation seems to be possible in δ-MnO_2 using aqueous electrolytes,[147,227] in contrast to the conversion reactions afflicting hollandite and tunnel-MnO_2 polymorphs,[158] while reversible Zn intercalation is still debatable.[244] Under these conditions, preliminary investigations via XRD may indicate reversible δ-MnO_2 ↔ λ-MnO_2 transformations as a function of Mg cycling. More experiments are required to decouple the effects of Mn^{2+} dissolution[237−239] and proton intercalation which can significantly impact the electrochemical observations.

λ-MnO_2. The spinel structure, with chemical formula AB_2O_4 comprising the intercalating ion A occupying the tetrahedral

DOI: 10.1021/acs.chemrev.6b00614
Chem. Rev. 2017, 117, 4287−4341

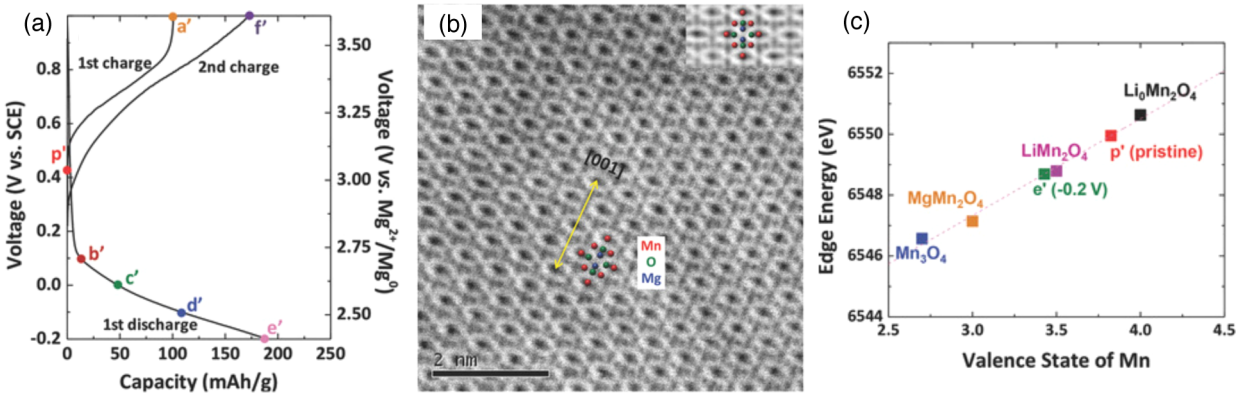

Figure 28. (a) Electrochemical Li deintercalation followed by Mg-intercalation in λ-MnO_2 from $Mg(NO_3)_2$ in water. (b) ABF-STEM image of Mg electrochemically intercalated λ-MnO_2 and relative atom assignment. (c) Mn *K*-edge onset vs valence state for various Mn compounds including magnesiated λ-MnO_2.[236] (a, b, and c) Reprinted with permission from ref 236. Copyright 2015 Wiley-VCH.

sites and B the transition metal filling the octahedral sites in a close-packed oxygen anion sublattice, was first considered as a cathode material for Li-ion batteries by Thackeray et al.[209] in 1984 and to this day remains useful in commercial battery applications due to its high voltage, good structural stability, and fast Li-ion diffusion.[4] Although Mg insertion into spinel-Mn_2O_4, also known as λ-MnO_2, is particularly appealing from the standpoint of the theoretical performance (expected capacity of ~308.3 mAh/g at ~2.9 V),[149,240] calculated Mg migration barriers (~500−800 meV) suggest slow Mg mobility in the oxide-spinel framework.[142,240]

Sinha et al.[203] first reported Mg^{2+} intercalation in spinel Mn_2O_4 by cycling spinel $LiMn_2O_4$ in an aqueous $Mg(NO_3)_2$ electrolyte. In cyclic voltammetry experiments, the authors claimed Li deintercalation forming λ-MnO_2 on the anodic sweep (from −0.7 to 1.2 V vs saturated calomel electrode, SCE) and Mg^{2+} insertion on the cathodic sweep, forming spinel-$MgMn_2O_4$. By comparing the powder XRD pattern of discharged samples with data available for standard $MgMn_2O_4$, the authors verified Mg intercalation and also showed reversible electrochemical behavior for over 20 cycles with ~35 mAh/g capacity. However, the signal-to-noise ratio on the XRD data from discharged $MgMn_2O_4$ samples was quite low.[203] Furthermore, cyclic voltammetry yielded similar peak voltages for both $LiNO_3$ and $Mg(NO_3)_2$ aqueous electrolytes, in contrast to the expectation that Mg intercalation should occur at a different voltage than Li. Similarly, Yuan et al.[204] claimed electrochemical Mg and Zn cycling in λ-MnO_2 obtained through chemical delithiation of $LiMn_2O_4$. In addition to the insufficient structural characterization provided for the discharged state, the reported initial discharge capacity of ~545 mAh/g is incredibly large compared to the theoretical one-electron capacity of ~308.3 mAh/g for inserting 0.5 mol of MV ion per MnO_2 and could stem from sweeping voltages above the potential for water electrolysis (~1.0 V vs SCE), resulting in proton cycling.

Kim et al.,[236] employing in situ XRD, XAS, STEM, and solid-state ^{25}Mg-NMR, observed reversible electrochemical Mg intercalation in an aqueous $Mg(NO_3)_2$ electrolyte. In organic electrolytes [$Mg(TFSI)_2$ in diglyme] a much lower degree of magnesiation was obtained (<3 at. % Mg per Mn_2O_4 measured by integrate in the EDX spectrum) vs aqueous (~11 at. %). In this experiment λ-MnO_2 was initially obtained through delithiation by acid leaching of Li^+ from $LiMn_2O_4$ then discharged at a rate of C/20 to allow for Mg intercalation, as seen in Figure 28a. While XRD measurements were used to track the formation of the tetragonal magnesiated spinel from the cubic empty spinel upon discharge (Figure 28c), ABF-STEM and XAS were used to confirm the presence of Mg^{2+} in the tetrahedral sites (Figure 28b) of the discharged phase and Mn reduction, respectively. Although the authors reported no indication of conversion products during discharge of λ-MnO_2, such as MgO and MnO seen in Hollandite,[158,221] the appearance of unexplained satellite peaks in ^{25}Mg NMR were attributed to the existence of multiple Mg-oxygen environments, with the authors speculating on spinel inversion, where Mg occupies both the tetrahedral and octahedral sites. Spinel inversion in $MgMn_2O_4$ would not only imply Mg occupation of Mn octahedral sites but also Mn^{3+} disproportionation into Mn^{4+} (in octahedral sites) and Mn^{2+} (tetrahedral). Note that some degree of spinel inversion has already been observed in high temperature synthesized $MgMn_2O_4$ and has been attributed to the similar ionic radii of Mg^{2+} and Mn^{3+}.[245−247] Inversion could potentially affect some of the electrochemical properties of the spinel, particularly the Mg^{2+} mobility, though this is still poorly understood. The work reported in ref 145 on Mg intercalation in spinel-MnO_2 in aqueous electrolytes stands in contrast to reports by Sun et al.,[227] showing a reversible layered ↔ spinel transformation during Mg cycling. Similarly Nam et al.[147] obtained the layered Birnessite polymorph by removing Mn^{2+} from spinel-Mn_3O_4, indicating that different MnO_2 polymorphs could be stabilized under different synthesis conditions (see discussion later). Given that only one Mg discharge−charge cycle in λ-MnO_2 was reported,[236] it remains to be seen if prolonged Mg cycling can be achieved in aqueous systems and more analysis is required to assess if subsequent phase transformations are reversible.

Similarly, Cabello et al.[224] first electrochemically demagnesiated a tetragonal $MgMn_2O_4$ ($I4_1/amd$ space group, the typical lattice arrangement of magnesiated λ-MnO_2)[245−247] in aqueous $Mg(NO_3)_2$ electrolyte with a Ag/AgCl reference electrode and a Pt counter electrode. Utilizing the same setup, subsequent Mg discharge/charge cycles showed an initial discharge capacity of ~150 mAh/g, followed by a substantial capacity fade over 20 cycles (capacity at the 20th cycle is ~100 mAh/g). Ex situ XRD measurements revealed reversible Mg removal and intercalation from $MgMn_2O_4$, though the voltammetry and the galvanostatic charge experiments recorded voltages well beyond that of water decomposition (approximately ±1.0 V vs AgCl/Ag), unlike recent reports.[236] Mg reversible intercalation in $MgMn_2O_4$ was

DOI: 10.1021/acs.chemrev.6b00614
Chem. Rev. 2017, 117, 4287−4341

also tested in nonaqueous electrolytes using $Mg(ClO_4)_2$ in ethylene carbonate:diethyl carbonate (EC:DEC, 1:1) against a Pt reference electrode and V_2O_5 (orthorhombic) as the negative electrode, resulting in a constant reversible capacity of ~120 mAh/g for 24 cycles. Though it is known that MnO_2 possesses cubic structure,[227,236,245] the XRD by Cabello et al.[224] of the electrode after cycling curiously suggest the retention of the tetragonal-$MgMn_2O_4$. Given the lack of satisfactory structural characterization, it is possible that the authors[224] could not extract Mg from the magnesiated electrode. Furthermore, the authors[224] did not endeavor to effectively decouple the electrochemical side reactions from Mg intercalation.

Recently Feng, Fenter, and collaborators[226] characterized Mg intercalation with AFM, electrochemistry, synchrotron XRD, XANES, and XPS in both the empty tetragonal and the empty cubic λ-MnO_2 phases, prepared as thin films. It is worth noting that by using a thin film morphology Feng et al.[226] claimed to epitaxially stabilize the cubic form of λ-$MgMn_2O_4$, which would be tetragonal otherwise. Given that the tetragonal spinel is not exactly a distinct phase but rather a Jahn–Teller distortion of the cubic $MgMn_2O_4$ phase, we believe that the existence of the cubic phase is unlikely for $x_{Mg} = 1$, given the presence of Jahn–Teller active Mn ions. While the authors reported Mg (de)intercalation using $Mg(TFSI)_2$ in PC in the cubic polymorph (as shown in Figure 29), confirmed by Mn *K*-edge XANES characterization, surprisingly the tetragonal MnO_2 phase could not (de)intercalate Mg. Feng et al. speculated that spinel inversion could facilitate Mg intercalation in cubic-Mn_2O_4, where inversion causes Mg ions to occupy the octahedral instead of the tetrahedral sites in the structure. However, since Mg occupies its preferred octahedral coordination environment upon spinel inversion, Mg mobility is expected to be reduced,[142] in disagreement with the authors' hypothesis.[226]

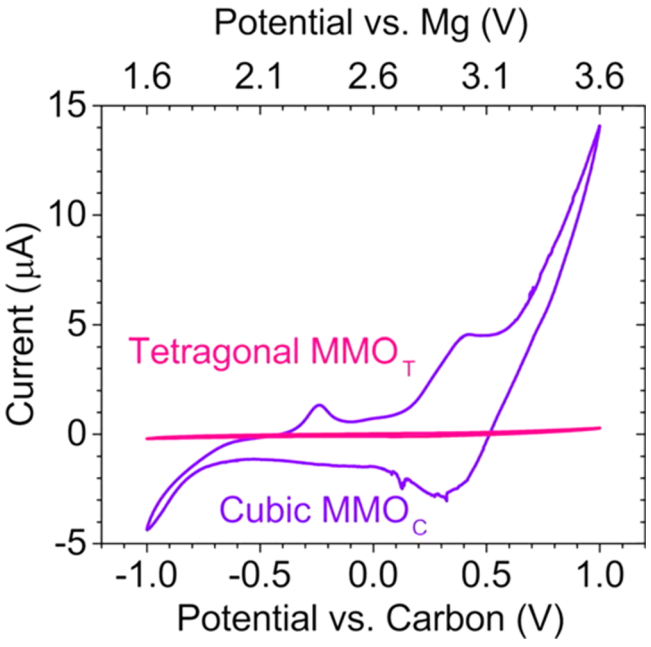

Figure 29. Cyclic voltammetry of tetragonal $I4_1/amd$ (pink) and cubic (purple) MnO_2 thin film coin cells at 1 mV/s scan rate in $Mg(TFSI)_2$:PC from Feng et al.[226] Reprinted and adapted from ref 226. Copyright 2015 American Chemical Society.

Sánchez and Pereira-Ramos,[248] claimed reversible Mg intercalation in a mixed Mn–Co spinel with composition $Mn_{2.15}Co_{0.37}O_4$. $Mg(ClO_4)_2$ or $Mg(CF_3SO_3)_2$ in PC were used as electrolytes while a magnesium rod served as the counter electrode together with a Li/Li^+ reference electrode confined in a separated compartment. The authors observed a first discharge capacity of ~60 mAh/g at an average voltage of ~2.77 V vs Mg with significant hysteresis on discharge/charge cycles. Composition analysis revealed a Mg concentration of ~0.22 per $M_{3-\delta}O_4$ (M = Mn, Co) after discharge, which is lower than the insertion levels achieved for Li in a similar mixed spinel ($x_{Li} \sim 0.62$). The authors attributed the lower reduction with Mg to the higher electrostatic repulsions experienced by the Mg^{2+} during insertion. The XRD characterization of the discharged product $Mg_{0.22}Mn_{2.15}Co_{0.37}O_4$ showed that Mg occupies the vacant octahedral (16*c*) instead of the tetrahedral (8*a*) sites in the structure. In this regard, first-principles calculations clearly indicate that the Mg migration barriers will be higher whenever Mg intercalates into its preferred octahedral coordination environment.[142]

In conclusion, Mg intercalation in λ-MnO_2 seems possible in water-based electrolytes but has not been convincingly demonstrated in nonaqueous electrolytes. However, it remains to be seen whether prolonged cyclability can be achieved in aqueous electrolytes. More pressing is the impact of intricate inversion mechanisms (where Mg^{2+} exchange with Mn^{3+} ions) on Mg cyclability in λ-MnO_2, affecting intrinsic Mg mobility. In parallel, spinel inversion in λ-MnO_2 can drive Mn^{3+} disproportionation into Mn^{4+} and Mn^{2+}, with Mn^{2+} being particularly soluble in water and contributing to potential cathode loss.

Mg Chemical Extraction in λ-MnO_2. Chemical extraction of Li from a range of materials has been used in the past[249−251] to circumvent the difficulties of the electrochemical setup, and this technique was also recently used to investigate the feasibility of Mg and Zn intercalation in λ-MnO_2.[118,223,234]

Mg chemical extraction from $MgMn_2O_4$[223] was investigated using two distinct methods: (i) in acidic (H_2SO_4) environments and (ii) using an oxidizing agent (NO_2BF_4). The authors speculated that Mg acid extraction (with H_2SO_4) follows the disproportionation reaction of $MgMn_2^{3+}O_4 \rightarrow 0.5Mn_2^{4+}O_4 + Mn^{2+}O + MgO$. They also advanced the hypothesis that the rate of Mg extraction could be inversely proportional to the degree of spinel inversion, in qualitative agreement with theoretical predictions.[142,240]

In analogy with their previous work on delithiation of Li-mixed spinels,[251] the authors initially proposed that the Mn^{3+} content in the structure might completely control the reactivity of the NO_2BF_4, mimicking an electrochemical extraction. Mg extraction with NO_2BF_4 was not successful for various degrees of Mg intercalation, which the authors attributed to the electrostatic repulsion felt by Mg^{2+} ions while diffusing between adjacent tetrahedral sites through the spinel structure. The authors also speculated that Mn leaching during the acid treatment (i.e., vacancy formation) promoted the percolation of Mg^{2+} ions, while this would not be the case using an oxidizing agent. However, MgO, which is claimed to be a product of acid treatment, is a basic oxide and should dissolve readily in acid, misleadingly indicating Mg^{2+} extraction instead of oxide conversion. Knight et al.[234] repeated the same experiments to study chemical extraction of Zn from spinel-$ZnMn_2O_4$ in acid and oxidizing environment, arriving at similar conclusions as reported for $MgMn_2O_4$.

DOI: 10.1021/acs.chemrev.6b00614
Chem. Rev. 2017, 117, 4287–4341

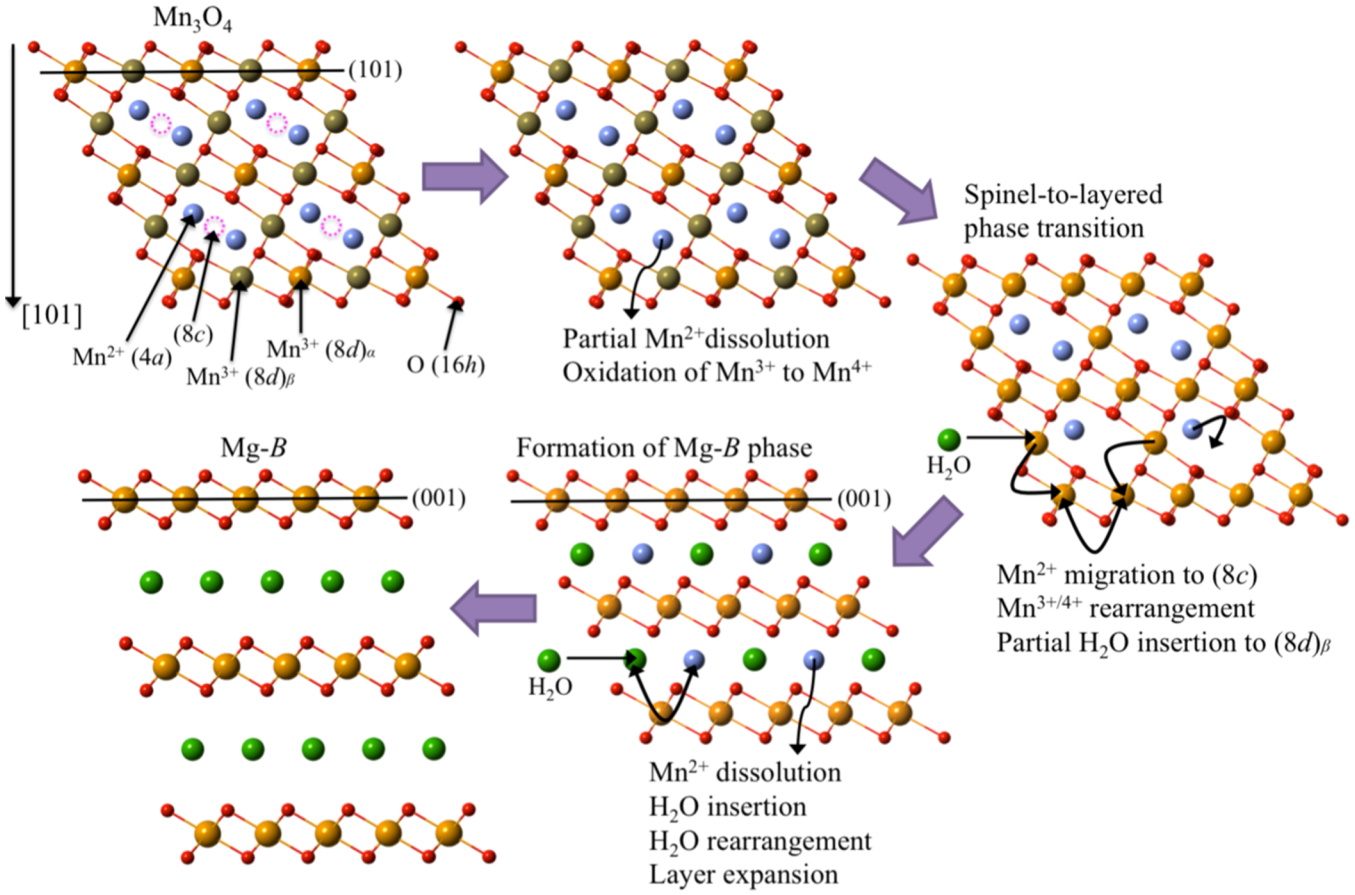

Figure 30. Schematic of the spinel → layered transformation from ref 145, with the 4*a* and 8*d* labels indicating tetrahedral and octahedral sites in the spinel lattice, respectively. Partial removal of Mn^{2+} from Mn_3O_4 facilitates the migration of Mn^{2+} to vacant octahedral 8*c* and intercalation of H_3O^+ ions into the lamellar transient phase. Further water intercalation into the lamellar transient phase leads to lattice expansion and transformation to Birnessite. Reprinted with permission from ref 145. Copyright 2015 Wiley-VCH.

Effect of Water on the Stability of MnO_2 Polymorphs. Recently, Kim and co-workers[145] reported an anomalous spinel → layered transformation in the Mn_2O_4 system (see Figure 30), the inverse of the well-known layered → spinel transformation in $Li_xMn_2O_4$.[242,252] Interestingly, some of the factors that could cause the layered → spinel transition in the $Li_xMn_2O_4$, namely, the high mobility that Mn achieves in a mixed-valence compound can also contribute to the reverse spinel → layered transformation. As first proposed by Reed et al.,[242] Mn can achieve high mobility in close-packed oxides by adopting a Mn^{2+} configuration through a charge-disproportionation reaction of Mn^{3+} during migration to the nearest vacant tetrahedral site. Consistent with the principles laid out for high mobility of cations,[142,240] this gives Mn a low-energy migration path between octahedral sites. Kim et al.[145] speculated that water molecules in the solvent could assist the spinel to layered transformation through the mechanism illustrated in Figure 30, but more investigation is required to support this hypothesis. To demonstrate the phase transformation electrochemically, Kim et al.[145] constructed a cell using the spinel Mn_3O_4 and Ag/AgCl as working and reference electrodes, respectively, with 1 M $MgSO_4$ aqueous electrolyte. Using HAADF and ABF images obtained from STEM measurements, the authors observed Mn^{2+} migration from tetrahedral to octahedral sites, during the first charge of spinel-Mn_3O_4 (Mn^{2+} extraction), leading to the formation of a 2D lamellar transient phase (Figure 30). This mechanism is consistent with the preference of higher-valent Mn for octahedral coordination[253] as well as the existence of sufficient vacancies to facilitate Mn mobility prior to complete oxidation to the 4+ state.[242] Since the measured "interlayer" distance in the transient phase is low (~4.8 Å), the authors speculated that water intercalates into the structure as hydronium (H_3O^+) ions, which are expected to have smaller bond distances with the oxygen in the lattice. Nevertheless, Kim et al. observed an abrupt change in the interlayer spacing from ~4.8 Å to ~7.2 Å upon further intercalation of water, subsequently resulting in the movement of the phase boundary between the transient and spinel phases, and leading to the transformed Birnessite (layered δ-MnO_2) phase. On the basis of electrochemical Mg cycling, the authors hypothesized the formation of Birnessite,[145] which yielded a similar capacity compared to previous reports.[147] Coincidentally, Sun and co-workers[227] advanced the hypothesis that Birnessite could transform into λ-Mn_2O_4 if Mg is intercalated from aqueous electrolytes (see previous sections), but the mechanism triggering the transformation was not explained. In accordance with the XRD data shown in Figure 24b, the Birnessite → spinel transition must undergo a glide transformation of the MnO_2 layers followed by water removal to accommodate the short distance between MnO_2 sheets in the Mg spinel structure (~4.8 Å).

In contrast to ref 147, Kim et al.[236] have shown retention of the spinel-Mn_2O_4 phase during acid leaching of $LiMn_2O_4$ (spinel), while Sun et al.[227] reported the formation of a

DOI: 10.1021/acs.chemrev.6b00614
Chem. Rev. 2017, 117, 4287−4341

Birnessite phase based on hydrothermal synthesis with residual Mg in the pristine structure. Such varied observations emphasize the importance of the synthesis conditions in stabilizing various MnO_2 polymorphs, which is an highly active area of research.[238,254] Also, electrochemical cycling of Mg in MnO_2 could cause reversible phase transformations, such as the spinel ↔ layered transition,[227] necessitating rigorous investigations to unearth the fundamental mechanisms behind Mg intercalation in various MnO_2 polymorphs.

Despite the promise of high theoretical capacity and voltages of MV intercalation in MnO_2, compared to other oxide, sulfide, and polyanion (see later) materials, the comparative analysis presented above demonstrates the complexity of this chemical system. From the examination of Mg literature, it appears that reversible Mg (and Zn) intercalation in Hollandite and tunnel-like phases is not sustainable due to conversion reactions involving the formation of MgO (and ZnO) and various Mn oxides. In contrast, Mg intercalation seems possible in layered MnO_2 but only in aqueous (or water-containing) electrolytes, potentially hindering the use of an energy dense Mg-anode, while it is unclear whether Zn can intercalate reversibly in δ-MnO_2. Although spinel-$MgMn_2O_4$ ($ZnMn_2O_4$) is thermodynamically stable against conversion reactions.[149] The extent of reversible Mg (Zn) intercalation in spinel MnO_2 is still debatable due to contrasting experimental data. The role of water, either as preintercalated molecules in layered MnO_2 or as part of the electrolyte environment, in giving rise to reversible transformations between MnO_2 phases, needs to be evaluated, in particular given that it is well-known that Mn^{3+}/Mn^{2+} are highly mobile species when sufficient cations are present.[242] It is important to emphasize that different from Li-ion batteries, the absence of standard procedures to prepare and conduct MV electrochemical experiments renders the data interpretation extremely challenging. For example, concurrent electrolyte degradation and/or corrosion of current collectors[255] can also contribute to the electrochemical data, highlighting the need for special care in choosing the cell components and the experimental conditions.

5.4. Other Spinels and Post-Spinels

Other Spinels. In this section, the analysis on spinels is extended to oxides comprising transition metals other than Mn. Figure 31 depicts the computed average voltage against gravimetric capacity for different combinations of MV (A) and transition metal ions (M), revealing possible routes to achieve energy densities higher than Li-ion,[240] such as Mg and Ca intercalation in spinel AM_2O_4 where M = Mn, Fe, Co, Ni, and Cr.

While some combinations of transition metals and multivalent ions (Figure 31) suggest promising venues for future experimental investigations, the pressing problem faced by close-packed anion frameworks (as in spinels) is the poor MV ion migration performance in the host structure. Rong and collaborators[142] have recently explained the origins of the high diffusion barriers observed for MV within AM_2O_4 spinels and other close-packed structures. Table 2 lists the migration barriers for several MV ions (Mg^{2+}, Zn^{2+}, Ca^{2+}, and Al^{3+}) computed using first-principles calculations combined with nudged elastic band (NEB) theory. In general, Liu et al.[240] demonstrated in a variety of oxide spinels that the transition metal chemistry does not significantly affect the MV cation diffusion path and the corresponding barriers.

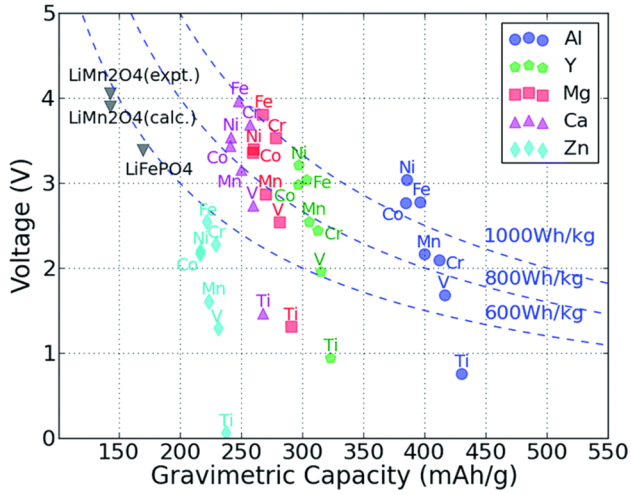

Figure 31. Computed average voltage vs gravimetric capacity for intercalation of A = Zn, Ca, Mg, Y, and Al in B_2O_4 spinels (with B = Mn, Fe, Co, Ni, and Cr) up to composition AB_2O_4. The redox-active metal is marked next to each point. Dashed curves show energy densities of 600 Wh/kg (2400 Wh/l at 4 g/cm^3 density[80]), 800 Wh/kg (3200 Wh/l), and 1000 Wh/kg (4000 Wh/l), respectively, from ref 240. Reproduced from ref 240. Copyright 2015 The Royal Society of Chemistry.

Table 2. Computed MV Migration Barriers (E_m in meV) and Preferred Migration Paths (Path) for AM_2O_4 Spinel Oxides Where M = Mn, Fe, Co, Ni, and Cr in the Charged State (and Discharged State in Brackets)[142,240a]

MV	E_m	path
	Mn_2O_4	
Li	544 (464)	*t*−*o*−*t*
Mg	776 (486)	*t*−*o*−*t*
Zn	1030 (871)	*t*−*o*−*t*
Ca	540 (−)	*t*−*o*−*t*
Al	1428 (−)	*t*−*o*−*t*
	Co_2O_4	
Li	490 (380)	*t*−*o*−*t*
Mg	698 (520)	*t*−*o*−*t*
Zn	983 (821)	*t*−*o*−*t*
Ca	413 (760)	*o*−*t*−*o*
Al	−	−
	Ni_2O_4	
Li	461 (280)	*t*−*o*−*t*
Mg	669 (485)	*t*−*o*−*t*
Zn	925 (554)	*t*−*o*−*t*
Ca	368 (−)	*o*−*t*−*o*
Al	−	−
	Cr_2O_4	
Li	434 (417)	*t*−*o*−*t*
Mg	616 (636)	*t*−*o*−*t*
Zn	880 (855)	*t*−*o*−*t*
Ca	613 (367)	*o*−*t*−*o*
Al	−	−

[a] *t* stands for tetrahedral site and *o* for octahedral.

As discussed at the beginning of section 5, the migration barrier E_m (Table 2) can be at most ∼525 meV when using a micron-sized particle and ∼650 meV in a nanosized particle. In general, a 60 meV variation in the migration energy corresponds to approximately an order of magnitude variation

DOI: 10.1021/acs.chemrev.6b00614
Chem. Rev. 2017, 117, 4287−4341

in diffusivity. The migration path typically connects through a shared three-coordinated face (with energy E_m) between the stable tetrahedral and the intermediate octahedral sites, leading to a unique diffusion topology for the spinel framework, which is tetrahedral → octahedral → tetrahedral (as shown in Table 2). There are systems where the intermediate octahedral site has a lower energy relative to the tetrahedral site, leading to octahedral → tetrahedral → octahedral migration path (e.g., Ca in Cr_2O_4) (see Table 2).[142]

Among the divalent cations, Zn^{2+}(~800−1000 meV) and Mg^{2+}(~600−800 meV) have the highest barriers, while Ca^{2+} is comparable to Li^+(~400−600 meV). The migration barriers for Li^+ in M_2O_4 (M = Mn, Co, Ni, and Cr) fall in the ~400−600 meV range in the empty lattice limit, in agreement with previous literature.[256] With the exclusion of a few Ca-intercalated and CrO_2 spinels, the migration barriers in the high vacancy limit are always higher compared to the dilute vacancy limit. The migration barriers vary significantly with the chemical nature of the diffusing divalent ion, with barriers for $Zn^{2+} > Mg^{2+} > Ca^{2+}$ across all spinel structures. Although Ca^{2+} migration appears facile from these calculations, Ca^{2+} prefers to occupy the vacant octahedral sites in the empty M_2O_4 structures (with the exception of Mn_2O_4) compared to the tetrahedral sites. The tendency of Ca^{2+} toward octahedral sites in spinel may indicate difficulties in synthesizing Ca-intercalated spinels and a driving force toward spinel inversion. Indeed, Ca-containing spinels, with Ca in the tetrahedral sites are found to be relatively unstable from a thermodynamic analysis based on first-principles energies.[142,240]

Despite these findings, it remains to be proven if promising spinel compositions can be synthesized and electrochemically cycled. Nevertheless, theoretical predictions have shown good agreement with experiments before, an example of which is the large Mg migration barriers of Table 2 concurring well with the known difficulties in electrochemical Mg insertion/extraction in spinel cobalt oxides, with reported capacities of ~5 mAh/g.[248]

In 1990, Gregory et al.[53] explored Mg intercalation into RuO_2 from $Mg(ClO_4)_2$:THF in a full-cell using a Mg-metal anode, reporting an overall voltage of ~2.55 V and a 1st discharge capacity of ~266 mAh/g. Although the study only reports the 1st Mg discharge profile and does not provide any structural characterization upon discharge, complete electrochemical reversibility was claimed up to $x_{Mg} = 0.66$, indicating that further investigation is required. Also, the authors suggested a reversible phase separation during Mg intercalation, based on the observed voltage profile, into RuO_2 and $Mg_{0.66}RuO_2$, followed by an irreversible disproportionation of the cathode to MgO and Ru beyond $x_{Mg} = 0.66$.[53] In the same work, a range of other Mg intercalation hosts comprising other oxides (i.e., Co_3O_4, Mn_2O_3, Mn_3O_4, MoO_3, PbO_2, Pb_3O_4, V_2O_5, and WO_3), sulfides (TiS_2, VS_2, and ZrS_2), and borides (MoB_2, TiB_2, and ZrB_2) were tested. Although only capacities and voltages of these materials were published,[53] their structural characterization to ascertain Mg intercalation was missing and urges the battery community to revisit the electrochemical properties of these materials.

Recently Okamoto et al.[257] explored the feasibility of Mg electrochemical intercalation at 150 °C in various spinel oxides such as $MgCo_2O_4$, $MgMn_2O_4$, $MgFe_2O_4$, $MgCr_2O_4$, and Co_3O_4. A three-electrode setup, with Li-ribbon as reference and Mg-ribbon as counter electrodes, was used along with a $Mg(TFSA)_2$/CsTFSA [where TFSA = bis(trifluoromethanesulfonyl)amide] ionic liquid electrolyte. Mg reversible insertion in the magnesiated spinel hosts was verified utilizing ICP, EDX, XANES, and XRD. Though ref 257 claimed Mg intercalation in all the spinel hosts based on EDX analysis, EDX only probes the composition of the nanoparticle. If a sample contains multiple phases, EDX does not identify which phases are magnesiated and thus provides inconclusive evidence of Mg intercalation. XRD data of the materials, at different depths of discharge, were indexed to two phases, namely (i) spinel and (ii) rock salt. Subsequently, the intercalation of more than 1 mol of Mg per TM_2O_4 was assigned to the rock-salt phase, and a reversible spinel ↔ rock-salt transformation was suggested. Nevertheless, all peaks in the XRD spectra of the discharged $MgMn_2O_4$, $MgCo_2O_4$, Co_3O_4, and $MgFe_2O_4$ samples appear particularly broad, with significant presence of MgO, MnO, CoO, and FeO, respectively, thereby suggesting the possible occurrence of parallel conversion reactions.

Post-Spinels. A recent theoretical study suggests that high Mg^{2+} mobility can be achieved in high-pressure phases of the Mn_2O_4 spinel (λ-MnO_2), namely the postspinel structures.[258] Postspinels are categorized into three types according to their crystallographic space-group: (i) $CaMn_2O_4$-type with space group *Pmab*, (ii) $CaTi_2O_4$-type with space group *Cmcm*, and (iii) $CaFe_2O_4$-type with space group *Pnma*. The predicted theoretical capacity for *Pnma* $MgMn_2O_4$ is ~308.3 mAh/g (similar to spinel-MnO_2), and the voltage profile exhibits a steep slope from 2.84 to 1.68 V (computed with DFT+U = 3.9 eV) in ref 258. On the basis of first-principles evaluations, the $CaFe_2O_4$-type (*Pnma*) $MgMn_2O_4$ exhibits a Mg^{2+} migration barrier as low as ~400 meV, comparable to that of Li^+ in commercial cathode materials. Nevertheless, the *Pmab* phase, exhibiting a relatively high migration barrier, is the most stable high-pressure polymorph for stoichiometric $MgMn_2O_4$, with the spinel/postspinel phase transition occurring at ~11.1 GPa. In the Mg-deficient regime, DFT calculations predict that the spinel/postspinel phase transition can occur at relatively lower pressures and form the desired *Pnma* phase. For example, the predicted phase transition pressure for $Mg_{0.5}Mn_2O_4$ and $Mg_{0.25}Mn_2O_4$ is ~7.7 and ~5.4 GPa, respectively. Ling et al.[258] also showed that postspinels can be stabilized by reducing the number of Jahn−Teller centers, for example by doping Mn with Fe as well as introducing Mg vacancies.

Previous experimental work[259,260] indicates that extreme conditions (T > 1000 K) are required to trigger the reverse postspinel → spinel transformation under ambient pressures. In light of the fact that Mg intercalation in some MnO_2 phases could convert into MnO and MgO (and perhaps MnOOH and $Mg(OH)_2$ in aqueous conditions),[158,221,225,227,261] the Toyota R&D team explored the phase stability of the postspinel $MgMn_2O_4$ *Pnma* against conversion reactions with first-principles calculations, as reported in Figure 32. Mg intercalation in the *Pnma* postspinel is stable up to 0.4375 mol of Mg per MnO_2 ($Mg_{0.875}Mn_2O_4$) beyond which conversion to Mn_2O_3 and MgO is expected (Figure 32), even though the stable phase is $MgMn_2O_4$.[258] Further experiments on the postspinel framework's stability during Mg (MV) intercalation are needed to assess the practical electrochemical performance.

Arroyo-de Dompablo et al.[262] recently studied computationally and experimentally [combining DFT, ex situ XRD, potentiodynamic intermittent titration technique (PITT) and SEM] the intercalation of Ca in the postspinel Mn_2O_4 (or marokite, space group *Pmab*) phase. Ca extraction from the postspinel $CaMn_2O_4$ was tested with PITT at 75 °C, using a 0.4

DOI: 10.1021/acs.chemrev.6b00614
Chem. Rev. 2017, 117, 4287−4341

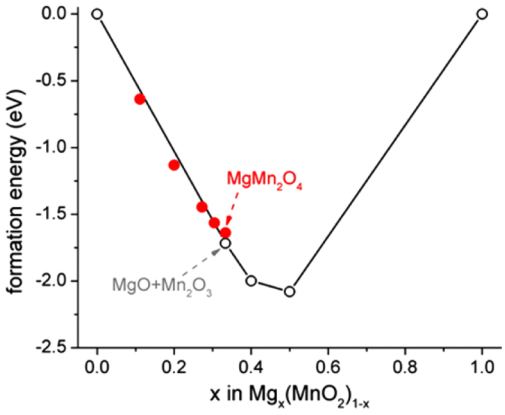

Figure 32. Computed convex hull for Mg intercalation in the $CaFe_2O_4$-type (*Pnma*) postspinel from ref 258, where 0 in the composition axis (x axis) is MnO_2 and 1.0 Mg metal, respectively. The stable phases are indicated by ○. Reprinted from ref 258. Copyright 2013 American Chemical Society.

M solution of $Ca(BF_4)_2$ in a mixture of EC:PC, a Ca-metal counter electrode, and Li as the reference electrode. The PITT response only detected the breakdown of the electrolyte at ~4.3 V, an indication that the only capacity measured arises from the decomposition of the electrolyte. Indeed, analysis of the ex situ XRD data of the electrode after oxidation showed no structural alteration when compared to the pristine sample. Also, first-principles calculations suggested high migration barriers associated with Ca diffusion in the $CaMn_2O_4$-type postspinel structure (~1.8 eV), which decreases slightly (~1.2 eV) when the $CaFe_2O_4$-type Mn_2O_4 is considered.[262] In parallel, the authors also explored the thermodynamics of a postspinel → spinel transformation at $x_{Ca} \sim 1$ because of promising Ca mobility predicted in the hypothetical spinel-$CaMn_2O_4$.[240] However, owing to the high temperature of transformation required for the postspinel → spinel transition (~3000 K, the spinel is highly unstable with Ca in tetrahedral sites), the authors ruled out a solid state process to synthesize spinel-$CaMn_2O_4$ from the postspinel and suggested the exploration of soft-chemistry techniques.

6. POLYANIONS

Due to their excellent cation diffusion, structural stability, and safety, polyanion materials have been a preferred area of Li-ion cathode research in the last 20 years, with the most researched compounds being $LiFePO_4$,[263−265] tavorite phases such as $LiVOPO_4$, $LiVPO_4F$, and $Li(Fe,Mn)SO_4F$,[266−269] and NASICON frameworks.[266,270] Recently, metal organic framework materials, especially Prussian-blue analogues, comprised by both organic molecules (spacers) and transition-metal ions have also received interest as cathode materials for Li, Na, and other ion chemistries.[271,272] In this section, we review the suitability of a few classes of polyanion materials as MV cathodes, including silicates, NASICON-frameworks, fluoro-polyanions, borates, and Prussian-blue structures.

6.1. Olivines

Among the polyanion cathode materials, olivine structures have received the most attention owing to the widespread utilization of $LiFePO_4$ as a Li-ion battery cathode. These compounds have been subsequently examined as Mg intercalation cathodes. In particular, transition metal phosphates and transition metal silicates have been investigated in multiple studies, detailed below.

In addition to improved safety and covalent bonding, silicates in particular afford an opportunity to utilize inexpensive, earth abundant materials (silicon) and present compact SiO_4 tetrahedra expected to facilitate MV diffusion.[273] In particular, $MgFeSiO_4$ is a promising polyanionic cathode material, exhibiting a significantly higher theoretical energy density (~869 Wh/kg, ~2549 Wh/l) than known Mg intercalation cathodes (Chevrel Mo_6S_8, ~77 Wh/kg and ~400 Wh/l; δ-MnO_2, ~690 Wh/kg and ~2329 Wh/l; and V_2O_5, ~325 Wh/kg and ~1188 Wh/l).[273,274] The high energy

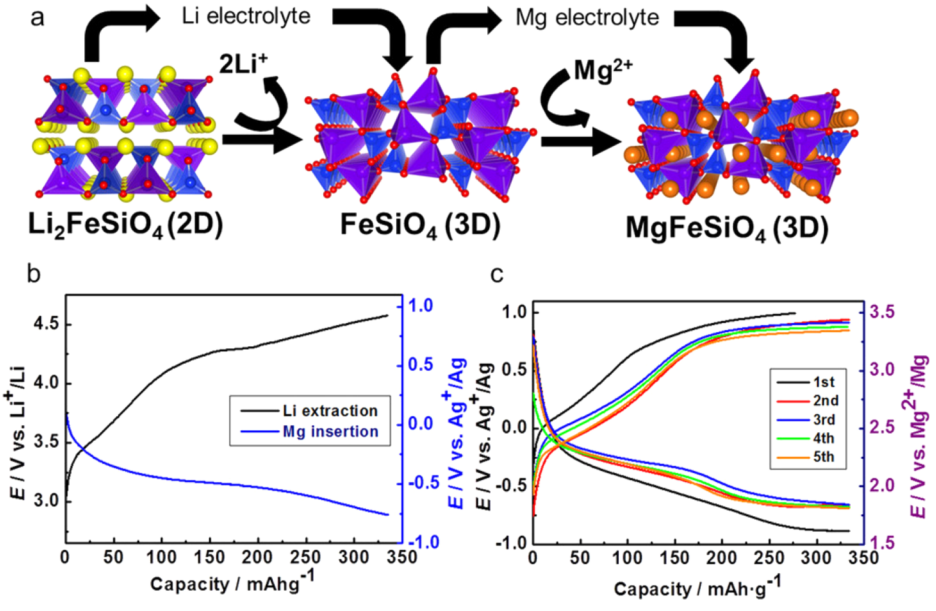

Figure 33. (a) Li/Mg ion-exchange for the electrochemical synthesis of $MgFeSiO_4$ from Li_2FeSiO_4. 2D Percolation network of Li_2FeSiO_4 and 3D framework of $FeSiO_4$ and $MgFeSiO_4$, respectively. (b) Charge−discharge profiles for the ion-exchange process from Li_2FeSiO_4 to $MgFeSiO_4$. (c) Charge−discharge profiles of ion-exchanged $MgFeSiO_4$ at a current density of 6.62 mA/g.[273]

DOI: 10.1021/acs.chemrev.6b00614
Chem. Rev. 2017, 117, 4287−4341

density of $FeSiO_4$ stems from its large gravimetric capacity (~362.4 mAh/g) and relatively high intercalation voltage (~2.4 V vs Mg).

Silicates. Initial attempts to investigate iron silicates as magnesium battery cathodes focused on olivine-$MgFeSiO_4$ prepared by a solid-state synthesis route.[274] However, attempts to cycle Mg in this material yielded less than half of the theoretical capacity.[274] Furthermore, the electrochemical studies in this report utilized a $Mg(AlCl_2EtBu)_2$:THF electrolyte, copper current collectors, and examined voltages in excess of 1.8 V (vs Mg/Mg^{2+}). Because $Mg(AlCl_2EtBu)_2$:THF is known to decompose under these conditions,[273] reactions with the electrolyte cannot be ruled out as a source of spurious capacity. Furthermore, the lack of structural characterization of the cycled materials makes it difficult to adequately assess the electrochemical performance of this material. Facile Mg mobility may not be expected in the as-prepared material because Mg resides in a highly stable octahedral coordination environment.[142]

Better electrochemical performance has been obtained in orthorhombic $MgFeSiO_4$, recently investigated by Orikasa and colleagues.[273] This metastable orthorhombic *Pnma* phase was prepared via electrochemical delithiation of Li_2FeSiO_4 followed by Mg intercalation (see Figure 33b).[273] In contrast to the solid-state synthesis route described above,[274] electrochemical preparation yields a structure presenting tetrahedrally coordinated Mg, as depicted in Figure 33a. Charging and discharging of the $FeSiO_4$ cathode against activated carbon in the presence of a $Mg(TFSI)_2$:ACN electrolyte reversibly furnishes ~330 mAh/g of capacity at ~2.5 V vs Mg (an energy content of approximately 825 Wh/kg and ~2420 Wh/l), shown for five cycles in Figure 33c. The authors also report in situ structural and spectroscopic characterization using XRD and XANES, respectively, which provide compelling evidence that the capacity arises from reversible Mg intercalation. Interestingly, the *K*-edge XANES spectra provide some evidence that some of the exhibited capacity arises from anion oxidation, although this hypothesis would require further investigation to confirm unambiguously.[273]

The authors also attempted to cycle $MgFeSiO_4$ against a Mg metal anode in the presence of $Mg(TFSI)_2$ in triglyme. In these experiments, only half of the theoretical capacity was found to be accessible.[273] Although the authors speculated that optimization of the electrolyte and cell operating conditions can improve the available capacity, only a single charge−discharge cycle was presented, and no further structural characterization of the cycled materials was performed. Thus, it remains to be seen whether a full cell utilizing Mg metal can reversibly furnish the full capacity of this material.[273]

Because tetrahedral coordination is less favorable than octahedral coordination for Mg, it is expected that the less stable, tetrahedrally coordinated Mg site in electrochemically prepared $MgFeSiO_4$ will offer superior Mg diffusivity and improved kinetics for Mg insertion/extraction.[142] It is worth noting that the postspinel structures described in the previous section (see section 5), which exhibit excellent MV ionic conductivity, also crystallize as orthorhombic structures with space group *Pnma*.

The manganese silicate, with a similarly high theoretical energy density (to $MgFeSiO_4$), has also attracted considerable interest as Mg intercalation cathode.[275−280] $MgMnSiO_4$ exhibits a large theoretical capacity for Mg intercalation (364.6 mAh/g) and high voltage (4.1 V for Mn^{4+}/Mn^{3+} and 3.0 V for Mn^{3+}/Mn^{2+} as predicted by DFT+U[281]). As with many similar silicate materials, olivine crystallizes within a hexagonal close packed anion lattice and a *Pbnm* space group as shown in Figure 34a.

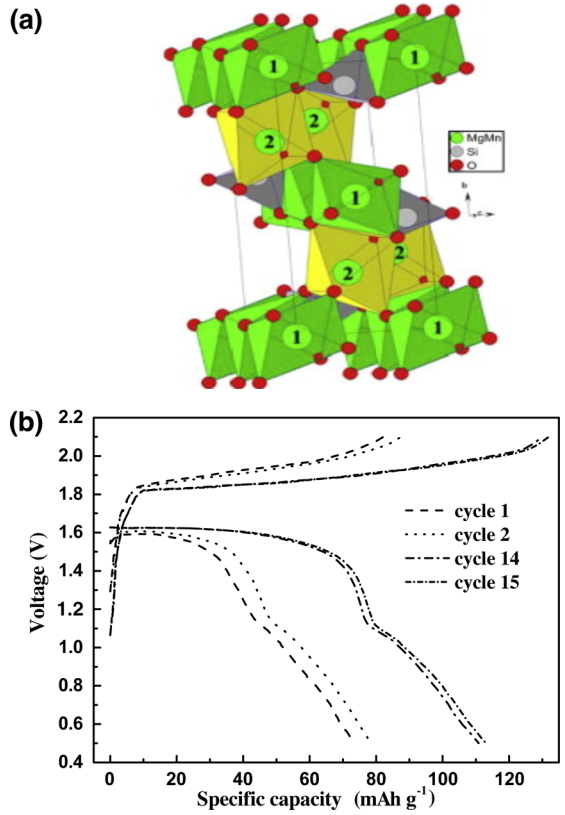

Figure 34. (a) $Mg_{1.03}Mn_{0.97}SiO_4$ structure, where Mn and Mg green and yellow MO_6 octahedrons, respectively, while Si atoms sit in oxygen tetrahedrons (gray).[275] Green MO_6 polyhedrons (marked as 1) are 92% occupied by Mg^{2+} and 8% by Mn ions, while the yellow octahedron (marked as 2) by 89% Mn and 11% Mg. (b) Representative voltage-capacity profile of sol−gel carbon coated $Mg_{1.03}Mn_{0.97}SiO_4$ obtained at a current rate of 12.6 mA/g from ref 275. Voltages are against Mg/Mg^{2+}. (a and b) Reprinted and adapted with permission from ref 275. Copyright 2008 Elsevier.

Mn and Mg ions occupy the yellow and green MO_6 octahedra with 92% and 89% occupancies, respectively. The yellow and green octahedra are corner and edge-sharing, respectively, with the Mg−O bond speculated to be more stable in the green octahedra.[275−280]

Mg insertion into various forms of $Mg_{1.03}Mn_{0.97}SiO_4$ has been attempted by Feng[275] and later NuLi.[277−280,282] Feng et al. compare $Mg_{1.03}Mn_{0.97}SiO_4$ synthesized in two different ways: a solid-state synthesis and a sol−gel synthesis. The primary difference between these samples is particle size, with the sol−gel synthesized particles being considerably smaller (<60 nm) than the solid-state synthesized particles (hundreds of nm after ball milling).[275]

The discharge curve for Mg insertion into $Mn_{0.97}SiO_4$ (against an activated carbon counter electrode) reported by Feng and co-workers of Figure 34b, exhibits two voltage plateaus: one at 1.6 V and another at 1.1 V vs Mg/Mg^{2+}.[275] These voltage plateaus were speculatively attributed to Mg^{2+} insertion into two different octahedron sites, labeled as 1 and 2 in Figure 34a. M1 is the preferred Mg site; because of this, it is expected to be kinetically inferior (more thermodynamically

DOI: 10.1021/acs.chemrev.6b00614
Chem. Rev. 2017, 117, 4287−4341

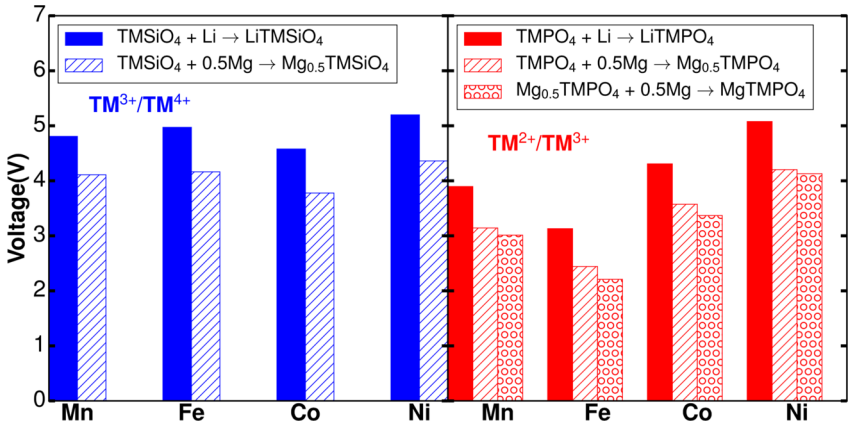

Figure 35. Theoretical voltages for the lithiation and magnesiation of olivine compounds from ref 281. Blue (left): TM^{3+}/TM^{4+}; red (right): TM^{2+}/TM^{3+}. Specific reactions are coded by bar fillings as indicated in figure legends. Reprinted and adapted with permission from ref 281. Copyright 2012 The Royal Society of Chemistry.

stable) than M2, which should present a lower barrier to Mg migration. The maximum capacity attained during the first discharge is ~240 mAh/g (at a low current density of 3.1 mA/g) for the sol–gel sample, while the solid-state sample furnished considerably lower capacities (<80 mAh/g).[275] The higher capacities attained by the nanosized sol–gel sample highlight the importance of synthesis conditions in determining the kinetic performance of the material.

Further evidence of the possible impact of kinetics can be seen in the discharge curves presented in Figure 34b. The amount of capacity provided by the higher voltage plateau was found to be inversely proportional to the discharge rate, consistent with the idea that M2 is kinetically superior to M1. However, a lack of in situ characterization or spectroscopic evidence of Mg insertion in ref 275 makes this claim difficult to verify. Given the small anodic stability of the electrolyte used (~2.5 V[71]), electrolyte side reactions cannot be ruled out as a source of capacity. Notably, smaller particles also present more surface area for possible side reactions, consistent with the higher capacities observed in the sol–gel synthesized sample. Furthermore, the insertion voltages reported in this study disagree qualitatively with DFT-predicted insertion voltages for the Mn redox pairs.[281] This point is further discussed in the following paragraphs.

NuLi and co-workers also examined the possibility of Mg intercalation into various forms of $Mg_{1.03}Mn_{0.97}SiO_4$, including mesoporous[279,282] and nanotube-templated[280] forms of the silicate. Like the sol–gel synthesized nanoparticles described above,[275] these materials exhibit enhanced surface area and reduced dimensionality, possibly yielding improved performance via increased electrolyte contact and improved electronic/ionic mobility. Indeed, the mesoporous $Mg_{1.03}Mn_{0.97}SiO_4$ samples do yield improved capacity (~214 mAh/g)[279,282] and better cyclability (20 cycles without capacity fade). A paucity of in situ characterization in these studies coupled with an unstable electrolyte $Mg(AlCl_2EtBu)_2$, known to react with Cu current collectors, which were used by NuLi et al.,[279] at ~1.8 V as well as qualitative disagreement with DFT-derived insertion voltages (see later) make it difficult to distinguish genuine Mg insertion from electrolyte side-reactions in these reports.

The effect of synthesis conditions and resulting morphology on Mg intercalation into $MnSiO_4$ was recently investigated more systematically by Mori and co-workers.[283] Using a combination of high-resolution SEM and careful XRD analysis of $MgMnSiO_4$ synthesized using a flux method at various temperatures, the authors[283] conclude that samples prepared at lower temperatures exhibit smaller particle size and less antisite mixing (where the extent of antisite mixing describes the amount of Mg occupying corner sharing octahedra, M2 in Figure 34a, instead of the preferred edge-sharing octahedra, which are labeled M1 in Figure 34a). Electrochemical tests utilizing a three-electrode setup with a $Mg(TFSA)_2$ (where TFSA is trifluoromethanesulfonyl amide) electrolyte demonstrated a clear relationship between synthesis temperature and available capacity, with particles synthesized at 450 °C furnishing nearly an order of magnitude more capacity than particles synthesized at 1000 °C (~110 mAh/g vs ~10 mAh/g, respectively). XRD and XANES were employed at various stages of the charge–discharge process to verify the electrochemical intercalation of Mg. It is also worth noting that insertion voltages for Mg measured in this study agree well with DFT-derived predictions for the Mn^{3+}/Mn^{2+} redox couple.[281]

The enhanced performance of the low-temperature particles was attributed to the reduced antisite mixing rather than the smaller particle size (which should presumably improve kinetics). This conclusion was justified by the fact that particles synthesized at 700 and 1000 °C exhibit radically different particle sizes but a similar degree of antisite mixing while still yielding very little capacity. Conversely, the particles synthesized at 450 and 700 °C exhibit similar sizes but differ significantly in the amount of antisite mixing; the 450 °C particles have a much larger capacity. Therefore, the performance differences are attributed to the extent of antisite mixing rather than particle size.[283] This is consistent with the idea that site mixing in the olivine structure reduces Li^+ mobility in $LiFePO_4$.[284]

NuLi et al.[282] as well as Zheng et al.[285] also examined Mg intercalation in the cobalt silicate $CoSiO_4$. The capacity-voltage profiles reported in this study display the expected two-plateau voltage profile resulting from the oxidation/reduction of Co. The voltages reported (~1.6 V for Co^{2+}/Co^{3+}) are considerably lower than DFT-derived voltages (~3.0 V for Co^{2+}/Co^{3+}, Figure 35).[281] As the electrochemical setup [$Mg(AlCl_2EtBu)_2$:THF electrolyte, Cu current collectors] used in this study was the same as the one employed in the Mn-based silicate studies described above, it is possible that similar side reactions affect the $CoSiO_4$ cathode.

DOI: 10.1021/acs.chemrev.6b00614
Chem. Rev. 2017, 117, 4287–4341

Ling and co-workers attempted to rationalize the experimental work on polyanion Mg storage materials, Mg_xTMXO_4 (with TM = Fe, Mn, Co, and Ni; X = Si, P, and S) using DFT calculations.[281] They calculated the thermodynamic stability of the olivine cathode material Mg_xMnSiO_4 at various states of magnesiation and, importantly, found a stable compound at x_{Mg} = 0.5. They also found this composition to be thermodynamically stable for other transition metal silicates. As a result, the authors concluded that Mg extraction/insertion from $MgTMSiO_4/TMSiO_4$ must occur as two steps: from $TMSiO_4$ to $Mg_{0.5}TMSiO_4$ and to $Mg_{1.0}TMSiO_4$.

Bader analysis of the stable Mg_xMnSiO_4 orderings reveals that all Mn atoms in the unit cell have the identical Bader charges at x_{Mg} = 0, 0.5, and 1. The authors assigned the Bader charges to represent Mn^{2+}, Mn^{3+}, and Mn^{4+}, respectively. Intermediate compositions exhibit a mixture of oxidation states, with x_{Mg} = 0.25 presenting a mixture of Mn^{2+}/Mn^{3+} and x_{Mg} = 0.75 presenting a mixture of Mn^{3+}/Mn^{4+}. On the basis of these results, the authors concluded that intercalation of a single Mg atom results in the one-electron reduction of two Mn atoms, rather than a two-electron reduction of a single Mn atom.

The average Mg insertion voltages predicted in this computational study are shown in Figure 35.[281] The predicted voltages for Mg insertion into $MnSiO_4$ are considerably higher (~4.1 V for Mn^{4+}/Mn^{3+} and ~3.0 for Mn^{3+}/Mn^{2+}) than reported experimentally by Feng and co-workers (~1.6 V for Mn^{4+}/Mn^{3+} and ~1.1 for Mn^{3+}/Mn^{2+}).[275] The substantial discrepancy between measured and predicted voltages has not been addressed, but as discussed above, it may originate from side-reactions between the electrolyte and cathode material during electrochemical cycling and the electrochemical response in the work by Feng et al. may not reflect Mg insertion. However, the predicted voltages shown in Figure 35 agree well with the experimental voltages for Mg intercalation into $FeSiO_4$ (Figure 33b).[273] The agreement between experiment and theory for Mg_xFeSiO_4 underscores the importance of the electrochemical experimental setup. Magnesium intercalation into Mn- and Co-silicates was performed using a full-cell setup with a Al−Cl Grignard electrolyte [$Mg(AlCl_2EtBu)_2$:THF],[275−280,282,285] known to be susceptible to side reactions.[71] On the contrary, Mg intercalation into $FeSiO_4$ was done with a three-electrolyte setup using a $Mg(TFSI)_2$:triglyme electrolyte, reducing possible side reactions.[273] More recent studies of Mg into $MnSiO_4$ utilizing a three-electrode setup and $Mg(TFSA)_2$ electrolyte yield much better agreement with these predicted voltages.[283]

A more recent study combined theoretical and experimental characterization to compare Mg mobility in olivine silicate and Chevrel-phase materials.[286] Chevrel-phase $Cu_2Mo_6S_8$ was synthesized by a molten salt method and leached to prepare Mo_6S_8. Olivine silicate materials with the formula $MgTMSiO_4$ (TM = Fe, Mn, and Co) were prepared by sol−gel as well as molten salt methods. Discharging these cathode materials against a magnesium alloy (AZ61) counter electrode in the presence of APC in THF yielded behavior consistent with prior results for the Chevrel phase cathode, while the silicate cathodes all furnished less than 5 mAh/g, far less than the capacities reported by NuLi[279,280,282] or Mori.[283] As neither structural nor chemical characterization of the discharged samples is performed in this study, it is not possible to speculate on the origin of low capacities.

Chen and co-workers simultaneously carried out first-principles calculations of Mg migration barriers in the transition metal silicates.[286] They found large (>600 meV) migration barriers for all transition metals except for $MgCrSiO_4$, which exhibits a 450 meV barrier in the *c* direction. For all transition metals, barriers are substantially higher (2−3 eV) in the *a* and *b* directions than in the *c* direction. The finding of low barriers along only one crystallographic axis is consistent with the well-known one-dimensional diffusion of Li in olivine $LiFePO_4$. The experimental results presented in this study suggest little-to-no attainable capacity for these materials, a conclusion supported by the high Mg migration barriers. However, it is worth noting that this work considered the ground state phase presenting octahedrally coordinated Mg. An earlier study of Mg insertion into the metastable orthorhombic $FeSiO_4$ phase (which coordinates Mg tetrahedrally and would be expected to show better Mg mobility[142]) finds reasonable capacity (>300 mAh/g) and cycle stability.

Although substantial disagreement between measured and predicted Mg insertion voltage persists for the Mn/Co-silicates in a full-cell setup,[275−282,285] the successful intercalation of Mg into $FeSiO_4$[273] and $MnSiO_4$[283] using three-electrode setups, demonstrated by careful in situ structural and spectroscopic characterization[273] as well as agreement with DFT-predicted voltage profiles,[281] highlights the possible utility of olivine silicates as Mg cathode materials. Furthermore, the problematic aspects of the full-cell studies likely arise from the electrochemical setup rather than the cathode itself, providing hope that with judicious choice of electrolyte, reversible Mg insertion into/extraction from these materials will eventually be demonstrated. In light of the excellent energy density and safety offered by silicate cathodes, this avenue is worth pursuing further.

Phosphates. While silicates have received more focus to date, some studies have also considered phosphate cathode materials. Recently, Zhang and Ling, inspired by the success of $LiFePO_4$, examined olivine $FePO_4$, prepared via electrochemical delithiation of $LiFePO_4$, as a magnesium intercalation cathode.[287] Alongside the experiments reported in their study, the authors also carried out first-principles modeling of Mg mobility in $FePO_4$ and $Mg_{0.5}FePO_4$. The authors reported a modest migration barrier (~580 meV) for the charged state ($FePO_4$) but a prohibitively high barrier (~1025 meV) for the discharged state, $Mg_{0.5}FePO_4$. The authors also calculated the thermodynamic stability of $Mg_{0.5}FePO_4$ and found that the compound is metastable against decomposition across an O_2 chemical potential range spanning all practical laboratory conditions.

In light of the instability of $Mg_{0.5}FePO_4$ and reasonable mobility in $FePO_4$, the authors attempted Mg insertion into electrochemically delithiated $FePO_4$ from two different electrolytes [Mg MonoCarborane (MMC) and APC in THF] by discharging against Mg foil. Regardless of the electrolyte use, negligible capacities (~12 mAh/g) were obtained at voltages of ~1.8−1.9 V.[261] Ex situ analysis by XRD indicates that the discharge produced no change in the diffraction pattern, suggesting that the bulk of the $FePO_4$ remains unreacted. The surfaces of the pristine and discharged samples were also examined using FTIR spectroscopy, which revealed a shift to lower frequency of the P−O−P stretching modes. The authors speculated that the shift signals amorphization of the surface on the basis of similar FTIR spectra reported in an earlier study of amorphous iron phosphides.[288] Examination of these particles by TEM revealed that an amorphous surface layer formed on the $FePO_4$ particles following electrochemical discharge. Such a

DOI: 10.1021/acs.chemrev.6b00614
Chem. Rev. 2017, 117, 4287−4341

surface did not form after soaking $FePO_4$ particles in MMC electrolyte, leading the authors to postulate that amorphization was caused by the electrochemical insertion of Mg into the surface. As the attained capacity (12 mAh/g) is consistent with the magnesiation of the outer layer of a 100 nm $FePO_4$ particle, this speculation seems reasonable. Attempts to cycle Li in $FePO_4$ following a discharge−charge cycle in MMC revealed a severe drop in accessible capacity as compared to pristine $FePO_4$, suggesting that the amorphous magnesiated layer passivated the particle surface.

In agreement with first-principles calculations reported in the same study, the magnesiated product of $FePO_4$ is thermodynamically unstable, with surface magnesiation likely forming a passivating amorphous layer. In spite of reasonable Mg migration barriers in the charged state, thermodynamic instability leaves seemingly little hope for $FePO_4$ as a Mg battery cathode. The results reported in this study underscore the simultaneous (and often conflicting[142]) requirement of good kinetics and thermodynamic stability.

6.2. NASICONs

Na Super Ionic CONductors (NASICON) have been investigated both as solid electrolytes and cathode materials, for Li- as well as Na-ion batteries,[289−292] ever since significant Na^+ mobility was demonstrated in these structures.[293] NASICON-frameworks have a chemical formula of $A_xM_2(PO_4)_3$, where A = Li^+, Na^+, or a multivalent ion and M is a transition metal (e.g., Ti, Zr, V, Fe, etc.) and occur in multiple polymorphs, including hexagonal [e.g., $Mg_{0.5}Ti_2(PO_4)_3$, Figure 36a] and monoclinic [$Mg_{0.5}Zr_2(PO_4)_3$, Figure 36b]. All polymorphs are made of MO_6 octahedra, such as the blue TiO_6 and the green ZrO_6 octahedra in Figure 36 (panels a and b, respectively), connected through corners with PO_4 groups (gray tetrahedra in Figure 36). The orange polyhedra of Figure 36 indicate the half-occupied MgO_6 octahedra and MgO_5 pentahedra in the Ti- and Zr-NASICON, respectively. Expectations of good Mg^{2+} mobility, based on good Li^+ and Na^+ mobility, led to the exploration of NASICON-frameworks as both cathode and electrolyte materials for Mg-ion batteries.[294−301]

The $Mg_{0.5}Ti_2(PO_4)_3$-NASICON (Figure 36a), in its pure form and under different doping conditions, has been subjected to galvanostatic Mg discharge[294−296] and measurements of Mg ionic conductivity.[297] Using a three electrode setup of a Mg ribbon counter electrode, the Ag/Ag^+ as reference electrode and $Mg(ClO_4)_2$:PC electrolyte, Makino et al.[294−296] reported galvanostatic Mg discharge in the pure and in acceptor (Fe^{3+}/Cr^{3+})-doped $Mg_{0.5}Ti_2(PO_4)_3$. While the authors demonstrated a voltage plateau of ∼1.0 V at low discharge rates (∼25 $\mu A/cm^2$), and claimed Mg intercalation up to $Mg_{1.5}Ti_2(PO_4)_3$ in the undoped framework, the voltage plateau shrinks rapidly at higher discharge rates (∼100 $\mu A/cm^2$), attributed by the authors to poor Mg mobility within the NASICON-structure (Figure 37a). Fe/Cr-doping does not improve Mg mobilities in the structure, with the authors reporting similar discharge profiles with respect to the undoped NASICON,[295,296] as well as a susceptibility of the material to decompose into $Mg_3(PO_4)_2$ and $MePO_4$ (Me = Fe and Cr) at Mg concentration higher than $Mg(Ti_{1-y}Me_y)_2(PO_4)_3$. Although theoretical calculations indicate a high Mg migration barrier in the $Mg_{0.5}Ti_2(PO_4)_3$-NASICON (Figure 37c),[302] in agreement with the observations by Makino et al., further characterization on the Mg-discharged samples are required to ascertain any Mg intercalation into the structure.

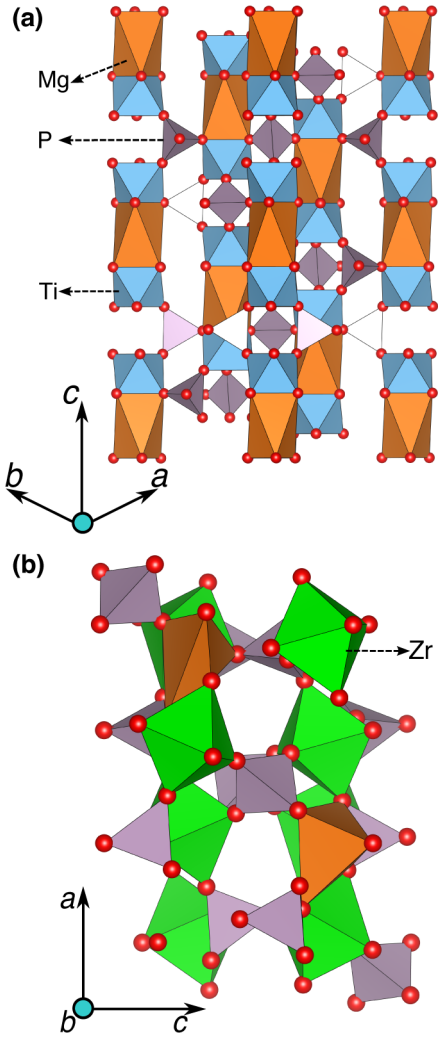

Figure 36. The hexagonal and monoclinic NASICON frameworks are shown in (a and b), respectively. The orange, blue, green, and gray polyhedra indicate Mg, Ti, Zr, and P atoms coordinated by oxygen atoms.

Takahashi et al.[297] determined Mg ionic conductivity using AC impedance measurements under donor (Nb) and acceptor (Fe, Mn, Co) doped $Mg_{0.5}Ti_2(PO_4)_3$. Maximum doping concentrations were 50%, 25%, 10%, and 20% for Fe, Mn, Co, and Nb, respectively, beyond which the structure decomposes into the respective phosphates [e.g., $Co_3(PO_4)_2$ formation on Co-doping]. Rietveld refinement of XRD measurements by the authors revealed contraction of the *c* axis (see Figure 36a and Figure 37b) in acceptor-doped structures (with increasing contraction for Fe > Mn > Co doping), while donor (Nb) doping caused an expansion of the *c* axis. Using Arrhenius plots based on AC impedance data, the authors reported Mg migration barriers of 808, 954, 922, 591, and 1057 meV for the pure, Fe-, Mn-, Co-, and Nb-doped structures, respectively. Although the authors suggested the existence of an optimal level of *c* axis contraction leading to high Mg mobilities, evidenced by the lower migration barriers in the Co-doped samples compared to Fe/Mn-doping, the existence of impurities [such as $Co_3(PO_4)_2$] and secondary

DOI: 10.1021/acs.chemrev.6b00614
Chem. Rev. 2017, 117, 4287−4341

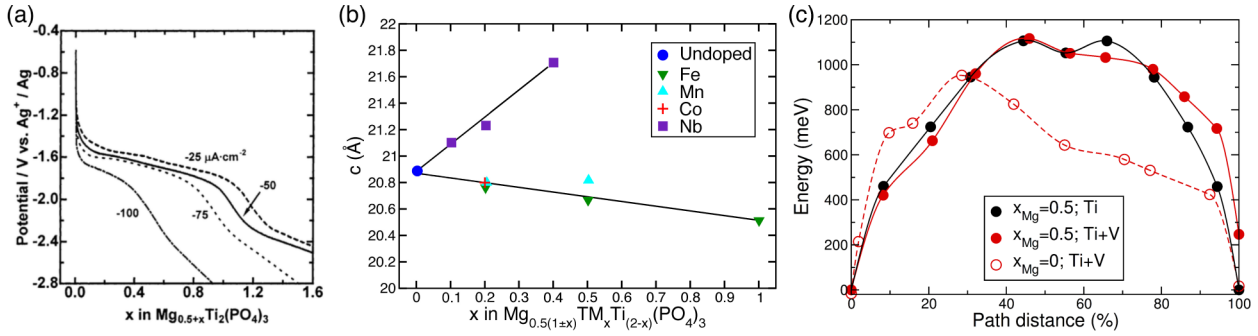

Figure 37. (a) Galvanostatic Mg discharge tests in $Mg_{0.5}Ti_2(PO_4)_3$ at different rates.[294] (b) Evaluation of the *c* lattice parameter under different doping conditions using Rietveld refinement of XRD data digitized from ref 297. (c) Theoretical calculations of Mg migration barriers in the hexagonal-NASICON framework.[302] (a) Reprinted and adapted with permission from ref 294. Copyright 2001 Elsevier.

phases [$Mg_{0.5}(TiO)PO_4$] that appear during sintering could contribute significantly to the ionic conductivities observed.

Calculations of the Mg migration barriers,[302] employing NEB theory along with DFT (for methodological details, see ref 142) were performed for the hexagonal NASICON frameworks of $Mg_{0.5}Ti_2(PO_4)_3$ (solid black line, Figure 37c), $Mg_{0.5}TiV(PO_4)_3$ (solid red line), and $TiV(PO_4)_3$ ($x_{Mg} \sim 0$, dashed red line), respectively. Data from the computations which are in qualitative agreement with the experimental results from Takahashi[297] and others,[294−296] indicate fairly high Mg migration barriers (~1.0 eV) at different Mg concentrations ($x_{Mg} \sim 0$ and 0.5) and transition metal combinations (Ti-only or equal proportions of Ti and V), signifying little potential for the hexagonal NASICON structure to be a potential Mg cathode material. Additionally, the energy difference between the end points (~247 meV) in the $Mg_{0.5}TiV(PO_4)_3$ calculation (solid red line, Figure 37c) reflects an ordered arrangement of Mg atoms and vacancies in the structure.

Huang et al.[298] studied Mg (de)intercalation into the monoclinic $V_2(PO_4)_3$-NASICON host (Figure 36b) at room temperature and at 55 °C. The lithiated phase, $Li_3V_2(PO_4)_3$, was synthesized and electrochemically delithiated, followed by Mg cycling in a three electrode cell, comprising a Mg rod working electrode, a Ag/Ag^+ reference, and $Mg(TFSI)_2$ dissolved in ACN, yielding an average voltage of ~3.0 V vs Mg and a capacity of ~197 mAh/g. While the initial delithiation followed a four-step voltage profile similar to previous reports,[299] subsequent discharge curves displayed a gradual sloping single-phase voltage profile, attributed to structural transformations in the $V_2(PO_4)_3$ by the authors. Composition analysis by Huang et al. revealed both Li^+ and Mg^{2+} presence in the NASICON structure, with significant accumulation of ions on the surface of the cathode as indicated by significant differences in the composition estimates made using ICP and Rietveld refinements of Synchrotron XRD data. Further electrochemical experiments on the delithiated cathode in a freshly prepared Mg cell (devoid of any Li^+ in the electrolyte) showed a voltage profile similar to the case with Li and Mg cointercalation (see Figure 38a), suggesting possible side-reactions.[298] Given that most Mg liquid electrolytes are not stable at voltages of ~3.0 V vs Mg metal,[24,31,32] the significant discrepancies in surface and bulk composition estimates, and the similarities in voltage profiles obtained with and without Li^+ in the electrolyte,[298] reversible Mg^{2+} intercalation into the $V_2(PO_4)_3$-NASICON seems unproven at this time.

The monoclinic NASICON structure has also received attention as a Mg solid-state electrolyte, with experiments

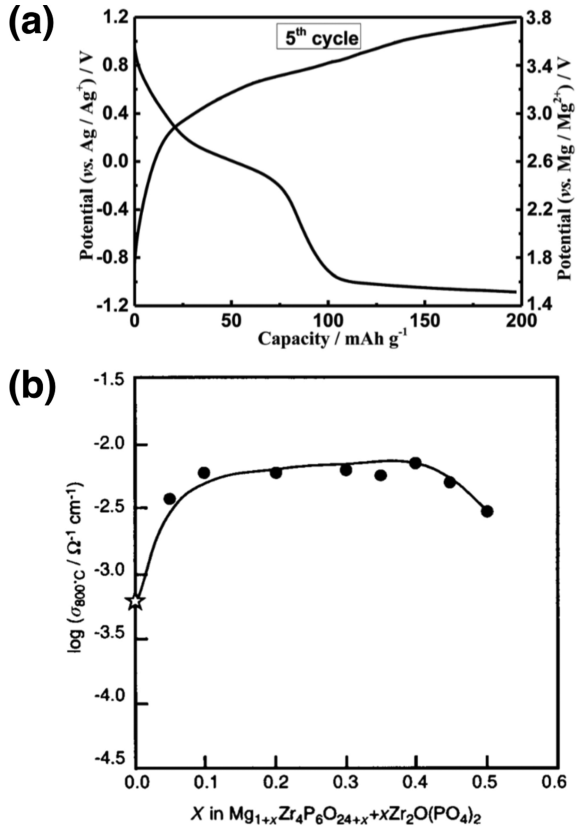

Figure 38. (a) Electrochemical voltage-capacity curve obtained during Mg cycling in Li-free $V_2(PO_4)_3$ structure, with the data shown for the 5th cycle.[298] (b) Variation of measured ionic conductivity with respect to a change in the secondary phase content in the $Mg_{0.5}Zr_2(PO_4)_3$-NASICON.[301] (a) Reproduced and adapted with permission from ref 298. Copyright 2015 The Royal Society of Chemistry. (b) Reproduced and adapted with permission from ref 301. Copyright 2000 The Royal Society of Chemistry.

reported specifically on the $Mg_{0.5}Zr_2(PO_4)_3$ structure.[300,301] Anuar et al.[300] reported Mg conductivity of ~10^{-5} S/cm at 500 °C (~10^{-6} S/cm at 298 K) on a sample sintered at 750 °C, with an electrochemical stability window of ~2.5 V vs Mg. The extrapolated migration barrier for Mg diffusion (~97 meV, obtained from Arrhenius plots) seems inconsistent with the low conductivity values reported in ref 300. An activation energy of 97 meV would be expected to lead to very high ionic conductivity, in contrast with observations in ref 300. For comparison, excellent ionic conductors for Li^+ and Na^+ have

DOI: 10.1021/acs.chemrev.6b00614
Chem. Rev. 2017, 117, 4287−4341

ionic conductivities in the $\approx 10^{-3}$ S/cm at 298 K and activation energies in the 200−350 meV range.[113,290] Imanaka et al.[301] explored the influence of a secondary phase addition, $Zr_2O(PO_4)_2$, on the Mg-conductivity in the Zr-NASICON. The authors found a monotonous improvement in conductivity with the addition of the secondary phase, reaching a maximum of ∼6.92 mS/cm at 800 °C corresponding to ∼40% addition (Figure 38b). While the increase in Mg conductivity was attributed to the improved density of the composite samples by the authors, the contribution of mobile ions within the secondary phase to the observed ionic conductivities is unclear. Additionally, the high Mg migration barriers calculated by Imanaka et al. (∼1407 meV) does not show promise for room temperature Mg conductivity, which is critical for Mg solid-electrolytes. Mg-containing compounds should certainly be explored for potential MV solid state electrolytes as that could mitigate several issues faced by current liquid Mg electrolytes.[113,303,304]

6.3. Fluoro-Polyanions

Experimental[305] and theoretical[306,307] studies of Mg intercalation in fluoro-polyanion structures have been primarily motivated by the hypothesis that the introduction of F weakens the Mg-anion interactions, yielding increased ionic conductivity. Although no clear evidence of improved Mg mobilities has been reported by experiments so far, theoretical predictions of low Mg migration barriers in the $FeSO_4F$-structure[306] indicate promise and a potential chemical space to explore in the future.

Huang et al.[305] reported electrochemical Mg cycling starting from the $MgFePO_4F$-carbon nanotube (CNT) composite working electrode and using a 0.5 M $Mg(TFSI)_2$ electrolyte, referenced to a Ag/Ag^+ electrode with a Mg rod as counter electrode. While showing good cyclability (∼10 cycles) at a high voltage (∼2.6 V vs Mg/Mg^{2+}), the $FePO_4F$ cathodes suffered from low capacities, ∼38 mAh/g at C/20, and poor Coulombic efficiencies (∼80%), resulting in low energy densities of approximatively 99 Wh/kg and ∼295 Wh/l, respectively. From the structural characterization after synthesis, the authors found significant antisite mixing between the Fe and Mg species, as shown by the mixed occupancy of sites M1 and M2 in Figure 39b. Further, Huang et al. attributed the limited Mg mobility and the low capacity observed (compared to the theoretical value of ∼157.8 mAh/g) in the structure to the antisite defects blocking some of the Mg percolation channels within the structure. Although the Coulombic efficiencies could be improved by controlling electrode−electrolyte side reactions,[305] attention needs to be directed toward understanding the exact conditions limiting both Mg mobility and capacity in the $FePO_4F$-structure.

Theoretical work by Wu and co-workers[306,307] highlighted the possibilities of the Tavorite-$FeSO_4F$ and VPO_4F as cathode materials for Mg batteries. While the calculated discharge voltage of $FeSO_4F$ is ∼2.52 V vs Mg/Mg^{2+} (Fe^{3+}/Fe^{2+}), VPO_4F shows voltage plateaus of ∼2.6 and ∼1.5 V for the V^{4+}/V^{3+} and V^{3+}/V^{2+} couples, respectively. Calculation of Mg migration, coupling DFT and NEB theory, in VPO_4F indicate a 1D conduction channel (as in Figure 39a) with a barrier of ∼704 meV, whereas the barrier for a similar 1D channel in $FeSO_4F$ is more promising (∼360 meV). Although the theoretical data on the magnesiated VPO_4F and Tavorite-$FeSO_4F$ is promising, synthesis and electrochemical studies need to be undertaken in these systems to confirm their potential as cathode materials.

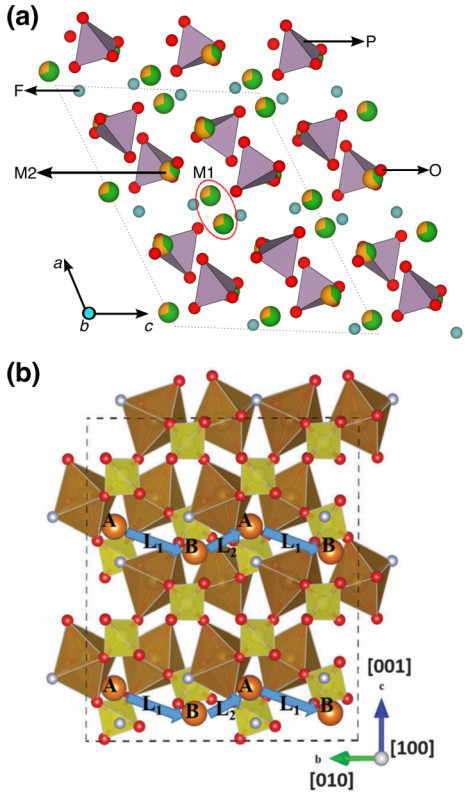

Figure 39. (a) $MgFePO_4F$ structure adapted from ref 305 showing M1 and M2 sites with mixed occupancies of both Fe and Mg. (b) Mg migration path (L1 + L2) in the $FeSO_4F$ structure from ref 306. (a) Reproduced and adapted with permission from ref 305. Copyright 2014 The Royal Society of Chemistry. (b) Reproduced with permission from ref 306. Copyright The PCCP Owner Societies.

6.4. Borates

Of the common oxo-anion groups, borates exhibit the lowest mass/charge ratio and therefore offer higher specific capacities. Furthermore, because the edge sharing chains of MO_6 octahedra of these structures can give rise to metallic conduction,[308] electrical conductivity in many borates is likely sufficient for electrochemical cycling. While a number of studies have examined borate compounds for Li-ion batteries,[309−311] two borate frameworks, M_2BO_4 orthoborates and $M_2B_2O_5$ pyroborates, were recently investigated as potential Mg intercalation compounds.[312]

The orthoborate and pyroborate structures present two different crystallographic M cation sites, labeled M_A and M_B in Figure 40a, which depicts these frameworks. In their recent work,[312] Bo and co-workers investigated $MgVBO_4$ (orthoborate) and two compositions of the pyroborate compound $Mg_xFe_{2-x}B_2O_5$ with $x = 2/3$ and $x = 4/3$. Each compound was synthesized using a solid-state route, and the structures were refined from time-of-flight neutron diffraction as well as XRD measurements. $MgVBO_4$ was found to exhibit some cation disorder, with Mg^{2+} showing a strong preference for the M_A site (79% occupancy) and V favoring the M_B site in the same amount. In contrast, structural refinements of $Mg_{2/3}Fe_{4/3}B_2O_5$ and $Mg_{4/3}Fe_{2/3}B_2O_5$ suggested a random distribution of Mg and Fe over the M_A and M_B sites.

In addition to the synthesis and structural refinement of each compound, Bo et al. carried out a preliminary assessment of Mg mobility in the borate frameworks by attempting Mg removal

DOI: 10.1021/acs.chemrev.6b00614
Chem. Rev. 2017, 117, 4287−4341

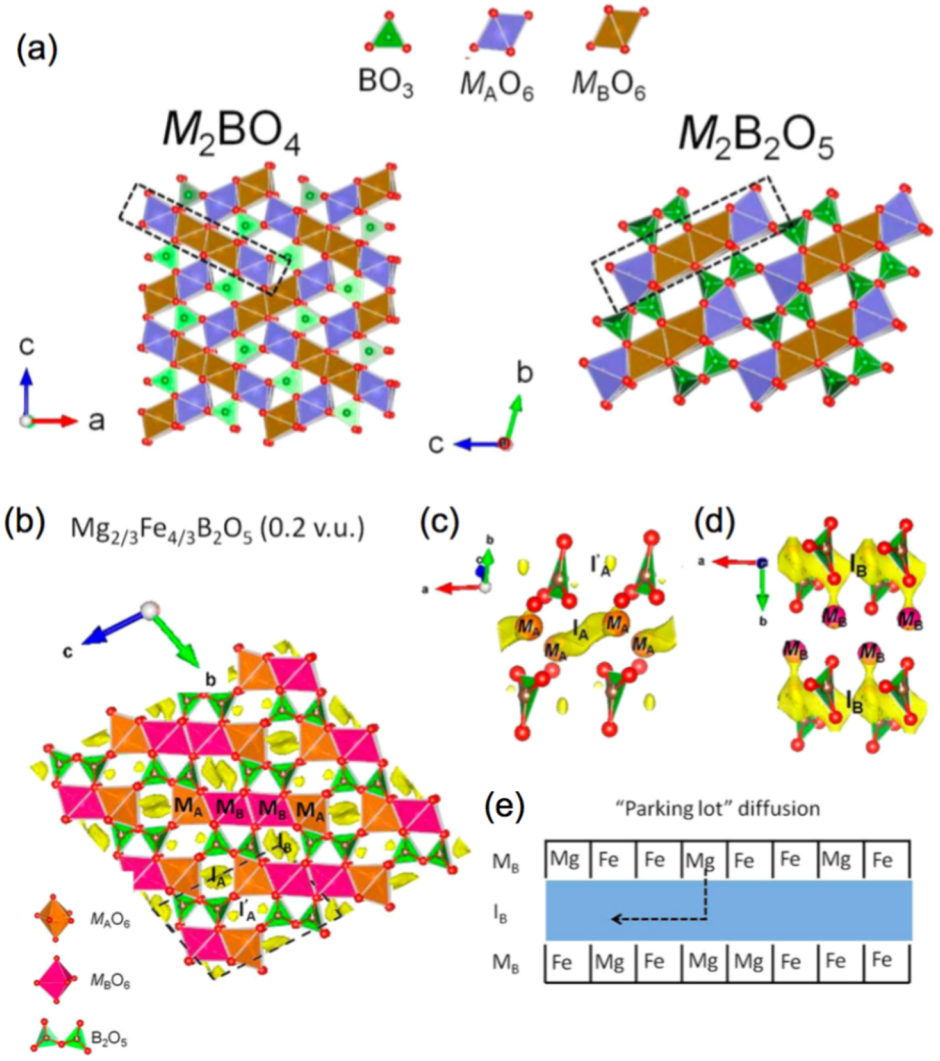

Figure 40. (a) Crystal structures of the orthoborate (M_2BO_4) and pyroborate ($M_2B_2O_5$) compounds, where M is a di- or trivalent ion. Dashed rectangles indicate ribbons of Mg^{2+} edge-sharing octahedra. The ribbons contain two distinct crystallographic sites, with outer sites denoted M_A (blue octahedra) and inner sites denoted M_B (brown octahedra). (b) Bond valence sum mismatch map along the *a* axis, revealing impeded diffusion in the *bc* plane. Black dotted lines indicate the $Mg_{2/3}Fe_{4/3}B_2O_5$ unit cell, with the three unique interstitials I_A, I'_A, and I_B. In (c and d), only the I_B sites form a percolation channel. (e) A schematic of the "parking lot" diffusion motif discussed in text and adapted from ref 312. (a, b, c, d, and e) Reprinted and adapted with permission from ref 312. Copyright 2015 American Chemical Society.

via chemical and thermal oxidation.[312] $MgVBO_4$ did not show any evidence for demagnesiation in response to immersion in a saturated aqueous $K_2S_2O_8$ solution (chemical oxidation) nor to sustained heating in the presence of oxidation (thermal oxidation). On the basis of these experiments, the authors concluded that $MgVBO_4$ is unsuitable for electrochemical applications. The iron borate samples ($Mg_{2/3}Fe_{4/3}B_2O_5$ and $Mg_{4/3}Fe_{2/3}B_2O_5$) proved similarly resistant to chemical oxidation by a saturated $K_2S_2O_8$ solution. However, it was found that thermal oxidation and Mg loss could occur in both iron borate samples in the temperature range of 200−500 °C without loss of the underlying lattice structure. Mg loss and lattice stability was suggested on the basis of TGA and ex situ XRD measurements on thermally oxidized samples. Structural refinement of thermally oxidized samples indicated that Mg loss occurs almost exclusively from the M_B site. Considering the random distribution of Mg across the A and B sites, half of the Mg theoretical capacity (amounting to 186 mAh/g) may be accessible at elevated temperatures.[312]

Bond valence sum (BVS) mismatch maps were used to rationalize the difference in Mg mobility between the $MgVBO_4$ and $Mg_xFe_{2-x}B_2O_5$ samples. Analysis of BVS mismatch maps revealed a lack of percolation pathways in $MgVBO_4$. On the other hand, BVS mismatch maps of the $Mg_xFe_{2-x}B_2O_5$ structure contain three distinct interstitial sites (I_A, I'_A, and I_B) accessible to Mg^{2+} ions, as shown in Figure 40 (panels b and c). The interstitial sites are indexed based on the type of adjacent cation site (i.e., I_A interstitials connect M_A sites). Of these three sites, only the site labeled I_B in Figure 40c creates a percolation path. The formation of a percolating network of interstitial sites led the authors to propose a defect-tolerant "parking lot" diffusion mechanism, depicted schematically in Figure 40e, whereby the diffusion of Mg^{2+} proceeds without needing to pass through other M_B octahedra and so is unaffected by the type of atom occupying them.

Although seemingly defect-tolerant, the microscopic reversibility of the hop between a M_B site and a I_B interstitial suggests the presence of competing effects on Mg diffusion kinetics. While a higher percentage of Mg ions in M_B sites should

DOI: 10.1021/acs.chemrev.6b00614
Chem. Rev. 2017, 117, 4287−4341

presumably improve mobility by connecting more Mg sites to percolating interstitial networks, a larger number of Mg ions in interstitial sites necessarily implies a larger number of "open" parking spaces, increasing the chance that a diffusing Mg atom will "park" in one of these empty spaces and transiently cease contributing to ionic diffusion. Therefore, it is unclear whether the parking lot-style diffusion is beneficial to ionic mobility.

While the parking lot diffusion mechanism remains unproven, the finding that only I_B interstitials (those connecting M_B sites) form a percolating network is consistent with Mg removal exclusively from M_B sites. The lack of percolating networks and preferential occupation of the less-mobile M_A site in $MgVBO_4$ explains the resistance of this material to demagnesiation. It would be useful to corroborate these findings with more accurate ab initio calculations of Mg mobility.

At this time, the limited amount of investigation into Mg intercalation in borates shows little promise for this class of compounds. $MgVBO_4$ was found to be entirely unsuitable for electrochemical applications, while $Mg_xFe_{2-x}B_2O_5$ required temperatures in excess of 200 °C to render even half of its Mg capacity accessible. As these temperatures exceed the operational range of most battery devices, borate materials would seem to lack sufficient Mg mobility to be of practical utility in this application.

6.5. Prussian Blue Analogues

Recently, hybrid framework materials comprised of inexpensive organic molecules bonded through transition metal ions called metal organic frameworks have been explored as novel cathode materials (Figure 41a). The versatile nature of metal organic frameworks, together with the possibility of modulating the size of the intercalation channels, has stimulated interest in the quest for new MV-cathode materials in this chemical space.[271,272,313−321] In particular, Prussian blue (PB) is a metal organic framework nanomaterial with formula $A_xMM'(CN)_6{\cdot}yH_2O$, analogous to AMX_3 perovskites but with A as a MV ion, and M and M′ as transition metals, as shown in Figure 41a.

The large open cages, illustrated in Figure 41a, originating from the coordination of cyanide groups (CN^-) with the transition metal ions (e.g., Ni, Cu, Fe, etc.) are believed to ease the insertion of multivalent ions and small solvent molecules (e.g., H_2O). Of note, PB analogues have demonstrated reversible intercalation of a multitude of multivalent ions including Mg^{2+}, Ca^{2+}, Sr^{2+}, Ba^{2+}, Co^{2+}, Ni^{2+}, Cu^{2+}, Zn^{2+}, Pb^{2+}, Al^{3+}, Y^{3+}, La^{3+}, Ce^{3+}, Nd^{3+} and Sm^{3+} from both aqueous and nonaqueous electrolytes.[271,272,313−321]

While Wang et al.[271,272] have demonstrated excellent electrochemical cyclability (~2000 cycles without capacity fading) of Rb^+, Mg^{2+}, Ca^{2+}, Sr^{2+}, Ba^{2+}, Co^{2+}, Ni^{2+}, Cu^{2+}, Zn^{2+}, Pb^{2+}, Al^{3+}, Y^{3+}, La^{3+}, Ce^{3+}, Nd^{3+}, and Sm^{3+} in PB from aqueous electrolytes (see Figure 41, panels b and c), the insertion voltages (~0.60 — 1.3 V vs SHE) as well as the specific capacities (~30−60 mAh/g) are poor, resulting in energy densities of ~102 Wh/kg and ~171 Wh/l that are far-off from the expectations (section 2) of a practical MV battery.

Recently, Lipson and collaborators,[318] utilizing a coin-cell setup, reported reversible Ca insertion in $MnFe(CN)_6$ from nonaqueous electrolytes ($Ca(PF_6)_2$ in a mixture of EC:PC) and a BP2000 carbon anode with a 1st discharge capacity of ~100 mAh/g. Similar to MV insertion from aqueous electrolyte of Figure 41c, the Galvanostatic charge−discharge curves in ref

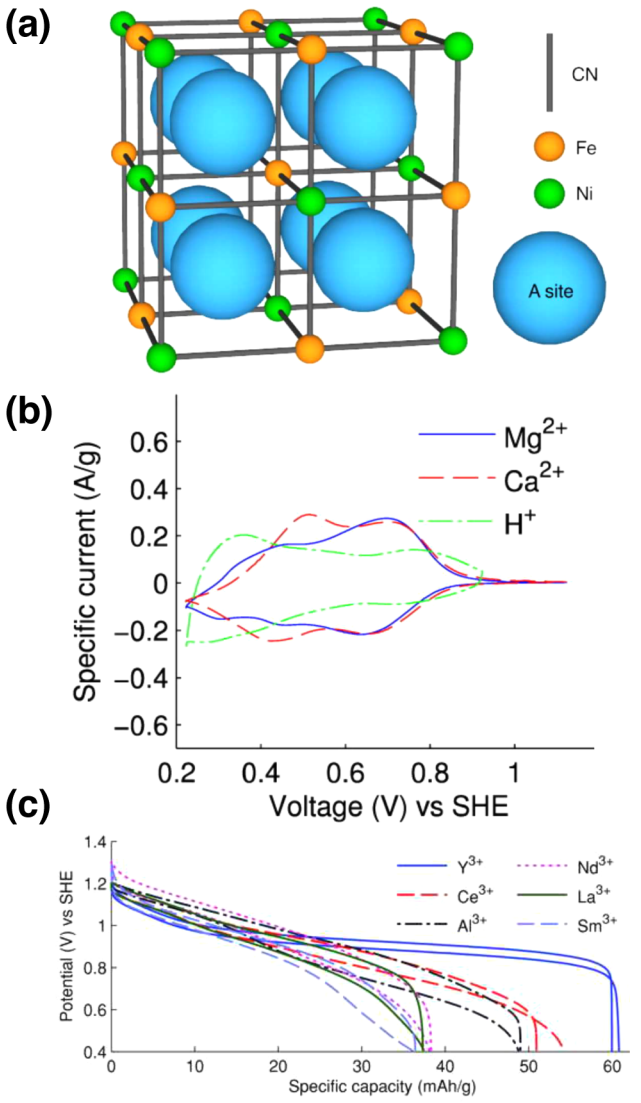

Figure 41. (a) Structure of Prussian Blue analogues,[271] (b) voltammetry for mono- and divalent cation intercalation[271] (i.e., H, Mg, and Ca) in PB, and (c) galvanostatic charge and discharge for trivalent ion intercalation[272] (i.e., Y, Ce, Al, Nd, La and Sm), in PB from aqueous electrolytes. (a and b) Reprinted and adapted from ref 271. Copyright 2013 American Chemical Society. (c) Reprinted with permission from ref 272. Copyright 2015 Wiley-VCH.

318 showed a single plateau, suggesting that only one transition metal [among Mn and Fe in $MnFe(CN)_6$] undergoes reduction upon Ca insertion. Synchrotron XRD measurements in Figure 42a showed substantial, reversible changes of the peak located at ~2.35 $Å^{-1}$ when the cathode is discharged, suggesting Ca intercalation in the Prussian Blue material. Additionally, the ex situ Mn K-edge XANES spectra, recorded at different states of discharge in Figure 42b, demonstrated clear $Mn^{2+/3+}$ redox activity upon insertion. In contrast, the Fe K-edge XANES spectra (omitted for brevity) indicated that Fe remains predominantly in the 3+ oxidation state, which was also supported by cyclic voltammetry measurements (also omitted).

Subsequently, the authors[318] attempted to cycle a full cell with a calciated Sn-metal anode, as shown in Figure 43, and reported reversible Ca intercalation with a first discharge capacity of ~90 mAh/g at ~2.4 V and a 100% Coulombic efficiency for about 35 cycles. Data from Figure 43b[318] show a

DOI: 10.1021/acs.chemrev.6b00614
Chem. Rev. 2017, 117, 4287−4341

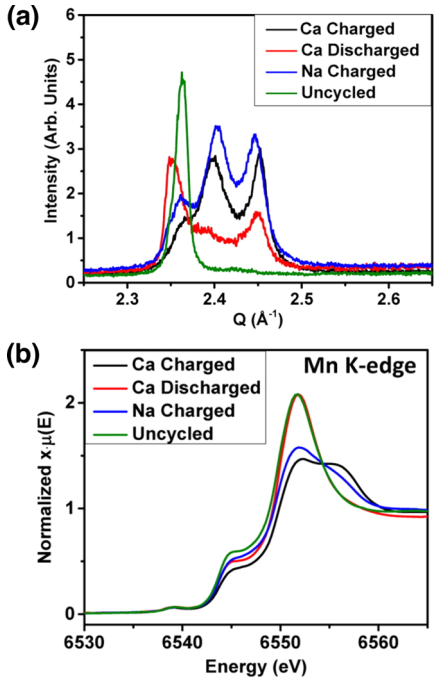

Figure 42. (a) XRD and (b) normalized Mn K-edge ex situ XANES of $MnFe(CN)_6$ at different stages of Ca intercalation from Lipson et al.[318] (a and b) Reprinted and adapted from ref 318. Copyright 2015 American Chemical Society.

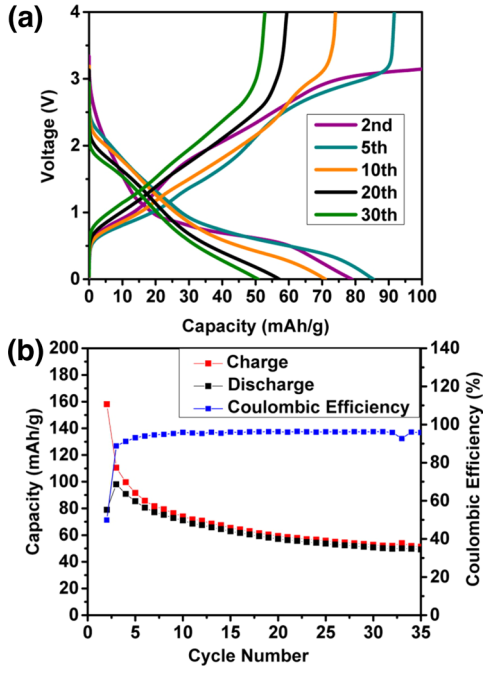

Figure 43. (a) Galvanostatic charge−discharge curves of Ca intercalation in $MnFe(CN)_6$ Prussian Blue analogues in $Ca(PF_6)_2$ electrolyte in a mixture of EC:PC and using calciated Sn as anode from Lipson et al.[318] (b) Capacity and Coulombic efficiency vs cycle number. (a and b) Reprinted and adapted from ref 318. Copyright 2015 American Chemical Society.

non-negligible capacity fade (~35% reduction of the initial capacity) and was speculatively attributed by Lipson et al.[318] to possible delamination of the Sn-anode (caused by substantial volume expansion upon Ca insertion), Sn dissolution in the electrolyte, and an increase in cell resistance (possibly due to surface film formation).

Computational reports of ion intercalation in PB systems are also available.[322,323] Ling and Mizuno at Toyota R&D[322] reported an exhaustive first-principles investigation to assess the intercalation of multivalent ions (Mg^{2+}, Ca^{2+}, Sr^{2+}, and Ba^{2+}) in $Fe[Fe(CN)_6]$ and underscored that ion insertion in this material is strongly affected by the ionic radius of the intercalant ion (as indicated in Figure 44). Since PB analogues

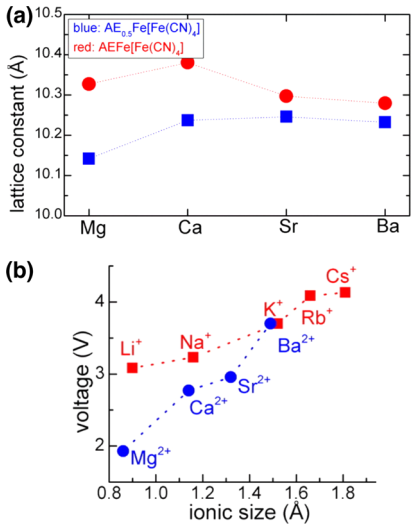

Figure 44. (a) Trend of lattice constants (computed with first-principles calculations) in $Fe[Fe(CN)_6]$ as a function of MV (AE = alkaline-earth) ion at x = 0.5 and x = 1.0, respectively, from Ling et al.[322] (b) DFT+U computed intercalation voltages for x = 0.0 to x = 0.5 for MV ions ($Fe^{2+/3+}$ ions were treated in their low-spin state).[322] (a and b) Reprinted and adapted from ref 318. Copyright 2015 American Chemical Society.

are not compact structures, the insertion of large ions, such as Ca^{2+}, Sr^{2+}, and Ba^{2+}, only marginally affects (~2% about 0.2 Å) the cell lattice parameter of $Fe[Fe(CN)_6]$. Interestingly, the DFT-derived insertion voltages for MV ions, displayed in Figure 44b increase as a function of ionic radius, suggesting that slightly larger energy densities are achievable by intercalating larger cations.

PB is an interesting proof of concept to show that structures with larger voids can tolerate the diffusion of highly polarizing di- and trivalent ions. Furthermore, the cointercalation of solvent molecules (or water) may improve the kinetics of ion intercalation, similar to the enhancement observed in V_2O_5 and MnO_2 cathodes (section 5). Though from a technical perspective any participation of the electrolyte solvent in the intercalation reaction requires a practical cell with a considerable amount of electrolyte, thus reducing further the energy density. PB therefore represents a good platform for studying the intercalation of large ions, such as Ca^{2+}, Sr^{2+}, and Ba^{2+}, whose electrochemistry is less explored at the moment. But, the fate of solvent (or water) molecules, which likely play an important role in PB systems (similar to some oxides as discussed in the beginning of section 5), is scarcely documented and often overlooked. As discussed in previous sections, it is expected that water could actively participate in the material electrochemistry for example by providing readily cyclable protons or favoring/inhibiting MV intercalation in the PB framework. Nonetheless, the low energy densities yielded by

DOI: 10.1021/acs.chemrev.6b00614
Chem. Rev. 2017, 117, 4287−4341

Table 3. Summary of All Materials That Have Been Experimentally Attempted As Intercalation Cathodes for Mg[a]

material	energy density		ρ	status
	gravimetric	volumetric		
		Chalcogenides		
Chevrel-Mo_6S_8[12]	77	400	5.20[83]	Mg full-cell done
Spinel-Ti_2S_4[121]	228	731	3.20[125]	Mg full-cell done
layered-TiS_2[123]	192	623	3.24[126]	capacity fade
MoS_2[129]	~ 14	~ 70	4.98[326]	low energy density
$TiSe_2$[133]	108	566	5.24[327]	Mg full-cell done
WSe_2[134]	168	1578	9.39[135]	scant characterization
		Oxides		
α-MoO_3[62]	495	2332	4.71[328]	poor Mg mobility; partial irreversibility
$Mo_{2.48}VO_{9.93}$[159]	587.5	2344	3.99[329]	rapid capacity fade
$Mg_2Mo_3O_8$[160]	–	–	5.38[330]	no electrochemical activity
orthorhombic-V_2O_5[62]	352.5	1188.5	3.37[331]	α is poor; δ is promising
Xerogel-V_2O_5[195,200]	264–840	724–2303	2.74[188]	solvent cointercalation
α-MnO_2[218]	790	3324	4.21[332]	conversion reactions
δ-MnO_2[147,227]	420–690	1417–2329	3.37[333]	solvent cointercalation
λ-MnO_2[236]	551	2267	4.25[80]	poor nonaq. electrochemistry
RuO_2[53]	678	4787	7.06[334]	no characterization
		Polyanions		
$FeSiO_4$[273]	825	2420.5	2.93[335]	possible side-reactions
$MnSiO_4$[275]	384	1104	2.87[336]	side reactions
$CoSiO_4$[285]	256	779	3.04[337]	side reactions
$FePO_4$[287]	22	76	3.44[338]	surface particles amorphization
$FePO_4F$[305]	99	295	2.99[339]	poor coulombic efficiency
Ti-NASICON[294]	~136	~406	2.98[340]	poor Mg mobility
V-NASICON[298]	591	1763	2.98[340]	possible side-reactions
V/Fe-borates[312]	–	–	3.70[312]	no electrochemical activity
$Ni(CN)_6{\cdot}nH_2O$ (PB)[271]	~102	~171	1.68[84]	low energy density

[a]The status column indicates any open questions or challenges remaining for the respective structures. Practical gravimetric and volumetric energy densities are in Wh/kg and Wh/l, respectively, and the density ρ is g/cm^3. Refer to Table 1 for more details on MnO_2 polymorphs.

most PB frameworks suggest that while PB can demonstrate a proof-of-concept intercalation of several MV ions, it is not a practical candidate for a MV battery cathode.

7. DISCUSSION

Multivalent batteries that couple a high voltage cathode with a metal anode, exhibit promise in achieving higher energy densities than current Li-ion technologies. Cell-level models (section 2) show that a Mg battery using a Mg metal anode has the potential to achieve energy densities of ~750 Wh/l, indicating future applications in portable electronics as well as in electric vehicles and the grid. However, there are still many obstacles to be overcome in MV chemistry, such as the lack of compatible electrolytes and poor MV mobility in many compounds. While state-of-the-art MV batteries, using the Chevrel-phases as cathodes, demonstrate reversible Mg intercalation with reasonable rate performance, the voltages (~1.1 V) and capacities (~80 mAh/g) obtained are low, resulting in poor energy densities and necessitating the exploration of alternate chemistries for cathode materials. A summary of the available electrochemical data for all Mg cathodes is given in Table 3, and Figure 45 graphically characterizes a few candidate cathodes.

Chalcogenides

So far, the chalcogenide compounds have shown the best electrochemical performance as Mg cathodes. The fundamental breakthroughs of reversible Mg intercalation in Chevrel-Mo_6S_8 and other cluster compounds by Aurbach and his team[12] deliver the kind of cycle life that is comparable to today's Li-ion compounds, albeit at low energy density. As a result, many other chalcogenide hosts, such as sulfides (TiS_2, MoS_2)[121,123,129] and selenides ($TiSe_2$, WSe_2)[133,134] have been explored with mixed results. While Mg migration is expected to be sluggish in layered-TiS_2,[124] high-capacity reversible Mg intercalation has recently been demonstrated in spinel-Ti_2S_4 at reasonable rates (C/10 to C/5).[121] Against a Mg metal anode, Ti_2S_4 cycled at ~1.2 V yields a capacity of ~190 mAh/g, representing a significant improvement over the energy density of the Chevrel-phase. The performance of sulfide spinels is consistent with recent ab initio calculations[106] and indicates the importance of sulfur cathode chemistries in achieving highly reversible MV intercalation.

MoS_2 has attracted notable attention in the MV battery community owing to its importance as a 2D material,[128−130] but it is hard for MoS_2 to supersede other MV sulfide cathodes such as Mo_6S_8 and Ti_2S_4, given its low capacity and higher cost. $TiSe_2$[133] and WSe_2[134] have been explored as alternatives to sulfur compounds, with potentially better Mg (MV) mobilities at similar voltages and gravimetric capacities. The reliability of some Mg intercalation experiments in selenides is questionable, given the absence of rigorous characterization of the discharged products, and establishing some baseline experimental data in these systems is a high priority.

DOI: 10.1021/acs.chemrev.6b00614
Chem. Rev. 2017, 117, 4287−4341

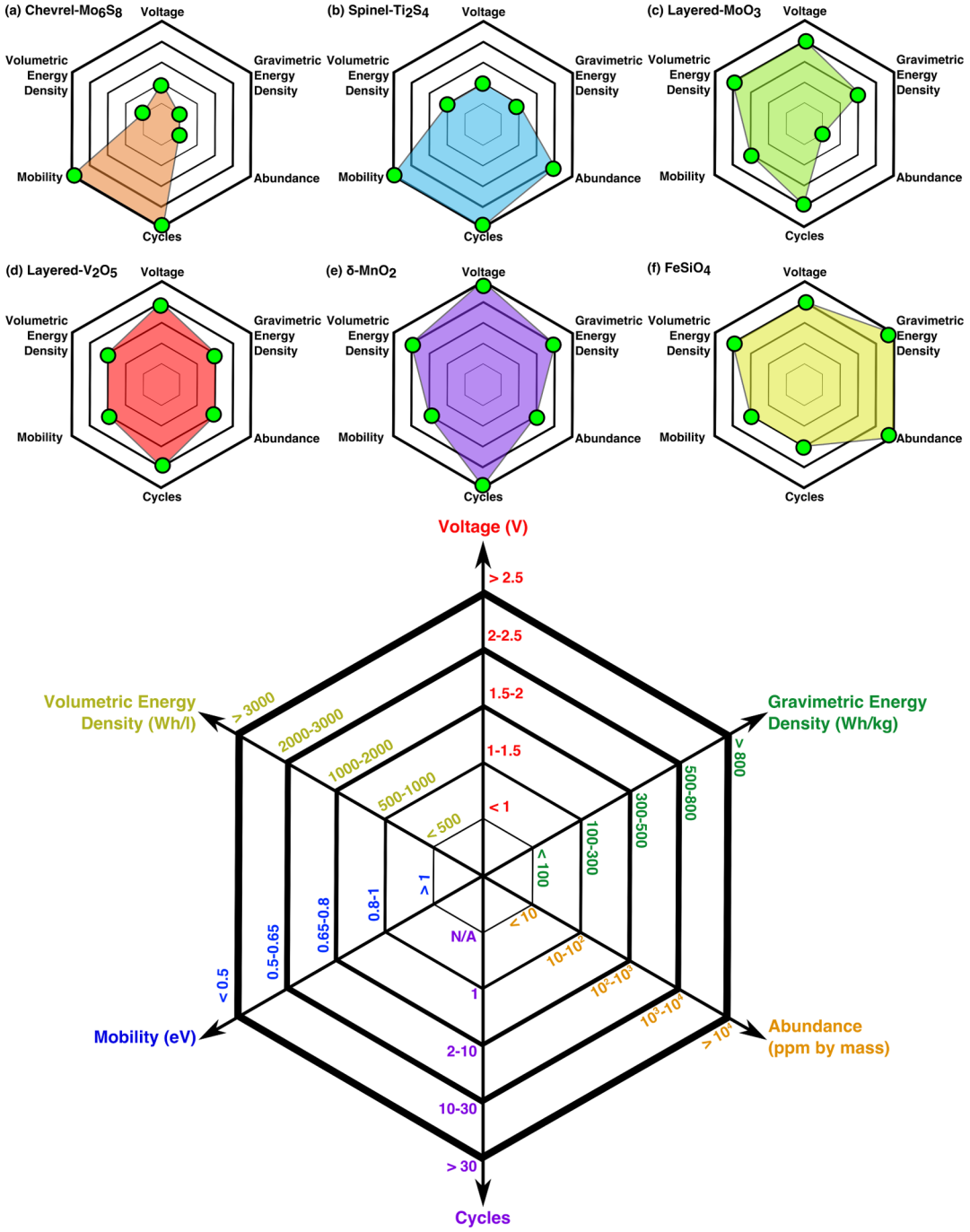

Figure 45. Parameters for charting promising cathode materials, including intercalation voltage (V), practical gravimetric (Wh/kg), volumetric (Wh/l) energy densities, barrier for bulk Mg (MV) mobility (eV), cycling behavior (number of cycles), and abundance of the transition metal used in the cathode in the earth's crust (equivalent to parts per million, or ppm, by mass, from ref 324) have been summarized for several frameworks in the chalcogenide (Chevrel and Ti_2S_4), oxide (MoO_3, V_2O_5, and MnO_2) and polyanion ($FeSiO_4$) chemical spaces.

Oxides

Transition metal oxide hosts have been considered as cathode materials for MV batteries because of their high theoretical voltages and capacities (section 5).[142,240] However, most oxide hosts suffer from poor MV mobility in the bulk structure,[142,169,170,236] possible oxide conversion reactions in the cathode,[225] pseudocapacitance contributions arising from nanosized frameworks,[143,144] and electrolyte incompatibility with high voltage (~3.0 V vs Mg) cathodes,[204] making it difficult to observe and validate reversible MV (or Mg) intercalation at reasonable rates. Nevertheless, layered-oxide hosts, such as MoO_3,[151] $Mo_{2.48}VO_{9.93}$,[159] V_2O_5,[62] and δ-MnO_2[147,227] have received significant experimental and theoretical attention as cathodes for Mg batteries, and electrochemically reversible Mg intercalation at comparable voltages has already been displayed in these hosts with varied levels of success. While oxide spinel hosts tend to have high Mg migration barriers,[142,240] recent theoretical estimations of high Mg mobility in high-pressure postspinel phases[258] shows promise and a potential new class of cathode materials.

Water (or solvent) cointercalation has often been proposed as a possible solution to improve MV (or Mg^{2+}) mobility in

DOI: 10.1021/acs.chemrev.6b00614
Chem. Rev. 2017, 117, 4287−4341

oxide hosts,[146,171] thus achieving both higher voltages and better mobilities. Despite promising electrochemical performance shown in water cointercalated hosts such as xerogel-V_2O_5[187,195,200] and MnO_2 polymorphs (especially Birnessite and Spinel),[147,227,236] further investigations are required to clarify possible side reactions (such as proton cycling) that could contribute to the improved performance. Additionally, the presence of water in the electrolyte is detrimental to the usage of a Mg metal anode and may not be viable for practical MV batteries. If solvent cointercalation is indeed established as the mechanism for improved Mg mobility in oxide hosts then exploration of other solvents that can reversibly cointercalate in addition to being compatible with the Mg anode is necessary. A fundamental question that remains to be addressed is whether solvent cointercalation improves mobility in the bulk and exactly what the mechanism is of such improvement, or whether cointercalation increases the rate capability by limiting the amount of desolvation that is required upon intercalation. If such solvent cointercalation enhances Mg mobility in the bulk, it may be possible to preintercalate the solvent in layered cathode materials.[127]

Overall, oxides will remain an exciting class of potential MV cathode materials due to their high potential energy density. Nearly two decades of research on multivalent electrochemistry have taught the battery community that divalent ions may exhibit a diverse range of behaviors from different diffusivities[12,13,21,97,142,162,170,199,205] to distinct electrochemical properties.[15,41,43,53,54,57,58] Even though MV-ion mobility is on average considerably lower than for monovalent Li^+ and Na^+ intercalants,[142] the development of a new technology is not controlled by average properties but requires only a few good material families, as evidenced by today's Li-ion technology, which relies almost solely on layered oxides (O3-stacking[325]), spinels, and the olivine $LiFePO_4$. If recent theory is a guide, it seems likely that careful matching of structure and intercalant[142,169,170,258] can indeed lead to reasonable mobility for Mg^{2+}, Ca^{2+}, or Zn^{2+}, as has already been demonstrated by very high rate reversible Zn^{2+} insertion in V_2O_5.[199]

Polyanions

As in oxides, results on polyanion cathodes are mixed. Mg intercalation in $FeSiO_4$ shows promise,[273] while possible side-reactions in others (such as Mn and Co-silicates)[275,285] have obscured whether reversible intercalation can take place.[287] Despite showing high Li- and Na-mobilities, NASICON frameworks do not seem very promising for Mg intercalation owing to the high Mg migration barriers calculated theoretically[302] and sluggish Mg migration observed in experiments.[294,297,298] Theoretical calculations on specific fluoro-polyanions show promise (e.g., Mg barrier is ~360 meV in $FeSO_4F$),[306] but experiments in the $FePO_4F$ structure suffer from poor Coulombic efficiencies and low capacities.[305] While interesting diffusion mechanisms have been observed in borates, with potential applications in other frameworks,[312] the obtained capacities are low (~50% of theoretical capacity) even at high temperatures. Prussian blue analogues, being able to intercalate a diverse set of MV species (including electrochemically unexplored Sr^{2+} and Ba^{2+}),[271,272] are interesting proof-of-concept structures, albeit with low energy densities.[318] Although Prussian blue structures may not find potential battery applications, their stability and reversibility makes them interesting counter and reference electrodes in a research setting. In summary, among the class of polyanion materials, certain silicates ($FeSiO_4$) and fluoro-polyanions ($FeSO_4F$) show potential but require rigorous experimental and theoretical investigations to validate Mg intercalation and understand any potential limitations.

While MV batteries show great promise as a means to move beyond and out-perform Li-ion batteries, a number of practical issues and open challenges must be addressed on the path to technological utilization. There is a significant lack of understanding on the complex reactions that may take place between electrolytes, electrodes, current collectors, and all other components, often leading to unidentified corrosion reactions in experiments, which obscures true MV-ion intercalation response. This is unlike for Li^+-ion or Na^+-ion chemistries which are considerably more standardized and therefore allows for more reliable and effective cathode research. Hence, it is often challenging to determine if reported electrochemical data in the literature (without supporting characterization information) indeed corresponds to reversible MV intercalation only. Overemphasizing the electrochemical observations (e.g., gravimetric capacity, open circuit voltage, rate performance, etc.) appears to be a common trend in "novel" MV cathode studies, whereas spectroscopic characterization of the intercalation process is often overlooked. Hence, rigorous characterization measurements, such as XRD, XANES, TEM, and other techniques, are required at different states of (dis)charge to truly validate MV insertion. Additionally, theoretical data, if available, can be used to benchmark experimental results and identify any possible discrepancies. In this context, ab initio theory has been particularly good at predicting electrochemical voltages within a ~0.25 V window,[341] and very large discrepancies between measured and calculated voltages should be a cause of concern. In particular, voltages in the 1.0−1.5 V range for 3d-oxides, which are generally expected to be much higher in voltage, are often a sign of corrosion currents. The recently released MV-voltage data on the Materials Project,[149] as part of the Joint Center for Energy Storage Research (JCESR) effort, may be useful in this regard.

Another common occurrence across MV cathode studies is the significant variance of electrochemical data with electrolyte species. The small stability window of most MV electrolytes necessitates special electrochemical setups, such as hybrid cells and three-electrode setups, for testing high voltage cathodes. The Li-ion and Na-ion battery communities benefit from standardized and consistent protocols, developed over the years, for testing cathode materials and electrolyte stability. The MV-ion battery field is in urgent need of similar protocol standardization. Furthermore, a dependence of cell performance on electrolyte quantity should not be overlooked. Most laboratory-scale experiments are performed in conditions of considerable electrolyte excess (flooding cell setup), while commercial battery cells strive to minimize this quantity for reasons of energy density, safety and cost. Any viable MV electrolyte/cathode combination should also be verified as functioning well with limited quantities of electrolyte.

In summary, we would like to provide a number guidelines for the field in terms of best practices and important fundamental issues to focus on: (1) The role of H_2O in MV-ion intercalation needs to be better understood, especially given that a few cathodes, such as V_2O_5, MnO_2, etc., exhibit significantly different electrochemical responses with (or without) an aqueous electrolyte. While multiple experiments have demonstrated that the presence of H_2O in the electrolyte

DOI: 10.1021/acs.chemrev.6b00614
Chem. Rev. 2017, 117, 4287−4341

and/or electrode material improves MV-ion intercalation, the mechanism by which this occurs is unclear. It is possible that H_2O in the cathode improves MV-ion mobility, either by propping open the layered structures,[127] or by providing pathways with low coordination change for the MV-ion.[142] It may also be possible that H_2O moves with the MV ions in the structure and assists with desolvation from the electrolyte. In this regard, the role of H_2O in generating cyclable protons, which can inflate the electrochemical properties observed, should not be overlooked. Understanding how H_2O improves intercalation, which might require concerted theoretical-experimental studies, is critical so that one can target other cointercalants with a less detrimental effect on the metallic anode. (2) For Mg^{2+} and Ca^{2+}, conversion reactions are competitive with intercalation for many potential cathode materials. In addition, the corrosive nature of some electrolytes can lead to corrosion currents overwhelming the response from the cathode. Hence, at this early stage of the field, when no standard electrolytes and cell designs are available, electrochemical characterization of cathode materials should always be accompanied by structural characterization of the cycled cathode materials to demonstrate that intercalation is indeed taking place. (3) The field would benefit tremendously from establishing some baseline cathode materials that can be used across laboratories. Even for well-studied materials such as MnO_2, MoO_3, and V_2O_5, electrochemical results vary greatly in the literature and currently no "ground truth" capacity is known for these materials, unlike what is the case for many current Li-ion cathode materials. (4) Given the complex electrochemistry occurring in MV cells, and the passivation of Mg metal with many electrolytes, alternatives to standard two-electrode full cells should be encouraged. For example, by using hybrid cells with a reference electrode, more electrolyte choices become available to test cathodes, and a more rigorous electrochemical response of the cathode can be obtained. In this regard, the development of good reference electrolytes for MV systems represents a high priority. It is worth nothing that the electrochemistry of several MV cathode materials is often tested at elevated temperatures to facilitate MV ion mobility (as suggested by Figure 12). Hence, the electrochemical results always necessitate careful interpretation as temperature can promote undesired side reactions (including phase transformations) that contribute to the overall degradation of the cathode. (5) The result of new investigations should be compared and contrasted to previously published work and to available theory predictions. In preparing this review, we often found that the result of multiple studies could not be consistent with each other. Indications that intercalation is implausible can sometimes be inferred by comparing to ab initio predicted properties, in particular for average voltages, diffusion barriers, and changes of lattice parameters with intercalation, which have become quite reliable in ab initio methods. While disagreement with such theoretical predictions does not necessarily imply that either theory or experiments are wrong, it usually does indicate that a more complex phenomenon than topotatic intercalation (typically assumed for first-principles results) is taking place. Hence, such "disagreements" should be taken as a caution and a starting point for further investigations.

8. FUTURE OUTLOOK

The ability to store electricity in chemical devices represents one of the most successful discoveries of the recent centuries, and the last 30 years have witnessed a swift expansion of this field dominated mainly by Pb-acid, Ni-Metal hydride, and now lithium ion batteries. The latter form the bedrock of millions of portable devices (laptops, cameras, and various other tools). As Li-ion batteries approach their energy density limit, new technologies will be required to meet the rapidly growing demands of grid-scale and portable electrochemical energy storage. Utilizing intercalation batteries based on multivalent chemistry represents a promising avenue in this regard, with significant gains in energy density enabled by MV metal anodes, which are less susceptible to dendrite growth than Li at practical cycling rates, and are potentially safer and cheaper.

We have reviewed the progress and challenges associated with MV cathodes, the discovery of which remains one of the chief obstacles to a high energy-density MV battery prototype. Contrary to the well-established Li-ion intercalation experiments, the absence of minimal standard protocols to routinely perform electrochemical intercalation experiments poses substantial roadblocks for developing practical multivalent cathode materials. Cathode improvements over the last 15 years have resulted in significant increases in MV full-cell energy density, with spinel Ti_2S_4 doubling the energy density of Chevrel Mo_6S_8.

As the state-of-the-art thiospinel MV cathode material falls short of energy density levels needed to compete with present Li-ion technology, there is a demonstrable need for the discovery of high energy-density cathodes. Oxides provide a clear path to improved energy density at the expense of MV mobility. Experimental results to date in both material classes suggest that high voltage cathodes can be developed, albeit with MV mobility remaining a significant obstacle. Fortunately, the vast chemical space of possible MV cathode materials remains largely unexplored,[73] and predictions of high mobility in new material classes such as postspinels, silicates, and fluoro-polyanions suggest that a covenant of peace between the two contending parties, kinetic performance and energy density, can be simultaneously attained.

AUTHOR INFORMATION

Corresponding Authors

*E-mail: pcanepa@lbl.gov.
*E-mail: gceder@berkeley.edu and gceder@lbl.gov.

ORCID

Pieremanuele Canepa: 0000-0002-5168-9253

Author Contributions

[@]P.C., G.S.G., and D.C.H. contributed equally to this work.

Notes

The authors declare no competing financial interest.

Biographies

Pieremanuele Canepa is a Ramsay Memorial fellow at the University of Bath, United Kingdom, and was a postdoctoral fellow at Lawrence Berkeley National Laboratory and the Massachusetts Institute of Technology (MIT) under Prof. Gerbrand Ceder. His research covers the assessment of materials as novel electrode and solid ionic conductors for intercalation batteries as well as the rationalization of the complex structure of liquid electrolytes. In November 2012, he was awarded a Ph.D. in Chemistry from the University of Kent, United Kingdom. He holds a M.Sc. (Hons) and B.Sc. (Hons) in Chemistry from the University of Turin, Italy.

Gopalakrishnan Sai Gautam is a Ph.D. student at the Department of Materials Science and Engineering, Massachusetts Institute of

DOI: 10.1021/acs.chemrev.6b00614
Chem. Rev. 2017, 117, 4287−4341

Technology (MIT), under the guidance of Prof. Gerbrand Ceder. Currently a graduate exchange student at UC Berkeley, he focuses on in-depth studies of multivalent cathode materials and solid electrolytes using theoretical techniques while also contributing to high-throughput searches for promising candidates. He holds a Dual Degree (M.Tech. & B.Tech.) in Metallurgical and Materials Engineering from the Indian Institute of Technology Madras.

Daniel C. Hannah is a postdoctoral fellow at Lawrence Berkeley National Laboratory in the Materials Sciences Division working in the group of Prof. Gerbrand Ceder. His current research focuses on computational discovery and evaluation of cathode materials for multivalent batteries. He obtained his Ph.D. in Physical Chemistry at Northwestern University under the supervision of Profs. George Schatz and Richard Schaller, where he researched optical and thermal processes in nanomaterials. He holds a B.S. in Chemistry from Ohio State University.

Rahul Malik obtained a Ph.D. in 2013 under the supervision of Prof. Gerbrand Ceder at the Massachusetts Institute of Technology (MIT), where he worked on characterizing the Li intercalation kinetics in $LiFePO_4$ electrodes using first-principles calculations. From 2014 to 2015, he researched multivalent, Na-ion, and Li-excess intercalation cathode materials for batteries as a postdoctoral and research associate at MIT with Prof. Ceder. Currently, he is working as a consulting scientist for an early stage technology start-up.

Miao Liu received his Ph.D. in Materials Science and Engineering from the University of Utah. He is currently a postdoctoral fellow working with Prof. Kristin Persson in the Applied Energy Materials Group at the Lawrence Berkeley National Laboratory. He seeks to accelerate the discovery of new energy-storage materials using high-throughput first-principles calculations. His interest also extends to low-dimensional nanostructures.

Kevin G. Gallagher is the Principle Investigator for Systems Analysis and Translation in the Joint Center for Energy Storage Research (the DOE-BES Battery and Energy Storage Innovation Hub) and an electrochemical engineer at Argonne National Laboratory. His work has focused on techno-economic and continuum-scale modeling, electrochemical characterization, and materials development in advanced and beyond lithium-ion systems. He is a cocreator of the freely available bottom-up Battery Performance and Cost model (BatPaC) that has been used to support the 2017−2025 GHG and CAFE regulations for light duty vehicles. He received his Ph.D. in Chemical & Biomolecular Engineering from the Georgia Institute of Technology in 2009 and his B.S. in Chemical Engineering from the University of Michigan in 2003. In between undergraduate and graduate school, Kevin was a process engineer at a leading consumer products company.

Kristin A. Persson is an Assistant Professor of Materials Sciences and Engineering at UC Berkeley and Faculty Staff Scientist at Lawrence Berkeley National Laboratory. She received a Master's degree in Engineering Physics from the Lund Institute of Technology in Sweden and a Ph.D. in Theoretical Physics from the Royal Institute of Technology in Stockholm, Sweden. Kristin holds several patents and has published more than 100 scientific papers. She is an Associate Editor of Chemistry of Materials and has garnered awards, most recently, the TMS 2017 Early Career Faculty Fellow Award. Persson's research focuses on accelerated materials design using first-principles computations, and in this capacity she directs the Materials Project, which is a multi-institution, multinational effort to compute the properties of all inorganic materials and provide the data and associated analysis algorithms free of charge.

Gerbrand Ceder is The Chancellor's Professor of Materials Science and Engineering at UC Berkeley. He received an engineering degree from the University of Leuven, Belgium, and a Ph.D. in Materials Science from UC Berkeley in 1991. His research interests lie in materials design for clean energy technology. He has published over 375 scientific papers, and holds several U.S. patents. He has served on several DOE committees, including the workgroup preparing the Basic Needs for Electrical Energy Storage report, and has advised the government's Office of Science and Technology Policy on the role of computation in materials development, leading to the Materials Genome Initiative. He is a Lead Scientist for new battery technologies at the Joint Center for Energy Storage (JCESR) of the US Department of Energy, and the Chief Scientist of the Energy Frontier Research Center at the National Renewable Energy Laboratory. He is a Fellow of the Materials Research Society and a member of the Royal Flemish Academy of Arts and Sciences. He has received several awards including the Materials Theory Award from MRS, the MRS Medal, the Morris Cohen Award and the Hardy Award from TMS, the Battery Research Award from the ECS, and the research award from the International Battery Association. He is a co-founder of Computational Modeling Consultants, Pellion Technologies, and The Materials Project.

ACKNOWLEDGMENTS

The current work is fully supported by the Joint Center for Energy Storage Research, an Energy Innovation Hub funded by the U.S. Department of Energy (DOE), Office of Science and Basic Energy Sciences. This study was supported by Subcontract 3F-31144. The authors acknowledge a careful reading of the manuscript with Prof. Doron Aurbach at Bar-Ilan University, Prof. Jordi Cabana at University of Illinois Chicago, as well as Xiaoqi Sun and Prof. Linda Nazar at the University of Waterloo. P.C., G.S.G., and D.C.H. are thankful to Dr. Shou-Hang Bo and Tina Chen at Lawrence Berkeley National Laboratory for fruitful discussion as well as the "nice and clean" suggestions by Dr. Ryan Bayliss at University of Illinois at Chicago.

ACRONYMS

ABF-STEM	annular bright field scanning electron transmission microscopy
ACN	acetonitrile
AES	atomic emission spectroscopy
APC	all phenyl complex
BatPac	battery performance and cost
BVS	bond valence sum
CE	coulombic efficiency
CNT	carbon nanotube
CV	cyclic voltammetry
DC	direct current
DCC	dichloro complex
DEC	diethyl carbonate
DMC	dimethyl carbonate
DOE	department of energy
DOS	density of states
DFT	density functional theory
EC	ethylene carbonate
EELS	electron energy loss spectroscopy
EMIC	1-ethyl-3-methylimidazolium chloride
EDS	energy-dispersive X-ray spectroscopy
EDAX	energy-dispersive analysis of X-rays
EV	electric vehicles

DOI: 10.1021/acs.chemrev.6b00614
Chem. Rev. 2017, 117, 4287−4341

EXAFS	extended X-ray absorption fine structure
FTIR	Fourier transform infrared spectroscopy
GITT	galvanostatic intermittent titration technique
HAADF	high-angle annular dark-field imaging
HRTEM	high-resolution transmission electron microscopy
ICP	inductively coupled plasma
ICSD	inorganic crystal structure database
MACC	magnesium aluminum chloride complex
MMC	Mg monocarborane
MV	multivalent
NASICON	Na super ionic conductor
NEB	nudged elastic band
NMC333	$LiNi_{1/3}Mn_{1/3}Co_{1/3}O_2$
NMR	nuclear magnetic resonance
OCV	open circuit voltage
OEM	original equipment manufacturer
OES	optical emission spectroscopy
PB	Prussian blue
PC	propylene carbonate
PDF	pair distribution function
PEO	poly-ethylene oxide
PITT	potentiodynamic intermittent titration technique
PPM	parts per million
SAXS	small-angle X-ray scattering
STEM	scanning transmission electron microscopy
SCE	saturated calomel electrode
SHE	standard hydrogen electrode
TEM	transmission electron microscopy
TFSA	bis(trifluoromethanesulfonyl)amide
TFSI	bis(trifluoromethane)sulfonimide
TGA	thermogravimetric analysis
THF	tetrahydrofuran
TM	transition metal
USABC	United States Advanced Battery Consortium
WAXS	wide-angle X-ray scattering
XANES	X-ray absorption near edge spectroscopy
XAS	X-ray absorption spectroscopy
XRD	X-ray diffraction
XRF	X-ray fluorescence
XPS	X-ray photoelectron spectroscopy

REFERENCES

(1) Nykvist, B.; Nilsson, M. Rapidly falling costs of battery packs for electric vehicles. *Nat. Clim. Change* **2015**, *5*, 329−332.

(2) Diouf, B.; Pode, R. Potential of lithium-ion batteries in renewable energy. *Renewable Energy* **2015**, *76*, 375−380.

(3) Whittingham, M. S. Ultimate Limits to Intercalation Reactions for Lithium Batteries. *Chem. Rev.* **2014**, *114*, 11414−11443.

(4) Andre, D.; Kim, S.-J.; Lamp, P.; Lux, S. F.; Maglia, F.; Paschos, O.; Stiaszny, B. Future generations of cathode materials: an automotive industry perspective. *J. Mater. Chem. A* **2015**, *3*, 6709−6732.

(5) Thackeray, M. M.; Wolverton, C.; Isaacs, E. D. Electrical energy storage for transportation-approaching the limits of, and going beyond, lithium-ion batteries. *Energy Environ. Sci.* **2012**, *5*, 7854−7863.

(6) Grey, C. P.; Tarascon, J. M. Sustainability and in situ monitoring in battery development. *Nat. Mater.* **2016**, *16*, 45−56.

(7) Peled, E.; Gorenshtein, A.; Segal, M.; Sternberg, Y. Rechargeable lithium-sulfur battery (extended abstract). *J. Power Sources* **1989**, *26*, 269−271.

(8) Yang, Z.; Zhang, J.; Kintner-Meyer, M. C. W.; Lu, X.; Choi, D.; Lemmon, J. P.; Liu, J. Electrochemical Energy Storage for Green Grid. *Chem. Rev.* **2011**, *111*, 3577−3613.

(9) Bruce, P. G.; Freunberger, S. A.; Hardwick, L. J.; Tarascon, J.-M. Li-O_2 and Li-S batteries with high energy storage. *Nat. Mater.* **2011**, *11*, 19−29.

(10) Nazar, L. F.; Cuisinier, M.; Pang, Q. Lithium-sulfur batteries. *MRS Bull.* **2014**, *39*, 436−442.

(11) Manthiram, A.; Fu, Y.; Chung, S.-H.; Zu, C.; Su, Y.-S. Rechargeable Lithium-Sulfur Batteries. *Chem. Rev.* **2014**, *114*, 11751−11787.

(12) Aurbach, D.; Lu, Z.; Schechter, A.; Gofer, Y.; Gizbar, H.; Turgeman, R.; Cohen, Y.; Moshkovich, M.; Levi, E. Prototype systems for rechargeable magnesium batteries. *Nature* **2000**, *407*, 724−727.

(13) Yoo, H. D.; Shterenberg, I.; Gofer, Y.; Gershinsky, G.; Pour, N.; Aurbach, D. Mg rechargeable batteries: an on-going challenge. *Energy Environ. Sci.* **2013**, *6*, 2265−2279.

(14) Besenhard, J. O.; Winter, M. Advances in Battery Technology: Rechargeable Magnesium Batteries and Novel Negative-Electrode Materials for Lithium Ion Batteries. *ChemPhysChem* **2002**, *3*, 155−159.

(15) Ponrouch, A.; Frontera, C.; Bardé, F.; Palacín, M. R. Towards a calcium-based rechargeable battery. *Nat. Mater.* **2015**, *15*, 169−172.

(16) Aurbach, D. Review of selected electrode-solution interactions which determine the performance of Li and Li ion batteries. *J. Power Sources* **2000**, *89*, 206−218.

(17) Aurbach, D.; Zinigrad, E.; Cohen, Y.; Teller, H. A short review of failure mechanisms of lithium metal and lithiated graphite anodes in liquid electrolyte solutions. *Solid State Ionics* **2002**, *148*, 405−416.

(18) Larcher, D.; Beattie, S.; Morcrette, M.; Edström, K.; Jumas, J.-C.; Tarascon, J.-M. Recent findings and prospects in the field of pure metals as negative electrodes for Li-ion batteries. *J. Mater. Chem.* **2007**, *17*, 3759−3772.

(19) Dahn, J. http://www.almaden.ibm.com/institute/2009/resources/2009/presentations/JeffDahn-AlmadenInstitute2009.pdf (accessed March 15, 2016).

(20) Pour, N.; Gofer, Y.; Major, D. T.; Aurbach, D. Structural analysis of electrolyte solutions for rechargeable Mg batteries by stereoscopic means and DFT calculations. *J. Am. Chem. Soc.* **2011**, *133*, 6270−6278.

(21) Aurbach, D.; Suresh, G. S.; Levi, E.; Mitelman, A.; Mizrahi, O.; Chusid, O.; Brunelli, M. Progress in Rechargeable Magnesium Battery Technology. *Adv. Mater.* **2007**, *19*, 4260−4267.

(22) Aurbach, D.; Gizbar, H.; Schechter, A.; Chusid, O.; Gottlieb, H. E.; Gofer, Y.; Goldberg, I. Electrolyte Solutions with a Wide Electrochemical Window for Rechargeable Magnesium Batteries. *J. Electrochem. Soc.* **2002**, *149*, A115−A121.

(23) Kim, H. S.; Arthur, T. S.; Allred, G. D.; Zajicek, J.; Newman, J. G.; Rodnyansky, A. E.; Oliver, A. G.; Boggess, W. C.; Muldoon, J. Structure and compatibility of a magnesium electrolyte with a sulphur cathode. *Nat. Commun.* **2011**, *2*, 427.

(24) Muldoon, J.; Bucur, C. B.; Oliver, A. G.; Sugimoto, T.; Matsui, M.; Kim, H. S.; Allred, G. D.; Zajicek, J.; Kotani, Y. Electrolyte roadblocks to a magnesium rechargeable battery. *Energy Environ. Sci.* **2012**, *5*, 5941−5950.

(25) Guo, Y.-S.; Zhang, F.; Yang, J.; Wang, F.-F.; NuLi, Y.; Hirano, S.-i. Boron-based electrolyte solutions with wide electrochemical windows for rechargeable magnesium batteries. *Energy Environ. Sci.* **2012**, *5*, 9100−9106.

(26) Guo, Y.-S.; Zhang, F.; Yang, J.; Wang, F.-F. Electrochemical performance of novel electrolyte solutions based on organoboron magnesium salts. *Electrochem. Commun.* **2012**, *18*, 24−27.

(27) Doe, R. E.; Han, R.; Hwang, J.; Gmitter, A. J.; Shterenberg, I.; Yoo, H. D.; Pour, N.; Aurbach, D. Novel, electrolyte solutions comprising fully inorganic salts with high anodic stability for rechargeable magnesium batteries. *Chem. Commun.* **2014**, *50*, 243−245.

(28) Liu, T.; Shao, Y.; Li, G.; Gu, M.; Hu, J.; Xu, S.; Nie, Z.; Chen, X.; Wang, C.; Liu, J. A facile approach using $MgCl_2$ to formulate high performance Mg^{2+} electrolytes for rechargeable Mg batteries. *J. Mater. Chem. A* **2014**, *2*, 3430−3438.

(29) Barile, C. J.; Barile, E. C.; Zavadil, K. R.; Nuzzo, R. G.; Gewirth, A. A. Electrolytic Conditioning of a Magnesium Aluminum Chloride

DOI: 10.1021/acs.chemrev.6b00614
Chem. Rev. 2017, 117, 4287−4341

Complex for Reversible Magnesium Deposition. *J. Phys. Chem. C* **2014**, *118*, 27623−27630.
(30) Barile, C. J.; Spatney, R.; Zavadil, K. R.; Gewirth, A. A. Investigating the Reversibility of in Situ Generated Magnesium Organohaloaluminates for Magnesium Deposition and Dissolution. *J. Phys. Chem. C* **2014**, *118*, 10694−10699.
(31) Canepa, P.; Gautam, G. S.; Malik, R.; Jayaraman, S.; Rong, Z.; Zavadil, K. R.; Persson, K.; Ceder, G. Understanding the Initial Stages of Reversible Mg Deposition and Stripping in Inorganic Nonaqueous Electrolytes. *Chem. Mater.* **2015**, *27*, 3317−3325.
(32) Canepa, P.; Jayaraman, S.; Cheng, L.; Rajput, N.; Richards, W. D.; Gautam, G. S.; Curtiss, L. A.; Persson, K.; Ceder, G. Elucidating the Structure of the Magnesium Aluminum Chloride Complex electrolyte for Magnesium-ion batteries. *Energy Environ. Sci.* **2015**, *8*, 3718−3730.
(33) See, K. A.; Chapman, K. W.; Zhu, L.; Wiaderek, K. M.; Borkiewicz, O. J.; Barile, C. J.; Chupas, P. J.; Gewirth, A. A. The Interplay of Al and Mg Speciation in Advanced Mg Battery Electrolyte Solutions. *J. Am. Chem. Soc.* **2016**, *138*, 328−337.
(34) Carter, T. J.; Mohtadi, R.; Arthur, T. S.; Mizuno, F.; Zhang, R.; Shirai, S.; Kampf, J. W. Boron Clusters as Highly Stable Magnesium-Battery Electrolytes. *Angew. Chem., Int. Ed.* **2014**, *53*, 3173−3177.
(35) Tutusaus, O.; Mohtadi, R.; Arthur, T. S.; Mizuno, F.; Nelson, E. G.; Sevryugina, Y. V. An Efficient Halogen-Free Electrolyte for Use in Rechargeable Magnesium Batteries. *Angew. Chem., Int. Ed.* **2015**, *54*, 7900−7904.
(36) Lapidus, S. H.; Rajput, N. N.; Qu, X.; Chapman, K. W.; Persson, K. A.; Chupas, P. J. Solvation structure and energetics of electrolytes for multivalent energy storage. *Phys. Chem. Chem. Phys.* **2014**, *16*, 21941−21945.
(37) Shterenberg, I.; Salama, M.; Yoo, H. D.; Gofer, Y.; Park, J.-B.; Sun, Y.-K.; Aurbach, D. Evaluation of $(CF_3SO_2)_2N^-$(TFSI) Based Electrolyte Solutions for Mg Batteries. *J. Electrochem. Soc.* **2015**, *162*, A7118−A7128.
(38) Rajput, N. N.; Qu, X.; Sa, N.; Burrell, A. K.; Persson, K. A. The Coupling between Stability and Ion Pair Formation in Magnesium Electrolytes from First-Principles Quantum Mechanics and Classical Molecular Dynamics. *J. Am. Chem. Soc.* **2015**, *137*, 3411−3420.
(39) Song, J.; Sahadeo, E.; Noked, M.; Lee, S. B. Mapping the Challenges of Magnesium Battery. *J. Phys. Chem. Lett.* **2016**, *7*, 1736−1749.
(40) Lipson, A. L.; Han, S.-D.; Pan, B.; See, K. A.; Gewirth, A. A.; Liao, C.; Vaughey, J. T.; Ingram, B. J. Practical Stability Limits of Magnesium Electrolytes. *J. Electrochem. Soc.* **2016**, *163*, A2253−A2257.
(41) Muldoon, J.; Bucur, C. B.; Oliver, A. G.; Zajicek, J.; Allred, G. D.; Boggess, W. C. Corrosion of magnesium electrolytes: chlorides − the culprit. *Energy Environ. Sci.* **2013**, *6*, 482−487.
(42) Mohtadi, R.; Matsui, M.; Arthur, T. S.; Hwang, S.-J. Magnesium Borohydride: From Hydrogen Storage to Magnesium Battery. *Angew. Chem., Int. Ed.* **2012**, *51*, 9780−9783.
(43) Muldoon, J.; Bucur, C. B.; Gregory, T. D. Quest for Nonaqueous multivalent Secondary batteries: Magnesium and Beyond. *Chem. Rev.* **2014**, *114*, 11683−11720.
(44) Bucur, C. B.; Gregory, T.; Oliver, A. G.; Muldoon, J. Confession of a Magnesium Battery. *J. Phys. Chem. Lett.* **2015**, *6*, 3578−3591.
(45) Bucur, C. B.; Gregory, T.; Muldoon, J. Why Grignard's Century Old Nobel Prize Should Spark Your Curiosity. *Green Energy and Technology* **2015**, 611−635.
(46) Ha, J. H.; Adams, B.; Cho, J.-H.; Duffort, V.; Kim, J. H.; Chung, K. Y.; Cho, B. W.; Nazar, L. F.; Oh, S. H. A conditioning-free magnesium chloride complex electrolyte for rechargeable magnesium batteries. *J. Mater. Chem. A* **2016**, *4*, 7160−7164.
(47) Sa, N.; Pan, B.; Saha-Shah, A.; Hubaud, A. A.; Vaughey, J. T.; Baker, L. A.; Liao, C.; Burrell, A. K. Role of Chloride for a Simple, Non-Grignard Mg Electrolyte in Ether-Based Solvents. *ACS Appl. Mater. Interfaces* **2016**, *8*, 16002−16008.
(48) Keyzer, E. N.; Glass, H. F. J.; Liu, Z.; Bayley, P. M.; Dutton, S. E.; Grey, C. P.; Wright, D. S. Mg $(PF_6)_2$-Based Electrolyte Systems: Understanding Electrolyte-Electrode Interactions for the Development of Mg-Ion Batteries. *J. Am. Chem. Soc.* **2016**, *138*, 8682−8685.
(49) Giffin, G. A. Ionic liquid-based electrolytes for "beyond lithium" battery technologies. *J. Mater. Chem. A* **2016**, *4*, 13378−13389.
(50) Salama, M.; Shterenberg, I.; Gizbar, H.; Eliaz, N. N.; Kosa, M.; Keinan-Adamsky, K.; Afri, M.; Shimon, L. J.; Gottlieb, H. E.; Major, D. T.; Gofer, Y.; Aurbach, D. Unique Behavior of Dimethoxyethane (DME)/$Mg(N(SO_2CF_3)_2)_2$ Solutions. *J. Phys. Chem. C* **2016**, *120*, 19586−19594.
(51) Tutusaus, O.; Mohtadi, R.; Singh, N.; Arthur, T. S.; Mizuno, F. Study of Electrochemical Phenomena Observed at the Mg Metal/Electrolyte Interface. *ACS Energy Lett.* **2017**, *2*, 224−229.
(52) Lu, Z.; Schechter, A.; Moshkovich, M.; Aurbach, D. On the electrochemical behavior of magnesium electrodes in polar aprotic electrolyte solutions. *J. Electroanal. Chem.* **1999**, *466*, 203−217.
(53) Gregory, T. D.; Hoffman, R. J.; Winter, M. Nonaqueous Electrochemistry of Magnesium. *J. Electrochem. Soc.* **1990**, *137*, 775−780.
(54) Aurbach, D.; Gizbar, H.; Schechter, A.; Chusid, O.; Gottlieb, H. E.; Gofer, Y.; Goldberg, I. Electrolyte Solutions for Rechargeable Magnesium Batteries Based on Organomagnesium Chloroaluminate Complexes. *J. Electrochem. Soc.* **2002**, *149*, A115−A121.
(55) Doe, R. E.; Han, R.; Gofer, Y.; Aurbach, D.; Pour, N.; Sterenberg, E. Non-Aqueous Electrolyte for Rechargeable Magnesium Ion Cell. Patent WO2013096827 A1, 2013.
(56) Shao, Y.; Liu, T.; Li, G.; Gu, M.; Nie, Z.; Engelhard, M.; Xiao, J.; Lv, D.; Wang, C.; Zhang, J.-G.; Liu, J. Coordination Chemistry in magnesium battery electrolytes: how ligands affect their performance. *Sci. Rep.* **2013**, *3*, 3130.
(57) Peled, E. The Electrochemical Behavior of Alkali and Alkaline Earth Metals in Nonaqueous Battery Systems—The Solid Electrolyte Interphase Model. *J. Electrochem. Soc.* **1979**, *126*, 2047−2051.
(58) Aurbach, D. The Electrochemical Behavior of Calcium Electrodes in a Few Organic Electrolytes. *J. Electrochem. Soc.* **1991**, *138*, 3536−3545.
(59) Wan, L. F.; Perdue, B. R.; Apblett, C. A.; Prendergast, D. Mg Desolvation and Intercalation Mechanism at the Mo_6S_8 Chevrel Phase Surface. *Chem. Mater.* **2015**, *27*, 5932−5940.
(60) Wu, F.; Zhou, H.; Bai, Y.; Wang, H.; Wu, C. Toward 5 V Li-Ion Batteries: Quantum Chemical Calculation and Electrochemical Characterization of Sulfone-Based High-Voltage Electrolytes. *ACS Appl. Mater. Interfaces* **2015**, *7*, 15098−15107.
(61) Terada, S.; Mandai, T.; Suzuki, S.; Tsuzuki, S.; Watanabe, K.; Kamei, Y.; Ueno, K.; Dokko, K.; Watanabe, M. Thermal and Electrochemical Stability of Tetraglyme-Magnesium Bis-(trifluoromethanesulfonyl)amide Complex: Electric Field Effect of Divalent Cation on Solvate Stability. *J. Phys. Chem. C* **2016**, *120*, 1353−1365.
(62) Gershinsky, G.; Yoo, H. D.; Gofer, Y.; Aurbach, D. Electrochemical and Spectroscopic Analysis of Mg^{2+} Intercalation into Thin Film Electrodes of Layered Oxides: V_2O_5 and MoO_3. *Langmuir* **2013**, *29*, 10964−10972.
(63) Baskin, A.; Prendergast, D. Exploration of the Detailed Conditions for Reductive Stability of $Mg(TFSI)_2$ in Diglyme: Implications for Multivalent Electrolytes. *J. Phys. Chem. C* **2016**, *120*, 3583−3594.
(64) Connell, J. G.; Genorio, B.; Lopes, P. P.; Strmcnik, D.; Stamenkovic, V. R.; Markovic, N. M. Tuning the Reversibility of Mg Anodes via Controlled Surface Passivation by H_2O/Cl^- in Organic Electrolytes. *Chem. Mater.* **2016**, *28*, 8268−8277.
(65) Sa, N.; Rajput, N. N.; Wang, H.; Key, B.; Ferrandon, M.; Srinivasan, V.; Persson, K. A.; Burrell, A. K.; Vaughey, J. T. Concentration dependent electrochemical properties and structural analysis of a simple magnesium electrolyte: magnesium bis-(trifluoromethane sulfonyl)imide in diglyme. *RSC Adv.* **2016**, *6*, 113663−113670.
(66) Kumar, N.; Siegel, D. J. Interface-Induced Renormalization of Electrolyte Energy Levels in Magnesium Batteries. *J. Phys. Chem. Lett.* **2016**, *7*, 874−881.

DOI: 10.1021/acs.chemrev.6b00614
Chem. Rev. 2017, 117, 4287−4341

(67) Watkins, T.; Kumar, A.; Buttry, D. A. Designer Ionic Liquids for Reversible Electrochemical Deposition/Dissolution of Magnesium. *J. Am. Chem. Soc.* **2016**, *138*, 641−650.
(68) Saha, P.; Datta, M. K.; Velikokhatnyi, O. I.; Manivannan, A.; Alman, D.; Kumta, P. N. Rechargeable magnesium battery: Current status and key challenges for the future. *Prog. Mater. Sci.* **2014**, *66*, 1−86.
(69) Huie, M. M.; Bock, D. C.; Takeuchi, E. S.; Marschilok, A. C.; Takeuchi, K. J. Cathode materials for magnesium and magnesium-ion based batteries. *Coord. Chem. Rev.* **2015**, *287*, 15−27.
(70) Park, M.-S.; Kim, J.-G.; Kim, Y.-J.; Choi, N.-S.; Kim, J.-S. Recent Advances in Rechargeable Magnesium Battery Technology: A Review of the Field's Current Status and Prospects. *Isr. J. Chem.* **2015**, *55*, 570−585.
(71) Shterenberg, I.; Salama, M.; Gofer, Y.; Levi, E.; Aurbach, D. The Challenge of Developing Rechargeable Magnesium Batteries. *MRS Bull.* **2014**, *39*, 453−460.
(72) Levi, E.; Levi, M. D.; Chasid, O.; Aurbach, D. A review on the problems of the solid state ions diffusion in cathodes for rechargeable Mg batteries. *J. Electroceram.* **2009**, *22*, 13−19.
(73) Crabtree, G. The joint center for energy storage research: A new paradigm for battery research and development. *AIP Conf. Proc.* **2014**, *1652*, 112−128.
(74) Gallagher, K. G.; Trask, S. E.; Bauer, C.; Woehrle, T.; Lux, S. F.; Tschech, M.; Lamp, P.; Polzin, B. J.; Ha, S.; Long, B.; Wu, Q.; Lu, W.; Dees, D. W.; Jansen, A. N. Optimizing Areal Capacities through Understanding the Limitations of Lithium-Ion Electrodes. *J. Electrochem. Soc.* **2016**, *163*, A138−A149.
(75) Gallagher, K. G.; Goebel, S.; Greszler, T.; Mathias, M.; Oelerich, W.; Eroglu, D.; Srinivasan, V. Quantifying the promise of lithium-air batteries for electric vehicles. *Energy Environ. Sci.* **2014**, *7*, 1555−1563.
(76) Eroglu, D.; Ha, S.; Gallagher, K. G. Fraction of the theoretical specific energy achieved on pack level for hypothetical battery chemistries. *J. Power Sources* **2014**, *267*, 14−19.
(77) Nelson, P. A.; Gallagher, K. G.; Bloom, I.; Dees, D. *Modeling the Performance and Cost of Lithium-Ion Batteries for Electric-Drive Vehicles*; Technical Report ANL-11/32; Argonne National Laboratory: Argonne, IL, September 2011, http://www.ipd.anl.gov/anlpubs/2011/10/71302.pdf, 2012.
(78) Gallagher, K. G.; Nelson, P. A.; Dees, D. W. Simplified calculation of the area specific impedance for battery design. *J. Power Sources* **2011**, *196*, 2289−2297.
(79) Berg, E. J.; Villevieille, C.; Streich, D.; Trabesinger, S.; Novák, P. Rechargeable Batteries: Grasping for the Limits of Chemistry. *J. Electrochem. Soc.* **2015**, *162*, A2468−A2475.
(80) Berg, H.; Thomas, J. O.; Liu, W.; Farrington, G. C. A neutron diffraction study of Ni substituted $LiMn_2O_4$. *Solid State Ionics* **1998**, *112*, 165−168.
(81) Neubauer, J.; Pesaran, A.; Bae, C.; Elder, R.; Cunningham, B. Updating United States Advanced Battery Consortium and Department of Energy battery technology targets for battery electric vehicles. *J. Power Sources* **2014**, *271*, 614−621.
(82) Christensen, J.; Albertus, P.; Sanchez-Carrera, R. S.; Lohmann, T.; Kozinsky, B.; Liedtke, R.; Ahmed, J.; Kojic, A. A Critical Review of Li/Air Batteries. *J. Electrochem. Soc.* **2012**, *159*, R1−R30.
(83) Levi, E.; Mitelman, A.; Aurbach, D.; Brunelli, M. Structural Mechanism of the Phase Transitions in the Mg-Cu-Mo_6S_8 System Probed by ex Situ Synchrotron X-ray Diffraction. *Chem. Mater.* **2007**, *19*, 5131−5142.
(84) Małecki, G.; Ratuszna, A. Crystal structure of cyanometallates $Me_3[Co(CN)_6]_2$ and $KMe[Fe(CN)_6]$ with Me = Mn^{2+}, Ni^{2+}, Cu^{2+}. *Powder Diffr.* **1999**, *14*, 25−30.
(85) McKinnon, W. R.; Dahn, J. R. Structure and electrochemistry of $Li_xMo_6S_8$. *Phys. Rev. B: Condens. Matter Mater. Phys.* **1985**, *31*, 3084−3087.
(86) Chae, M. S.; Heo, J. W.; Lim, S.-C.; Hong, S.-T. Electrochemical Zinc-Ion Intercalation Properties and Crystal Structures of $ZnMo_6S_8$ and $Zn_2Mo_6S_8$ Chevrel Phases in Aqueous Electrolytes. *Inorg. Chem.* **2016**, *55*, 3294−3301.
(87) Cheng, Y.; Luo, L.; Zhong, L.; Chen, J.; Li, B.; Wang, W.; Mao, S. X.; Wang, C.; Sprenkle, V. L.; Li, G.; Liu, J. Highly Reversible Zinc-Ion Intercalation into Chevrel Phase Mo_6S_8 Nanocubes and Applications for Advanced Zinc-Ion Batteries. *ACS Appl. Mater. Interfaces* **2016**, *8*, 13673−13677.
(88) Geng, L.; Lv, G.; Xing, X.; Guo, J. Reversible Electrochemical Intercalation of Aluminum in Mo_6S_8. *Chem. Mater.* **2015**, *27*, 4926−4929.
(89) Levi, E.; Gershinsky, G.; Aurbach, D.; Isnard, O.; Ceder, G. New Insight on the Unusually High Ionic Mobility in Chevrel Phases. *Chem. Mater.* **2009**, *21*, 1390−1399.
(90) Seghir, S.; Stein, N.; Boulanger, C.; Lecuire, J.-M. Electrochemical determination of the diffusion coefficient of cations into Chevrel phase-based electrochemical transfer junction by potential step chronoamperometry and impedance spectroscopy. *Electrochim. Acta* **2011**, *56*, 2740−2747.
(91) Levi, M. D.; Lancry, E.; Gizbar, H.; Lu, Z.; Levi, E.; Gofer, Y.; Aurbach, D. Kinetic and Thermodynamic Studies of Mg^{2+} and Li^+ Ion Insertion into the Mo_6S_8 Chevrel Phase. *J. Electrochem. Soc.* **2004**, *151*, A1044−A1051.
(92) Rao, C., Biswas, K. In *Essentials of Inorganic Materials Synthesis*; 1st ed.; Rao, C., Biswas, K., Eds.; John Wiley & Sons, Inc.: Hoboken, NJ, 2015.
(93) Kaewmaraya, T.; Ramzan, M.; Osorio-Guillén, J.; Ahuja, R. Electronic structure and ionic diffusion of green battery cathode material: $Mg_2Mo_6S_8$. *Solid State Ionics* **2014**, *261*, 17−20.
(94) Roche, C.; Chevrel, R.; Jenny, A.; Pecheur, P.; Scherrer, H.; Scherrer, S. Crystallography and density of states calculation of $M_xMo_6Se_8$ (*M* = Ti, Cr, Fe, Ni). *Phys. Rev. B: Condens. Matter Mater. Phys.* **1999**, *60*, 16442−16447.
(95) Kganyago, K. R.; Ngoepe, P. E.; Catlow, C. R. A. Voltage profile, structural prediction, and electronic calculations for $Mg_xMo_6S_8$. *Phys. Rev. B: Condens. Matter Mater. Phys.* **2003**, *67*, 104103−1−104103−10.
(96) Levi, E.; Lancry, E.; Mitelman, A.; Aurbach, D.; Ceder, G.; Morgan, D.; Isnard, O. Phase Diagram of Mg Insertion into Chevrel Phases, $Mg_xMo_6T_8$ (T = S, Se). 1. Crystal Structure of the Sulfides. *Chem. Mater.* **2006**, *18*, 5492−5503.
(97) Levi, E.; Gershinsky, G.; Aurbach, D.; Isnard, O. Crystallography of Chevrel Phases, MMo_6T_8 (M = Cd, Na, Mn, and Zn, T = S, Se) and Their Cation Mobility. *Inorg. Chem.* **2009**, *48*, 8751−8758.
(98) Saha, P.; Jampani, P. H.; Datta, M. K.; Okoli, C. U.; Manivannan, A.; Kumta, P. N. A Convenient Approach to Mo_6S_8 Chevrel Phase Cathode for Rechargeable Magnesium Battery. *J. Electrochem. Soc.* **2014**, *161*, A593−A598.
(99) Lancry, E.; Levi, E.; Gofer, Y.; Levi, M.; Salitra, G.; Aurbach, D. Leaching Chemistry and the Performance of the Mo_6S_8 Cathodes in Rechargeable Mg Batteries. *Chem. Mater.* **2004**, *16*, 2832−2838.
(100) Schöllhorn, R.; Kümpers, M.; Besenhard, J. Topotactic redox reactions of the channel type chalcogenides Mo_3S_4 and Mo_3Se_4. *Mater. Res. Bull.* **1977**, *12*, 781−788.
(101) Cheng, Y.; Parent, L. R.; Shao, Y.; Wang, C.; Sprenkle, V. L.; Li, G.; Liu, J. Facile Synthesis of Chevrel Phase Nanocubes and Their Applications for Multivalent Energy Storage. *Chem. Mater.* **2014**, *26*, 4904−4907.
(102) Ritter, C.; Gocke, E.; Fischer, C.; Schöllhorn, R. Neutron diffraction study on the crystal structure of lithium intercalated chevrel phases. *Mater. Res. Bull.* **1992**, *27*, 1217−1225.
(103) Mitelman, A.; Levi, M. D.; Lancry, E.; Levi, E.; Aurbach, D. New cathode materials for rechargeable Mg batteries: fast Mg ion transport and reversible copper extrusion in $CuyMo_6S_8$ compounds. *Chem. Commun.* **2007**, 4212−4214.
(104) Choi, S.-H.; Kim, J.-S.; Woo, S.-G.; Cho, W.; Choi, S. Y.; Choi, J.; Lee, K.-T.; Park, M.-S.; Kim, Y.-J. Role of Cu in Mo_6S_8 and Cu Mixture Cathodes for Magnesium Ion Batteries. *ACS Appl. Mater. Interfaces* **2015**, *7*, 7016−7024.
(105) Woo, S.-G.; Yoo, J.-Y.; Cho, W.; Park, M.-S.; Kim, K. J.; Kim, J.-H.; Kim, J.-S.; Kim, Y.-J. Copper incorporated $Cu_xMo_6S_8$ ($x \geq 1$) Chevrel-phase cathode materials synthesized by chemical intercalation

DOI: 10.1021/acs.chemrev.6b00614
Chem. Rev. 2017, 117, 4287−4341

process for rechargeable magnesium batteries. *RSC Adv.* **2014**, *4*, 59048−59055.
(106) Liu, M.; Jain, A.; Rong, Z.; Qu, X.; Canepa, P.; Malik, R.; Ceder, G.; Persson, K. Evaluation of sulfur spinel compounds for multivalent battery cathode applications. *Energy Environ. Sci.* **2016**, *9*, 3201−3209.
(107) Levi, E.; Aurbach, D. Chevrel Phases, $M_xMo_6T_8$ (M = Metals, T = S, Se, Te) as a Structural Chameleon: Changes in the Rhombohedral Framework and Triclinic Distortion. *Chem. Mater.* **2010**, *22*, 3678−3692.
(108) Nikolowski, K.; Bramnik, N.; Baehtz, C.; Ehrenberg, H. In situ XRD Analysis of Magnesium Batteries. http://hasyweb.desy.de/science/annual_reports/2004_report/part1/contrib/41/12712.pdf (addessed December 20, 2016).
(109) Levi, E.; Mitelman, A.; Aurbach, D.; Isnard, O. On the Mechanism of Triclinic Distortion in Chevrel Phase as Probed by In-Situ Neutron Diffraction. *Inorg. Chem.* **2007**, *46*, 7528−7535.
(110) Thöle, F.; Wan, L. F.; Prendergast, D. Re-examining the Chevrel phase Mo_6S_8 cathode for Mg intercalation from an electronic structure perspective. *Phys. Chem. Chem. Phys.* **2015**, *17*, 22548−22551.
(111) Wan, L. F.; Wright, J.; Perdue, B. R.; Fister, T. T.; Kim, S.; Apblett, C. A.; Prendergast, D. Revealing electronic structure changes in Chevrel phase cathodes upon Mg insertion using X-ray absorption spectroscopy. *Phys. Chem. Chem. Phys.* **2016**, *18*, 17326−17329.
(112) Smeu, M.; Hossain, M. S.; Wang, Z.; Timoshevskii, V.; Bevan, K. H.; Zaghib, K. Theoretical investigation of Chevrel phase materials for cathodes accommodating Ca^{2+} ions. *J. Power Sources* **2016**, *306*, 431−436.
(113) Wang, Y.; Richards, W. D.; Ong, S. P.; Miara, L. J.; Kim, J. C.; Mo, Y.; Ceder, G. Design principles for solid-state lithium superionic conductors. *Nat. Mater.* **2015**, *14*, 1026−1031.
(114) Shannon, R. D. Revised effective ionic radii and systematic studies of interatomic distances in halides and chalcogenides. *Acta Crystallogr., Sect. A: Cryst. Phys., Diffr., Theor. Gen. Crystallogr.* **1976**, *32*, 751−767.
(115) Whittingham, M. S. Chemistry of intercalation compounds: Metal guests in chalcogenide hosts. *Prog. Solid State Chem.* **1978**, *12*, 41−99.
(116) Aydinol, M. K.; Kohan, A. F.; Ceder, G.; Cho, K.; Joannopoulos, J. Ab initio study of lithium intercalation in metal oxides and metal dichalcogenides. *Phys. Rev. B: Condens. Matter Mater. Phys.* **1997**, *56*, 1354−1365.
(117) Whittingham, M. S. Lithium Batteries and Cathode Materials. *Chem. Rev.* **2004**, *104*, 4271−4302.
(118) Bruce, P. G.; Krok, F.; Nowinski, J.; Gibson, V. C.; Tavakkoli, K. Chemical intercalation of magnesium into solid hosts. *J. Mater. Chem.* **1991**, *1*, 705−706.
(119) Bruce, P.; Krok, F.; Lighfoot, P.; Nowinski, J. L. Multivalent cation intercalation. *Solid State Ionics* **1992**, *53*−*56*, 351−355.
(120) Amir, N.; Vestfrid, Y.; Chusid, O.; Gofer, Y.; Aurbach, D. Progress in nonaqueous magnesium electrochemistry. *J. Power Sources* **2007**, *174*, 1234−1240.
(121) Sun, X.; Duffort, V.; Bonnick, P.; Rong, Z.; Liu, M.; Persson, K.; Ceder, G.; Nazar, L. F. A High Capacity Thiospinel Cathode for Mg Batteries. *Energy Environ. Sci.* **2016**, *9*, 2273−2277.
(122) Tao, Z.-L.; Xu, L.-N.; Gou, X.-L.; Chen, J.; Yuan, H.-T. TiS_2 nanotubes as the cathode materials of Mg-ion batteries. *Chem. Commun.* **2004**, 2080−2081.
(123) Sun, X.; Bonnick, P.; Nazar, L. F. Layered TiS_2Positive Electrode for Mg Batteries. *ACS Energy Lett.* **2016**, *1*, 297−301.
(124) Emly, A.; Van der Ven, A. Mg Intercalation in Layered and Spinel Host Crystal Structures for Mg Batteries. *Inorg. Chem.* **2015**, *54*, 4394−4402.
(125) Lightfoot, P.; Krok, F.; Nowinski, J. L.; Bruce, P. G. Structure of the cubic intercalate Mg_xTiS_2. *J. Mater. Chem.* **1992**, *2*, 139−140.
(126) Dahn, J. R.; McKinnon, W. R.; Haering, R. R.; Buyers, W. J. L.; Powell, B. M. Structure determination of Li_xTiS_2 by neutron diffraction. *Can. J. Phys.* **1980**, *58*, 207−213.
(127) Doe, R. E.; Downie, C. M.; Fischer, C.; Lane, G. H.; Morgan, D.; Nevin, J.; Ceder, G.; Persson, K. A.; Eaglesham, D. Layered materials with improved magnesium intercalation for rechargeable magnesium ion cells. U.S. Patent App. 13/794,551, 2013.
(128) Li, X.-L.; Li, Y.-D. MoS_2 Nanostructures: Synthesis and Electrochemical Mg^{2+} Intercalation. *J. Phys. Chem. B* **2004**, *108*, 13893−13900.
(129) Liang, Y.; Yoo, H. D.; Li, Y.; Shuai, J.; Calderon, H. A.; Robles Hernandez, F. C.; Grabow, L. C.; Yao, Y. Interlayer-Expanded Molybdenum Disulfide Nanocomposites for Electrochemical Magnesium Storage. *Nano Lett.* **2015**, *15*, 2194−2202.
(130) Liang, Y.; Feng, R.; Yang, S.; Ma, H.; Liang, J.; Chen, J. Rechargeable Mg Batteries with Graphene-like MoS_2 Cathode and Ultrasmall Mg Nanoparticle Anode. *Adv. Mater.* **2011**, *23*, 640−643.
(131) Yang, S.; Li, D.; Zhang, T.; Tao, Z.; Chen, J. First-Principles Study of Zigzag MoS_2 Nanoribbon As a Promising Cathode Material for Rechargeable Mg Batteries. *J. Phys. Chem. C* **2012**, *116*, 1307−1312.
(132) Shuai, J.; Yoo, H. D.; Liang, Y.; Li, Y.; Yao, Y.; Grabow, L. C. Density functional theory study of Li, Na, and Mg intercalation and diffusion in $MoS_2$with controlled interlayer spacing. *Mater. Res. Express* **2016**, *3*, 064001−1−064001−8.
(133) Gu, Y.; Katsura, Y.; Yoshino, T.; Takagi, H.; Taniguchi, K. Rechargeable magnesium-ion battery based on a $TiSe_2$-cathode with *d*-*p* orbital hybridized electronic structure. *Sci. Rep.* **2015**, *5*, 12486.
(134) Liu, B.; Luo, T.; Mu, G.; Wang, X.; Chen, D.; Shen, G. Rechargeable Mg-Ion Batteries Based on WSe_2 Nanowire Cathodes. *ACS Nano* **2013**, *7*, 8051−8058.
(135) Schutte, W. J.; De Boer, J. L.; Jellinek, F. Crystal structures of tungsten disulfide and diselenide. *J. Solid State Chem.* **1987**, *70*, 207−209.
(136) Gao, T.; Noked, M.; Pearse, A. J.; Gillette, E.; Fan, X.; Zhu, Y.; Luo, C.; Suo, L.; Schroeder, M. A.; Xu, K.; Lee, S. B.; Rubloff, G. W.; Wang, C. Enhancing the Reversibility of Mg/S Battery Chemistry through Li^+ Mediation. *J. Am. Chem. Soc.* **2015**, *137*, 12388−12393.
(137) Zhao-Karger, Z.; Zhao, X.; Wang, D.; Diemant, T.; Behm, R. J.; Fichtner, M. Performance Improvement of Magnesium Sulfur Batteries with Modified Non-Nucleophilic Electrolytes. *Adv. Energy Mater.* **2015**, *5*, 1401155.
(138) Yu, X.; Manthiram, A. Performance Enhancement and Mechanistic Studies of Magnesium-Sulfur Cells with an Advanced Cathode Structure. *ACS Energy Lett.* **2016**, *1*, 431−437.
(139) Kubaschewski, O.; Evans, E. L.; Alcock, C. B. *Metallurgical Thermochemistry*; Pergamon Press: Oxford, 1967.
(140) Mizushima, K.; Jones, P.; Wiseman, P.; Goodenough, J. Li_xCoO_2 ($0<x \leq 1$): A new cathode material for batteries of high energy density. *Solid State Ionics* **1981**, *3*-*4*, 171−174.
(141) Levi, E.; Gofer, Y.; Aurbach, D. On the Way to Rechargeable Mg Batteries: The Challenge of New Cathode Materials. *Chem. Mater.* **2010**, *22*, 860−868.
(142) Rong, Z.; Malik, R.; Canepa, P.; Sai Gautam, G.; Liu, M.; Jain, A.; Persson, K.; Ceder, G. Materials Design Rules for Multivalent Ion Mobility in Intercalation Structures. *Chem. Mater.* **2015**, *27*, 6016−6021.
(143) Kai, K.; Kobayashi, Y.; Yamada, Y.; Miyazaki, K.; Abe, T.; Uchimoto, Y.; Kageyama, H. Electrochemical characterization of single-layer MnO_2 nanosheets as a high-capacitance pseudocapacitor electrode. *J. Mater. Chem.* **2012**, *22*, 14691−14695.
(144) Fang, W.-C.; Fang, W.-L. Fast and reversible surface redox reduction in V_2O_5 dispersed on CN_x nanotubes. *Chem. Commun.* **2008**, 5236−5238.
(145) Kim, S.; Nam, K. W.; Lee, S.; Cho, W.; Kim, J.-S.; Kim, B. G.; Oshima, Y.; Kim, J.-S.; Doo, S.-G.; Chang, H.; Aurbach, D.; Choi, J. W. Direct Observation of an Anomalous Spinel-to-Layered Phase Transition Mediated by Crystal Water Intercalation. *Angew. Chem., Int. Ed.* **2015**, *54*, 15094−15099.
(146) Novák, P.; Desilvestro, J. Electrochemical Insertion of Magnesium in Metal Oxides and Sulfides from Aprotic Electrolytes. *J. Electrochem. Soc.* **1993**, *140*, 140−144.

DOI: 10.1021/acs.chemrev.6b00614
Chem. Rev. 2017, 117, 4287−4341

(147) Nam, K. W.; et al. The High Performance of Crystal Water Containing Manganese Birnessite Cathodes for Magnesium Batteries. *Nano Lett.* **2015**, *15*, 4071−4079.
(148) Zhou, F.; Cococcioni, M.; Marianetti, C. A.; Morgan, D.; Ceder, G. First-principles prediction of redox potentials in transition-metal compounds with LDA+*U*. *Phys. Rev. B: Condens. Matter Mater. Phys.* **2004**, *70*, 235121−1−235121−8.
(149) Jain, A.; Ong, S. P.; Hautier, G.; Chen, W.; Richards, W. D.; Dacek, S.; Cholia, S.; Gunter, D.; Skinner, D.; Ceder, G.; Persson, K. A. The Materials Project: A materials genome approach to accelerating materials innovation. *APL Mater.* **2013**, *1*, 011002.
(150) Sempolinski, D. R.; Kingery, W. D. Ionic conductivity and Magnesium Vacancy mobility in Magnesium Oxide. *J. Am. Ceram. Soc.* **1980**, *63*, 664−669.
(151) Spahr, M.; Novák, P.; Haas, O.; Nesper, R. Electrochemical insertion of lithium, sodium, and magnesium in molybdenum(VI) oxide. *J. Power Sources* **1995**, *54*, 346−351.
(152) Sian, T. S.; Reddy, G. B.; Shivaprasad, S. M. Study of Mg ion Intercalation in Polycrystalline MoO_3 Thin Films. *Jpn. J. Appl. Phys.* **2004**, *43*, 6248−6251.
(153) Sian, T. S.; Reddy, G. B.; Shivaprasad, S. M. Effect of Microstructure and Stoichiometry on Absorption in Mg Intercalated MoO_3 Thin Films. *Electrochem. Solid-State Lett.* **2006**, *9*, A120−A122.
(154) Campanella, L.; Pistoia, G. MoO_3: A New Electrode Material for Nonaqueous Secondary Battery Applications. *J. Electrochem. Soc.* **1971**, *118*, 1905−1908.
(155) Incorvati, J. T.; Wan, L. F.; Key, B.; Zhou, D.; Liao, C.; Fuoco, L.; Holland, M.; Wang, H.; Prendergast, D.; Poeppelmeier, K. R.; Vaughey, J. T. Reversible Magnesium Intercalation into a Layered Oxyfluoride Cathode. *Chem. Mater.* **2016**, *28*, 17−20.
(156) Gofer, Y.; Turgeman, R.; Cohen, H.; Aurbach, D. XPS Investigation of Surface Chemistry of Magnesium Electrodes in Contact with Organic Solutions of Organochloroaluminate Complex Salts. *Langmuir* **2003**, *19*, 2344−2348.
(157) Wang, J.; Polleux, J.; Lim, J.; Dunn, B. Pseudocapacitive Contributions to Electrochemical Energy Storage in TiO_2 (Anatase) Nanoparticles. *J. Phys. Chem. C* **2007**, *111*, 14925−14931.
(158) Arthur, T. S.; Zhang, R.; Ling, C.; Glans, P.-A.; Fan, X.; Guo, J.; Mizuno, F. Understanding the Electrochemical Mechanism of K-αMnO_2 for Magnesium Battery Cathodes. *ACS Appl. Mater. Interfaces* **2014**, *6*, 7004−7008.
(159) Kaveevivitchai, W.; Jacobson, A. J. High Capacity Rechargeable Magnesium-Ion Batteries Based on a Microporous Molybdenum-Vanadium Oxide Cathode. *Chem. Mater.* **2016**, *28*, 4593−4601.
(160) Gautam, G. S.; Sun, X.; Duffort, V.; Nazar, L. F.; Ceder, G. Impact of Intermediate Sites on Bulk Diffusion Barriers: Mg intercalation in $Mg_2Mo_3O_8$. *J. Mater. Chem. A* **2016**, *4*, 17643−17648.
(161) Arroyo-de Dompablo, M. E.; Krich, C.; Nava-Avaendaño, J.; Palacín, M. R.; Bardé, F. In quest of cathode materials for Ca ion batteries: the $CaMO_3$ perovskites (M = Mo, Cr, Mn, Fe, Co, Ni). *Phys. Chem. Chem. Phys.* **2016**, *18*, 19966−19972.
(162) Amatucci, G. G.; Badway, F.; Singhal, A.; Beaudoin, B.; Skandan, G.; Bowmer, T.; Plitz, I.; Pereira, N.; Chapman, T.; Jaworski, R. Investigation of Yttrium and Polyvalent Ion Intercalation into Nanocrystalline Vanadium Oxide. *J. Electrochem. Soc.* **2001**, *148*, A940−A950.
(163) Cabello, M.; Nacimiento, F.; González, J. R.; Ortiz, G.; Alcántara, R.; Lavela, P.; Pérez-Vicente, C.; Tirado, J. L. Advancing towards a veritable calcium-ion battery: $CaCo_2O_4$ positive electrode material. *Electrochem. Commun.* **2016**, *67*, 59−64.
(164) Hayashi, M.; Arai, H.; Ohtsuka, H.; Sakurai, Y. Electrochemical insertion/extraction of calcium ions using crystalline vanadium oxide. *Electrochem. Solid-State Lett.* **2004**, *7*, A119−A121.
(165) Whittingham, M. S. The Role of Ternary Phases in Cathode Reactions. *J. Electrochem. Soc.* **1976**, *123*, 315−320.
(166) Wiesener, K.; Schneider, W.; Ilić, D.; Steger, E.; Hallmeier, K.; Brackmann, E. Vanadium oxides in electrodes for rechargeable lithium cells. *J. Power Sources* **1987**, *20*, 157−164.
(167) Delmas, C.; Cognac-Auradou, H.; Cocciantelli, J.; Ménétrier, M.; Doumerc, J. The $Li_xV_2O_5$ system: An overview of the structure modifications induced by the lithium intercalation. *Solid State Ionics* **1994**, *69*, 257−264.
(168) Cava, R.; Santoro, A.; Murphy, D.; Zahurak, S.; Fleming, R.; Marsh, P.; Roth, R. The structure of the lithium-inserted metal oxide δLiV_2O_5. *J. Solid State Chem.* **1986**, *65*, 63−71.
(169) Sai Gautam, G.; Canepa, P.; Abdellahi, A.; Urban, A.; Malik, R.; Ceder, G. The Intercalation Phase Diagram of Mg in V_2O_5 from First-Principles. *Chem. Mater.* **2015**, *27*, 3733−3742.
(170) Sai Gautam, G.; Canepa, P.; Malik, R.; Liu, M.; Persson, K.; Ceder, G. First-principles evaluation of multi-valent cation insertion into orthorhombic V_2O_5. *Chem. Commun.* **2015**, *51*, 13619−13622.
(171) Novák, P.; Imhof, R.; Haas, O. Magnesium insertion electrodes for rechargeable nonaqueous batteries − a competitive alternative to lithium? *Electrochim. Acta* **1999**, *45*, 351−367.
(172) Pereira-Ramos, J.; Messina, R.; Perichon, J. Electrochemical formation of a magnesium vanadium bronze $Mg_xV_2O_5$ in sulfone-based electrolytes at 150°C. *J. Electroanal. Chem. Interfacial Electrochem.* **1987**, *218*, 241−249.
(173) Novák, P.; Shklover, V.; Nesper, R. Magnesium Insertion in Vanadium Oxides: A Structural Study. *Z. Phys. Chem.* **1994**, *185*, 51−68.
(174) Yu, L.; Zhang, X. Electrochemical insertion of magnesium ions into V_2O_5 from aprotic electrolytes with varied water content. *J. Colloid Interface Sci.* **2004**, *278*, 160−165.
(175) Legendre, J.-J.; Livage, J. Vanadium pentoxide gels: I. Structural study by electron diffraction. *J. Colloid Interface Sci.* **1983**, *94*, 75−83.
(176) Newby, K. R.; Scott, A. B. Discharge Mechanism of the V_2O_5 Electrode. *J. Electrochem. Soc.* **1970**, *117*, 152−156.
(177) Zhou, B.; Shi, H.; Cao, R.; Zhang, X.; Jiang, Z. Theoretical study on the initial stage of a magnesium battery based on a V_2O_5 cathode. *Phys. Chem. Chem. Phys.* **2014**, *16*, 18578−18585.
(178) Wang, Z.; Su, Q.; Deng, H. Single-layered V_2O_5 a promising cathode material for rechargeable Li and Mg ion batteries: an ab initio study. *Phys. Chem. Chem. Phys.* **2013**, *15*, 8705−8709.
(179) Carrasco, J. Role of van der Waals Forces in Thermodynamics and Kinetics of Layered Transition Metal Oxide Electrodes: Alkali and Alkaline-Earth Ion Insertion into V_2O_5. *J. Phys. Chem. C* **2014**, *118*, 19599−19607.
(180) Millet, P.; Satto, C.; Sciau, P.; Galy, J. MgV_2O_5 and $\delta Li_xV_2O_5$: A Comparative Structural Investigation. *J. Solid State Chem.* **1998**, *136*, 56−62.
(181) Matts, I. L.; Dacek, S.; Pietrzak, T. K.; Malik, R.; Ceder, G. Explaining Performance-Limiting Mechanisms in Fluorophosphate Na-Ion Battery Cathodes through Inactive Transition-Metal Mixing and First-Principles Mobility Calculations. *Chem. Mater.* **2015**, *27*, 6008−6015.
(182) Rossouw, M.; Liles, D.; Thackeray, M.; David, W.; Hull, S. Alpha manganese dioxide for lithium batteries: A structural and electrochemical study. *Mater. Res. Bull.* **1992**, *27*, 221−230.
(183) Tripathi, R.; Ramesh, T. N.; Ellis, B. L.; Nazar, L. F. Scalable Synthesis of Tavorite $LiFeSO_4F$ and $NaFeSO_4F$ Cathode Materials. *Angew. Chem.* **2010**, *122*, 8920−8924.
(184) Zhang, L.; Tarascon, J.-M.; Sougrati, M. T.; Rousse, G.; Chen, G. Influence of relative humidity on the structure and electrochemical performance of sustainable $LiFeSO_4F$ electrodes for Li-ion batteries. *J. Mater. Chem. A* **2015**, *3*, 16988−16997.
(185) Xiao, P.; Song, J.; Wang, L.; Goodenough, J. B.; Henkelman, G. Theoretical Study of the Structural Evolution of a $Na_2FeMn(CN)_6$ Cathode upon Na Intercalation. *Chem. Mater.* **2015**, *27*, 3763−3768.
(186) Kim, H.; Hong, J.; Yoon, G.; Kim, H.; Park, K.-Y.; Park, M.-S.; Yoon, W.-S.; Kang, K. Sodium intercalation chemistry in graphite. *Energy Environ. Sci.* **2015**, *8*, 2963−2969.
(187) Sai Gautam, G.; Canepa, P.; Richards, W. D.; Malik, R.; Ceder, G. Role of Structural H_2O in intercalation electrodes: the case of Mg in Nanocrystalline Xerogel-V_2O_5. *Nano Lett.* **2016**, *16*, 2426−2431.
(188) Petkov, V.; Trikalitis, P. N.; Bozin, E. S.; Billinge, S. J. L.; Vogt, T.; Kanatzidis, M. G. Structure of $V_2O_5{\cdot}nH_2O$ Xerogel Solved by the

DOI: 10.1021/acs.chemrev.6b00614
Chem. Rev. 2017, 117, 4287−4341

Atomic Pair Distribution Function Technique. *J. Am. Chem. Soc.* **2002**, *124*, 10157−10162.
(189) Oka, Y.; Tamada, O.; Yao, T.; Yamamoto, N. Synthesis and Crystal Structure of σ-$Zn_{0.25}V_2O_5{\cdot}H_2O$ with a Novel Type of V_2O_5 Layer. *J. Solid State Chem.* **1996**, *126*, 65−73.
(190) Oka, Y.; Yao, T.; Yamamoto, N. Crystal Structures of Hydrated Vanadium Oxides with δ-Type V_2O_5 Layers: δ-$M_{0.25}V_2O_5{\cdot}H_2O$, M = Ca, Ni. *J. Solid State Chem.* **1997**, *132*, 323−329.
(191) Bervas, M.; Klein, L.; Amatucci, G. Vanadium oxide-propylene carbonate composite as a host for the intercalation of polyvalent cations. *Solid State Ionics* **2005**, *176*, 2735−2747.
(192) Stojković, I.; Cvjetićanin, N.; Marković, S.; Mitrić, M.; Mentus, S. Electrochemical Behaviour of V_2O_5 Xerogel and V_2O_5 Xerogel/C Composite in an Aqueous $LiNO_3$ and $Mg(NO_3)_2$ Solutions. *Acta Phys. Pol., A* **2010**, *117*, 837−840.
(193) Lee, S. H.; DiLeo, R. A.; Marschilok, A. C.; Takeuchi, K. J.; Takeuchi, E. S. Sol Gel Based Synthesis and Electrochemistry of Magnesium Vanadium Oxide: A Promising Cathode Material for Secondary Magnesium Ion Batteries. *ECS Electrochem. Lett.* **2014**, *3*, A87−A90.
(194) Tepavcevic, S.; Xiong, H.; Stamenkovic, V. R.; Zuo, X.; Balasubramanian, M.; Prakapenka, V. B.; Johnson, C. S.; Rajh, T. Nanostructured Bilayered Vanadium Oxide Electrodes for Rechargeable Sodium-Ion Batteries. *ACS Nano* **2012**, *6*, 530−538.
(195) Tepavcevic, S.; Liu, Y.; Zhou, D.; Lai, B.; Maser, J.; Zuo, X.; Chan, H.; Král, P.; Johnson, C. S.; Stamenkovic, V.; et al. Nanostructured Layered Cathode for Rechargeable Mg-Ion Batteries. *ACS Nano* **2015**, *9*, 8194−8205.
(196) Vujković, M.; Pašti, I.; Simatović, I. S.; Šljukić, B.; Milenković, M.; Mentus, S. The influence of intercalated ions on cyclic stability of V_2O_5/graphite composite in aqueous electrolytic solutions: experimental and theoretical approach. *Electrochim. Acta* **2015**, *176*, 130−140.
(197) Le, D.; Passerini, S.; Coustier, F.; Guo, J.; Soderstrom, T.; Owens, B.; Smyrl, W. Intercalation of polyvalent cations into V_2O_5 aerogels. *Chem. Mater.* **1998**, *10*, 682−684.
(198) Sa, N.; Kinnibrugh, T. L.; Wang, H.; Gautam, G. S.; Chapman, K. W.; Vaughey, J. T.; Key, B.; Fister, T. T.; Freeland, J. W.; Proffit, D. L.; Chupas, P. J.; Ceder, G.; Bareno, J. G.; Bloom, I. D.; Burrell, A. K. Structural Evolution of Reversible Mg Insertion into a Bilayer Structure of $V_2O_5{\cdot}nH_2O$ Xerogel Material. *Chem. Mater.* **2016**, *28*, 2962−2969.
(199) Senguttuvan, P.; Han, S.-D.; Kim, S.; Lipson, A. L.; Tepavcevic, S.; Fister, T. T.; Bloom, I. D.; Burrell, A. K.; Johnson, C. S. A High Power Rechargeable Nonaqueous Multivalent Zn/V_2O_5 Battery. *Adv. Energy Mater.* **2016**, *6*, 1600826.
(200) Imamura, D.; Miyayama, M. Characterization of magnesium-intercalated V_2O_5/carbon composites. *Solid State Ionics* **2003**, *161*, 173−180.
(201) Imamura, D.; Miyayama, M.; Hibino, M.; Kudo, T. Mg Intercalation Properties into V_2O_5 gel/Carbon Composites under High-Rate Condition. *J. Electrochem. Soc.* **2003**, *150*, A753−A758.
(202) Yin, J.; Pelliccione, C. J.; Lee, S. H.; Takeuchi, E. S.; Takeuchi, K. J.; Marschilok, A. C. Communication−Sol-Gel Synthesized Magnesium Vanadium Oxide, $Mg_xV_2O_5{\cdot}nH_2O$: The Role of Structural Mg^{2+} on Battery Performance. *J. Electrochem. Soc.* **2016**, *163*, A1941−A1943.
(203) Sinha, N. N.; Munichandraiah, N. Electrochemical Conversion of $LiMn_2O_4$ to $MgMn_2O_4$ in Aqueous Electrolytes. *Electrochem. Solid-State Lett.* **2008**, *11*, F23−F26.
(204) Yuan, C.; Zhang, Y.; Pan, Y.; Liu, X.; Wang, G.; Cao, D. Investigation of the intercalation of polyvalent cations (Mg^{2+}, Zn^{2+}) into λ-MnO_2 for rechargeable aqueous battery. *Electrochim. Acta* **2014**, *116*, 404−412.
(205) Kundu, D.; Adams, B. D.; Duffort, V.; Vajargah, S. H.; Nazar, L. F. A high-capacity and long-life aqueous rechargeable zinc battery using a metal oxide intercalation cathode. *Nat. Energy* **2016**, *1*, 16119−1−16119−8.
(206) Dampier, F. W. The Cathodic Behavior of CuS, MoO_3, and MnO_2 in Lithium Cells. *J. Electrochem. Soc.* **1974**, *121*, 656−660.
(207) Pistoia, G. Some Restatements on the Nature and Behavior of MnO_2 for Li Batteries. *J. Electrochem. Soc.* **1982**, *129*, 1861−1865.
(208) Bach, S.; Pereira-Ramos, J. P.; Baffier, N. A new MnO_2 tunnel related phase as host lattice for Li intercalation. *Solid State Ionics* **1995**, *80*, 151−158.
(209) Thackeray, M.; Johnson, P.; de Picciotto, L.; Bruce, P.; Goodenough, J. Electrochemical extraction of lithium from $LiMn_2O_4$. *Mater. Res. Bull.* **1984**, *19*, 179−187.
(210) Renuka, R.; Ramamurthy, S. An investigation on layered birnessite type manganese oxides for battery applications. *J. Power Sources* **2000**, *87*, 144−152.
(211) Kumagai, N.; Komaba, S.; Sakai, H.; Kumagai, N. Preparation of todorokite-type manganese-based oxide and its application as lithium and magnesium rechargeable battery cathode. *J. Power Sources* **2001**, *97*−*98*, 515−517.
(212) Kumagai, N.; Komaba, S.; Abe, K.; Yashiro, H. Synthesis of metal-doped todorokite-type MnO_2 and its cathode characteristics for rechargeable lithium batteries. *J. Power Sources* **2005**, *146*, 310−314.
(213) Li, C.; Cheng, F.; Ji, W.; Tao, Z.; Chen, J. Magnesium microspheres and nanospheres: Morphology-controlled synthesis and application in Mg/MnO_2 batteries. *Nano Res.* **2009**, *2*, 713−721.
(214) Minakshi, M.; Blackford, M.; Ionescu, M. Characterization of alkaline-earth oxide additions to the MnO_2 cathode in an aqueous secondary battery. *J. Alloys Compd.* **2011**, *509*, 5974−5980.
(215) Rasul, S.; Suzuki, S.; Yamaguchi, S.; Miyayama, M. High capacity positive electrodes for secondary Mg-ion batteries. *Electrochim. Acta* **2012**, *82*, 243−249.
(216) Rasul, S.; Suzuki, S.; Yamaguchi, S.; Miyayama, M. Synthesis and electrochemical behavior of hollandite MnO_2/acetylene black composite cathode for secondary Mg-ion batteries. *Solid State Ionics* **2012**, *225*, 542−546.
(217) Rasul, S.; Suzuki, S.; Yamaguchi, S.; Miyayama, M. Manganese oxide octahedral molecular sieves as insertion electrodes for rechargeable Mg batteries. *Electrochim. Acta* **2013**, *110*, 247−252.
(218) Zhang, R.; Yu, X.; Nam, K.-W.; Ling, C.; Arthur, T. S.; Song, W.; Knapp, A. M.; Ehrlich, S. N.; Yang, X.-Q.; Matsui, M. α-MnO_2 as a cathode material for rechargeable Mg batteries. *Electrochem. Commun.* **2012**, *23*, 110−113.
(219) Kim, J.-S.; Chang, W.-S.; Kim, R.-H.; Kim, D.-Y.; Han, D.-W.; Lee, K.-H.; Lee, S.-S.; Doo, S.-G. High-capacity nanostructured manganese dioxide cathode for rechargeable magnesium ion batteries. *J. Power Sources* **2015**, *273*, 210−215.
(220) Song, J.; Noked, M.; Gillette, E.; Duay, J.; Rubloff, G.; Lee, S. B. Activation of α-MnO_2 cathode by water-stimulated Mg^{2+} insertion for a magnesium ion battery. *Phys. Chem. Chem. Phys.* **2015**, *17*, 5256−5264.
(221) Zhang, R.; Arthur, T. S.; Ling, C.; Mizuno, F. Manganese dioxides as rechargeable magnesium battery cathode; synthetic approach to understand magnesiation process. *J. Power Sources* **2015**, *282*, 630−638.
(222) Jarvis, L. The beneficial effect of increased cathode water content on Mg/MnO_2 battery performance. *J. Power Sources* **1990**, *32*, 271−276.
(223) Knight, J. C.; Therese, S.; Manthiram, A. On the Utility of Spinel Oxide Hosts for Magnesium-Ion Batteries. *ACS Appl. Mater. Interfaces* **2015**, *7*, 22953−22961.
(224) Cabello, M.; Alcantara, R.; Nacimiento, F.; Ortiz, G.; Lavela, P.; Tirado, J. L. Electrochemical and chemical insertion/deinsertion of magnesium in spinel-type $MgMn_2O_4$ and λ-MnO_2 for both aqueous and non-aqueous magnesium-ion batteries. *CrystEngComm* **2015**, *17*, 8728−8735.
(225) Ling, C.; Zhang, R.; Arthur, T. S.; Mizuno, F. How General is the Conversion Reaction in Mg Battery Cathode: A Case Study of the Magnesiation of α-MnO_2. *Chem. Mater.* **2015**, *27*, 5799−5807.
(226) Feng, Z.; et al. Phase-Controlled Electrochemical Activity of Epitaxial Mg-Spinel Thin Films. *ACS Appl. Mater. Interfaces* **2015**, *7*, 28438−28443.

DOI: 10.1021/acs.chemrev.6b00614
Chem. Rev. 2017, 117, 4287−4341

(227) Sun, X.; Duffort, V.; Mehdi, B. L.; Browning, N. D.; Nazar, L. F. Investigation of the Mechanism of Mg Insertion in Birnessite in Nonaqueous and Aqueous Rechargeable Mg-Ion Batteries. *Chem. Mater.* **2016**, *28*, 534−542.
(228) Xu, C.; Li, B.; Du, H.; Kang, F. Energetic Zinc Ion Chemistry: The Rechargeable Zinc Ion Battery. *Angew. Chem., Int. Ed.* **2012**, *51*, 933−935.
(229) Minakshi, M. Alkaline-Earth Oxide Modified MnO_2 Cathode: Enhanced Performance in an Aqueous Rechargeable Battery. *Ind. Eng. Chem. Res.* **2011**, *50*, 8792−8795.
(230) Xu, C.; Chiang, S. W.; Ma, J.; Kang, F. Investigation on Zinc Ion Storage in Alpha Manganese Dioxide for Zinc Ion Battery by Electrochemical Impedance Spectrum. *J. Electrochem. Soc.* **2013**, *160*, A93−A97.
(231) Lee, J.; Ju, J. B.; Cho, W. I. C.; Cho, B. W.; Oh, S. H. Todorokite-type MnO_2 as a zinc-ion intercalating material. *Electrochim. Acta* **2013**, *112*, 138−143.
(232) Lee, B.; Yoon, C. S.; Lee, H. R.; Chung, K. Y.; Cho, B. W.; Oh, S. H. Electrochemically-induced reversible transition from the tunneled to layered polymorphs of manganese dioxide. *Sci. Rep.* **2014**, *4*, 6066.
(233) Alfaruqi, M. H.; Mathew, V.; Gim, J.; Kim, S.; Song, J.; Baboo, J. P.; Choi, S. H.; Kim, J. Electrochemically Induced Structural Transformation in a γ-MnO_2 Cathode of a High Capacity Zinc-Ion Battery System. *Chem. Mater.* **2015**, *27*, 3609−3620.
(234) Knight, J. C.; Therese, S.; Manthiram, A. Chemical extraction of Zn from $ZnMn_2O_4$-based spinels. *J. Mater. Chem. A* **2015**, *3*, 21077−21082.
(235) Pan, H.; Shao, Y.; Yan, P.; Cheng, Y.; Han, K. S.; Nie, Z.; Wang, C.; Yang, J.; Li, X.; Bhattacharya, P.; Mueller, K. T.; Liu, J. Reversible aqueous zinc/manganese oxide energy storage from conversion reactions. *Nat. Energy* **2016**, *1*, 16039.
(236) Kim, C.; Phillips, P. J.; Key, B.; Yi, T.; Nordlund, D.; Yu, Y.-S.; Bayliss, R. D.; Han, S.-D.; He, M.; Zhang, Z.; Burrell, A. K.; Klie, R. F.; Cabana, J. Direct Observation of Reversible Magnesium Ion Intercalation into a Spinel Oxide Host. *Adv. Mater.* **2015**, *27*, 3377−3384.
(237) Messaoudi, B.; Joiret, S.; Keddam, M.; Takenouti, H. Anodic behaviour of manganese in alkaline medium. *Electrochim. Acta* **2001**, *46*, 2487−2498.
(238) Brock, S. L.; Duan, N.; Tian, Z. R.; Giraldo, O.; Zhou, H.; Suib, S. L. A Review of Porous Manganese Oxide Materials. *Chem. Mater.* **1998**, *10*, 2619−2628.
(239) Stobbe, E.; De Boer, B.; Geus, J. The reduction and oxidation behaviour of manganese oxides. *Catal. Today* **1999**, *47*, 161−167.
(240) Liu, M.; Rong, Z.; Malik, R.; Canepa, P.; Jain, A.; Ceder, G.; Persson, K. A. Spinel compounds as multivalent battery cathodes: a systematic evaluation based on *ab* initio calculations. *Energy Environ. Sci.* **2015**, *8*, 964−974.
(241) Lee, B.; Lee, H. R.; Kim, H.; Chung, K. Y.; Cho, B. W.; Oh, S. H. Elucidating the intercalation mechanism of zinc ions into α-MnO_2 for rechargeable zinc batteries. *Chem. Commun.* **2015**, *51*, 9265−9268.
(242) Reed, J.; Ceder, G.; Van Der Ven, A. Layered-to-Spinel Phase Transition in Li_xMnO_2. *Electrochem. Solid-State Lett.* **2001**, *4*, A78−A81.
(243) Kim, S.; Lee, S.; Nam, K. W.; Shin, J.; Lim, S. Y.; Cho, W.; Suzuki, K.; Oshima, Y.; Hirayama, M.; Kanno, R.; Choi, J. W. On the Mechanism of Crystal Water Insertion during Anomalous Spinel-to-Birnessite Phase Transition. *Chem. Mater.* **2016**, *28*, 5488−5494.
(244) Alfaruqi, M. H.; Gim, J.; Kim, S.; Song, J.; Pham, D. T.; Jo, J.; Xiu, Z.; Mathew, V.; Kim, J. A layered δ-MnO_2 nanoflake cathode with high zinc-storage capacities for eco-friendly battery applications. *Electrochem. Commun.* **2015**, *60*, 121−125.
(245) Irani, K.; Sinha, A.; Biswas, A. Effect of temperature on the structure of manganites. *J. Phys. Chem. Solids* **1962**, *23*, 711−727.
(246) Mănăilă, R. Cation migration in tetragonal spinels ($MgMn_2O_4$). *J. Phys. Chem. Solids* **1967**, *28*, 2335−2341.
(247) Malavasi, L.; Ghigna, P.; Chiodelli, G.; Maggi, G.; Flor, G. Structural and Transport Properties of $Mg_{1-x}Mn_xMn_2O_{4\pm\delta}$ Spinels. *J. Solid State Chem.* **2002**, *166*, 171−176.
(248) Sánchez, L.; Pereira-Ramos, J.-P. Electrochemical insertion of magnesium in a mixed manganese cobalt oxide. *J. Mater. Chem.* **1997**, *7*, 471−473.
(249) Gupta, R.; Manthiram, A. Chemical Extraction of Lithium from Layered $LiCoO_2$. *J. Solid State Chem.* **1996**, *121*, 483−491.
(250) Venkatraman, S.; Choi, J.; Manthiram, A. Factors influencing the chemical lithium extraction rate from layered $LiNi_{1-y-z}Co_yMn_zO_2$ cathodes. *Electrochem. Commun.* **2004**, *6*, 832−837.
(251) Knight, J. C.; Therese, S.; Manthiram, A. Delithiation Mechanisms in Acid of Spinel $LiMn_{2-x}M_xO4$ (M = Cr, Fe, Co, and Ni) Cathodes. *J. Electrochem. Soc.* **2015**, *162*, A426−A431.
(252) Vitins, G. Lithium Intercalation into Layered $LiMnO_2$. *J. Electrochem. Soc.* **1997**, *144*, 2587−2592.
(253) Mishra, S. K.; Ceder, G. Structural stability of lithium manganese oxides. *Phys. Rev. B: Condens. Matter Mater. Phys.* **1999**, *59*, 6120−6130.
(254) Kitchaev, D. A.; Peng, H.; Liu, Y.; Sun, J.; Perdew, J. P.; Ceder, G. Energetics of MnO_2 polymorphs in density functional theory. *Phys. Rev. B: Condens. Matter Mater. Phys.* **2016**, *93*, 045132.
(255) Lipson, A. L.; Proffit, D. L.; Pan, B.; Fister, T. T.; Liao, C.; Burrell, A. K.; Vaughey, J. T.; Ingram, B. J. Current Collector Corrosion in Ca-Ion Batteries. *J. Electrochem. Soc.* **2015**, *162*, A1574−A1578.
(256) Xu, B.; Meng, S. Factors affecting Li mobility in spinel $LiMn_2O_4$: A first-principles study by GGA and GGA+*U* methods. *J. Power Sources* **2010**, *195*, 4971−4976.
(257) Okamoto, S.; Ichitsubo, T.; Kawaguchi, T.; Kumagai, Y.; Oba, F.; Yagi, S.; Shimokawa, K.; Goto, N.; Doi, T.; Matsubara, E. Intercalation and Push-Out Process with Spinel-to-Rocksalt Transition on Mg Insertion into Spinel Oxides in Magnesium Batteries. *Adv. Sci.* **2015**, *2*, 1500072.
(258) Ling, C.; Mizuno, F. Phase Stability of Post-spinel Compound AMn_2O_4 (A = Li, Na, or Mg) and Its Application as a Rechargeable Battery Cathode. *Chem. Mater.* **2013**, *25*, 3062−3071.
(259) Malavasi, L.; Tealdi, C.; Flor, G.; Amboage, M. High-pressure stability of the tetragonal spinel $MgMn_2O_4$: Role of inversion. *Phys. Rev. B: Condens. Matter Mater. Phys.* **2005**, *71*, 174102.
(260) Yamaura, K.; Huang, Q.; Zhang, L.; Takada, K.; Baba, Y.; Nagai, T.; Matsui, Y.; Kosuda, K.; Takayama-Muromachi, E. Spinel-to-$CaFe_2O_4$ 0Type Structural Transformation in $LiMn_2O_4$ under High Pressure. *J. Am. Chem. Soc.* **2006**, *128*, 9448−9456.
(261) Zhang, R.; Ling, C. Status and challenge of Mg battery cathode. *MRS Energy & Sustainability* **2016**, *3*, E1−1−E1−19.
(262) Arroyo-de Dompablo, M. E.; Krich, C.; Nava-Avendaño, J.; Biškup, N.; Palacín, M. R.; Bardé, F. A Joint Computational and Experimental Evaluation of $CaMn_2O_4$Polymorphs as Cathode Materials for Ca Ion Batteries. *Chem. Mater.* **2016**, *28*, 6886−6893.
(263) Morgan, D.; Van der Ven, A.; Ceder, G. Li Conductivity in Li_xMPO_4 (M = Mn, Fe, Co, Ni) Olivine Materials. *Electrochem. Solid-State Lett.* **2004**, *7*, A30−A32.
(264) Islam, M. S.; Driscoll, D. J.; Fisher, C. A. J.; Slater, P. R. Atomic-Scale Investigation of Defects, Dopants, and Lithium Transport in the $LiFePO_4$ Olivine-Type Battery Material. *Chem. Mater.* **2005**, *17*, 5085−5092.
(265) Kang, B.; Ceder, G. Battery materials for ultrafast charging and discharging. *Nature* **2009**, *458*, 190−193.
(266) Ellis, B. L.; Lee, K. T.; Nazar, L. F. Positive Electrode Materials for Li-Ion and Li-Batteries. *Chem. Mater.* **2010**, *22*, 691−714.
(267) Mueller, T.; Hautier, G.; Jain, A.; Ceder, G. Evaluation of Tavorite-Structured Cathode Materials for Lithium-Ion Batteries Using High-Throughput Computing. *Chem. Mater.* **2011**, *23*, 3854−3862.
(268) Barpanda, P.; Ati, M.; Melot, B. C.; Rousse, G.; Chotard, J.-N.; Doublet, M.-L.; Sougrati, M. T.; Corr, S. A.; Jumas, J.-C.; Tarascon, J.-M. A 3.90 V iron-based fluorosulphate material for lithium-ion

DOI: 10.1021/acs.chemrev.6b00614
Chem. Rev. 2017, 117, 4287−4341

batteries crystallizing in the triplite structure. *Nat. Mater.* **2011**, *10*, 772−77.
(269) Tripathi, R.; Gardiner, G. R.; Islam, M. S.; Nazar, L. F. Alkali-ion Conduction Paths in $LiFeSO_4F$ and $NaFeSO_4F$ Tavorite-Type Cathode Materials. *Chem. Mater.* **2011**, *23*, 2278−2284.
(270) Gaubicher, J.; Wurm, C.; Goward, G.; Masquelier, C.; Nazar, L. Rhombohedral form of $Li_3V_2(PO_4)_3$ as a cathode in Li-ion batteries. *Chem. Mater.* **2000**, *12*, 3240−3242.
(271) Wang, R. Y.; Wessells, C. D.; Huggins, R. A.; Cui, Y. Highly Reversible Open Framework Nanoscale Electrodes for Divalent Ion Batteries. *Nano Lett.* **2013**, *13*, 5748−5752.
(272) Wang, R. Y.; Shyam, B.; Stone, K. H.; Weker, J. N.; Pasta, M.; Lee, H.-W.; Toney, M. F.; Cui, Y. Reversible Multivalent (Monovalent, Divalent, Trivalent) Ion Insertion in Open Framework Materials. *Adv. Energy Mater.* **2015**, *5*, 1401869.
(273) Orikasa, Y.; Masese, T.; Koyama, Y.; Mori, T.; Hattori, M.; Yamamoto, K.; Okado, T.; Huang, Z.-D.; Minato, T.; Tassel, C.; Kim, J.; Kobayashi, Y.; Abe, T.; Kageyama, H.; Uchimoto, Y. High energy density rechargeable magnesium battery using earth-abundant and non-toxic elements. *Sci. Rep.* **2014**, *4*, 5622.
(274) Li, Y.; NuLi, Y.; Yang, J.; Yilinuer, T.; Wang, J. $MgFeSiO_4$ prepared via a molten salt method as a new cathode material for rechargeable magnesium batteries. *Chin. Sci. Bull.* **2011**, *56*, 386−390.
(275) Feng, Z.; Yang, J.; NuLi, Y.; Wang, J.; Wang, X.; Wang, Z. Preparation and electrochemical study of a new magnesium intercalation material $Mg_{1.03}Mn_{0.97}SiO_4$. *Electrochem. Commun.* **2008**, *10*, 1291−1294.
(276) Feng, Z.; Yang, J.; NuLi, Y.; Wang, J. Sol-gel synthesis of $Mg_{1.03}Mn_{0.97}SiO_4$ and its electrochemical intercalation behavior. *J. Power Sources* **2008**, *184*, 604−609.
(277) NuLi, Y.; Yang, J.; Wang, J.; Li, Y. Electrochemical Intercalation of Mg^{2+} in Magnesium Manganese Silicate and Its Application as High-Energy Rechargeable Magnesium Battery Cathode. *J. Phys. Chem. C* **2009**, *113*, 12594−12597.
(278) NuLi, Y.; Yang, J.; Li, Y.; Wang, J. Mesoporous magnesium manganese silicate as cathode materials for rechargeable magnesium batteries. *Chem. Commun.* **2010**, *46*, 3794−3796.
(279) NuLi, Y.-N.; Yang, J.; Zheng, Y.-P.; Wang, J.-L. Mesoporous Magnesium Manganese Silicate as a Cathode Material for Rechargeable Magnesium Batteries. *Wuji Cailiao Xuebao* **2011**, *26*, 129−133.
(280) NuLi, Y.; Zheng, Y.; Wang, F.; Yang, J.; Minett, A. I.; Wang, J.; Chen, J. MWNT/C/$Mg_{1.03}Mn_{0.97}SiO_4$ hierarchical nanostructure for superior reversible magnesium ion storage. *Electrochem. Commun.* **2011**, *13*, 1143−1146.
(281) Ling, C.; Banerjee, D.; Song, W.; Zhang, M.; Matsui, M. First-principles study of the magnesiation of olivines: redox reaction mechanism, electrochemical and thermodynamic properties. *J. Mater. Chem.* **2012**, *22*, 13517−13523.
(282) NuLi, Y.; Zheng, Y.; Wang, Y.; Yang, J.; Wang, J. Electrochemical intercalation of Mg^{2+} in 3D hierarchically porous magnesium cobalt silicate and its application as an advanced cathode material in rechargeable magnesium batteries. *J. Mater. Chem.* **2011**, *21*, 12437−12443.
(283) Mori, T.; Masese, T.; Orikasa, Y.; Huang, Z.-D.; Okado, T.; Kim, J.; Uchimoto, Y. Anti-site mixing governs the electrochemical performances of olivine-type $MgMnSiO_4$ cathodes for rechargeable magnesium batteries. *Phys. Chem. Chem. Phys.* **2016**, *18*, 13524−13529.
(284) Malik, R.; Burch, D.; Bazant, M.; Ceder, G. Particle Size Dependence of the Ionic Diffusivity. *Nano Lett.* **2010**, *10*, 4123−4127.
(285) Zheng, Y.; NuLi, Y.; Chen, Q.; Wang, Y.; Yang, J.; Wang, J. Magnesium cobalt silicate materials for reversible magnesium ion storage. *Electrochim. Acta* **2012**, *66*, 75−81.
(286) Chen, X.; Bleken, F. L.; Løvvik, O. M.; Vullum-Bruer, F. Comparing electrochemical performance of transition metal silicate cathodes and chevrel phase Mo_6S_8 in the analogous rechargeable Mg-ion battery system. *J. Power Sources* **2016**, *321*, 76−86.
(287) Zhang, R.; Ling, C. Unveil the Chemistry of Olivine $FePO_4$ as Magnesium Battery Cathode. *ACS Appl. Mater. Interfaces* **2016**, *8*, 18018−18026.
(288) Palacios, E.; Leret, P.; Fernández, J.; De Aza, A.; Rodríguez, M. Synthesis of amorphous acid iron phosphate nanoparticles. *J. Nanopart. Res.* **2012**, *14*, 1−7.
(289) Delmas, C.; Nadiri, A.; Soubeyroux, J. The nasicon-type titanium phosphates $ATi_2(PO_4)_3$ (A = Li, Na) as electrode materials. *Solid State Ionics* **1988**, *28*−*30*, 419−423.
(290) Ong, S. P.; Chevrier, V. L.; Hautier, G.; Jain, A.; Moore, C.; Kim, S.; Ma, X.; Ceder, G. Voltage, stability and diffusion barrier differences between sodium-ion and lithium-ion intercalation materials. *Energy Environ. Sci.* **2011**, *4*, 3680−3688.
(291) Shi, J. J.; Yin, G. Q.; Jing, L. M.; Guan, J.; Wu, M. P.; Zhou, Y. L.; Lou, H. L.; Wang, Z. Lithium and sodium diffusion in solid electrolyte materials of $AM_2(PO_4)_3$ (A = Li, Na, M = Ti, Sn and Zr). *Int. J. Mod. Phys. B* **2014**, *28*, 1450176−1−1450176−9.
(292) Kang, J.; Chung, H.; Doh, C.; Kang, B.; Han, B. Integrated study of first principles calculations and experimental measurements for Li-ionic conductivity in Al-doped solid-state $LiGe_2(PO_4)_3$ electrolyte. *J. Power Sources* **2015**, *293*, 11−16.
(293) Goodenough, J.; Hong, H.-P.; Kafalas, J. Fast Na+-ion transport in skeleton structures. *Mater. Res. Bull.* **1976**, *11*, 203−220.
(294) Makino, K.; Katayama, Y.; Miura, T.; Kishi, T. Electrochemical insertion of magnesium to $Mg_{0.5}Ti_2(PO_4)_3$. *J. Power Sources* **2001**, *99*, 66−69.
(295) Makino, K.; Katayama, Y.; Miura, T.; Kishi, T. Magnesium insertion into $Mg_{0.5+y}(Fe_yTi_{1-y})_2(PO_4)_3$. *J. Power Sources* **2001**, *97*−*98*, 512−514.
(296) Makino, K.; Katayama, Y.; Miura, T.; Kishi, T. Preparation and electrochemical magnesium insertion behaviors of $Mg_{0.5+y}(Me_yTi_{1-y})_2(PO_4)_3$ (Me = Cr, Fe). *J. Power Sources* **2002**, *112*, 85−89.
(297) Takahashia, H.; Takamura, H. Ionic Conductivity and Crystal Structure of TM-Doped $Mg_{0.5}Ti_2(PO_4)_3$ (TM = Fe, Mn, Co and Nb). *Key Eng. Mater.* **2012**, *508*, 291−299.
(298) Huang, Z.-D.; Masese, T.; Orikasa, Y.; Mori, T.; Yamamoto, K. Vanadium phosphate as a promising high-voltage magnesium ion (de)-intercalation cathode host. *RSC Adv.* **2015**, *5*, 8598−8603.
(299) Yin, S.-C.; Grondey, H.; Strobel, P.; Anne, M.; Nazar, L. F. Electrochemical Property: Structure Relationships in Monoclinic $Li_{3-y}V_2(PO_4)_3$. *J. Am. Chem. Soc.* **2003**, *125*, 10402−10411.
(300) Anuar, N.; Adnan, S.; Mohamed, N. Characterization of $Mg_{0.5}Zr_2(PO_4)_3$ for potential use as electrolyte in solid state magnesium batteries. *Ceram. Int.* **2014**, *40*, 13719−13727.
(301) Imanaka, N.; Okazaki, Y.; Adachi, G.-y. Divalent magnesium ion conducting characteristics in phosphate based solid electrolyte composites. *J. Mater. Chem.* **2000**, *10*, 1431−1435.
(302) Gautam, G. S.; Canepa, P.; Ceder, G. Mg mobility in NASICON-frameworks. Lawrence Berkeley National Laboratory: Berkeley, CA, Unpublished Work, 2017.
(303) Kamaya, N.; Homma, K.; Yamakawa, Y.; Hirayama, M.; Kanno, R.; Yonemura, M.; Kamiyama, T.; Kato, Y.; Hama, S.; Kawamoto, K.; Mitsui, A. A lithium superionic conductor. *Nat. Mater.* **2011**, *10*, 682−686.
(304) Bachman, J. C.; Muy, S.; Grimaud, A.; Chang, H.-H.; Pour, N.; Lux, S. F.; Paschos, O.; Maglia, F.; Lupart, S.; Lamp, P.; Giordano, L.; Shao-Horn, Y. Inorganic Solid-State Electrolytes for Lithium Batteries: Mechanisms and Properties Governing Ion Conduction. *Chem. Rev.* **2016**, *116*, 140−162.
(305) Huang, Z.-D.; Masese, T.; Orikasa, Y.; Mori, T.; Minato, T.; Tassel, C.; Kobayashi, Y.; Kageyama, H.; Uchimoto, Y. $MgFePO_4F$ as a feasible cathode material for magnesium batteries. *J. Mater. Chem. A* **2014**, *2*, 11578−11582.
(306) Wu, J.; Gao, G.; Wu, G.; Liu, B.; Yang, H.; Zhou, X.; Wang, J. Tavorite-$FeSO_4F$ as a potential cathode material for Mg ion batteries: a first principles calculation. *Phys. Chem. Chem. Phys.* **2014**, *16*, 22974−22978.

DOI: 10.1021/acs.chemrev.6b00614
Chem. Rev. 2017, 117, 4287−4341

(307) Wu, J.; Gao, G.; Wu, G.; Liu, B.; Yang, H.; Zhou, X.; Wang, J. $MgVPO_4F$ as a one-dimensional Mg-ion conductor for Mg ion battery positive electrode: a first principles calculation. *RSC Adv.* **2014**, *4*, 15014−15017.
(308) Sauvage, F.; Laffont, L.; Tarascon, J.-M.; Baudrin, E. Study of the insertion/deinsertion mechanism of sodium into $Na_{0.44}MnO_2$. *Inorg. Chem.* **2007**, *46*, 3289−3294.
(309) Yamada, A.; Iwane, N.; Harada, Y.; Nishimura, S.-i.; Koyama, Y.; Tanaka, I. Lithium Iron Borates as High-Capacity Battery Electrodes. *Adv. Mater.* **2010**, *22*, 3583−3587.
(310) Kim, J. C.; Moore, C. J.; Kang, B.; Hautier, G.; Jain, A.; Ceder, G. Synthesis and Electrochemical Properties of Monoclinic $LiMnBO_3$ as a Li Intercalation Material. *J. Electrochem. Soc.* **2011**, *158*, A309−A315.
(311) Bo, S.-H.; Wang, F.; Janssen, Y.; Zeng, D.; Nam, K.-W.; Xu, W.; Du, L.-S.; Graetz, J.; Yang, X.-Q.; Zhu, Y.; Parise, J. B.; Grey, C. P.; Khalifah, P. G. Degradation and (de)lithiation processes in the high capacity battery material $LiFeBO_3$. *J. Mater. Chem.* **2012**, *22*, 8799−8809.
(312) Bo, S.-H.; Grey, C. P.; Khalifah, P. G. Defect-Tolerant Diffusion Channels for Mg^{2+} Ions in Ribbon-Type Borates: Structural Insights into Potential Battery Cathodes $MgVBO_4$ and $Mg_xFe_{2-x}B_2O_5$. *Chem. Mater.* **2015**, *27*, 4630−4639.
(313) Pasta, M.; Wessells, C. D.; Liu, N.; Nelson, J.; McDowell, M. T.; Huggins, R. A.; Toney, M. F.; Cui, Y. Full open-framework batteries for stationary energy storage. *Nat. Commun.* **2014**, *5*, 3007.
(314) Trócoli, R.; La Mantia, F. An Aqueous Zinc-Ion Battery Based on Copper Hexacyanoferrate. *ChemSusChem* **2015**, *8*, 481−485.
(315) Zhang, L.; Chen, L.; Zhou, X.; Liu, Z. Towards High-Voltage Aqueous Metal-Ion Batteries Beyond 1.5 V: The Zinc/Zinc Hexacyanoferrate System. *Adv. Energy Mater.* **2015**, *5*, 1400930.
(316) Yagi, S.; Fukuda, M.; Ichitsubo, T.; Nitta, K.; Mizumaki, M.; Matsubara, E. EQCM Analysis of Redox Behavior of CuFe Prussian Blue Analog in Mg Battery Electrolytes. *J. Electrochem. Soc.* **2015**, *162*, A2356−A2361.
(317) Reed, L. D.; Ortiz, S. N.; Xiong, M.; Menke, E. J. A rechargeable aluminum-ion battery utilizing a copper hexacyanoferrate cathode in an organic electrolyte. *Chem. Commun.* **2015**, *51*, 14397−14400.
(318) Lipson, A. L.; Pan, B.; Lapidus, S. H.; Liao, C.; Vaughey, J. T.; Ingram, B. J. Rechargeable Ca-Ion Batteries: A New Energy Storage System. *Chem. Mater.* **2015**, *27*, 8442−8447.
(319) Sun, X.; Duffort, V.; Nazar, L. F. Prussian Blue Mg−Li Hybrid Batteries. *Adv. Sci.* **2016**, *3*, 1600044.
(320) Kim, D.-M.; Kim, Y.; Arumugam, D.; Woo, S. W.; Jo, Y. N.; Park, M.-S.; Kim, Y.-J.; Choi, N.-S.; Lee, K. T. Co-intercalation of Mg^{2+} and Na^+ in $Na_{0.69}Fe_2(CN)_6$ as a High-Voltage Cathode for Magnesium Batteries. *ACS Appl. Mater. Interfaces* **2016**, *8*, 8554−8560.
(321) Tojo, T.; Sugiura, Y.; Inada, R.; Sakurai, Y. Reversible Calcium Ion Batteries Using a Dehydrated Prussian Blue Analogue Cathode. *Electrochim. Acta* **2016**, *207*, 22−27.
(322) Ling, C.; Chen, J.; Mizuno, F. First-Principles Study of Alkali and Alkaline Earth Ion Intercalation in Iron Hexacyanoferrate: The Important Role of Ionic Radius. *J. Phys. Chem. C* **2013**, *117*, 21158−21165.
(323) Shiga, T.; Kondo, H.; Kato, Y.; Inoue, M. Insertion of Calcium Ion into Prussian Blue Analogue in Nonaqueous Solutions and Its Application to a Rechargeable Battery with Dual Carriers. *J. Phys. Chem. C* **2015**, *119*, 27946−27953.
(324) Haynes, W. M., Bruno, T. J., Lide, D. R., Eds. *CRC Handbook of Chemistry and Physics*, 96th ed.; CRC Press: Boca Raton, FL, 2016.
(325) Delmas, C.; Fouassier, C.; Hagenmuller, P. Structural classification and properties of the layered oxides. *Physica B+C* **1980**, *99*, 81−85.
(326) Takeuchi, Y.; Nowacki, W. Detailed crystal structure of rhombohedral MoS_2 and systematic deduction of possible polytypes of molybdenite. *Bull. Suisse Mineral. Petrogr.***1964**, *44*, 105−120.
(327) Riekel, C. Structure refinement of $TiSe_2$ by neutron diffraction. *J. Solid State Chem.* **1976**, *17*, 389−392.
(328) Kihlborg, L. Least squares refinement of crystal structure of molybdenum trioxide. *Ark. Kemi* **1963**, *21*, 357−364.
(329) Galy, J.; Duc, F.; Svensson, G.; Baules, P.; Rozier, P.; Millet, P. Stacking disorder in $Mo_{1+x}V_{2-x}O_8$ phase ($0.12 \leq x \leq 0.18$). Solid state chemistry−X−rays-TEM-physical properties. *Solid State Sci.* **2005**, *7*, 726−734.
(330) Knorr, R.; Müller, U. η-Mo_4O_{11} und $Mg_2Mo_3O_8$: eine neue Synthese und Verfeinerung ihrer Kristallstrukturen. *Z. Anorg. Allg. Chem.* **1995**, *621*, 541−545.
(331) Enjalbert, R.; Galy, J. A refinement of the structure of V_2O_5. *Acta Crystallogr., Sect. C: Cryst. Struct. Commun.* **1986**, *42*, 1467−1469.
(332) Rossouw, M. H.; Liles, D. C.; Thackeray, M. M.; David, W. I. F.; Hull, S. Alpha manganese dioxide for lithium batteries: A structural and electrochemical study. *Mater. Res. Bull.* **1992**, *27*, 221−230.
(333) Parant, J.-P.; Olazcuaga, R.; Devalette, M.; Fouassier, C.; Hagenmuller, P. Sur quelques nouvelles phases de formule Na_xMnO_2 ($x \leq 1$. *J. Solid State Chem.* **1971**, *3*, 1−11.
(334) Takeda, T.; Nagata, M.; Kobayashi, H.; Kanno, R.; Kawamoto, Y.; Takano, M.; Kamiyama, T.; Izumi, F.; Sleight, A. W. High-Pressure Synthesis Crystal Structure, and Metal-Semiconductor Transitions in the $Tl_2Ru_2O_{7-\delta}$ Pyrochlore. *J. Solid State Chem.* **1998**, *140*, 182−193.
(335) Nytén, A.; Abouimrane, A.; Armand, M.; Gustafsson, T.; Thomas, J. O. Electrochemical performance of Li_2FeSiO_4 as a new Li-battery cathode material. *Electrochem. Commun.* **2005**, *7*, 156−160.
(336) Gummow, R. J.; Han, G.; Sharma, N.; He, Y. Li_2MnSiO_4 cathodes modified by phosphorous substitution and the structural consequences. *Solid State Ionics* **2014**, *259*, 29−39.
(337) Yamaguchi, H.; Akatsuka, K.; Setoguchi, M.; Takaki, Y. Structure of cobalt dilithium silicate β_{II}-Li_2CoSiO_4. *Acta Crystallogr., Sect. B: Struct. Crystallogr. Cryst. Chem.* **1979**, *35*, 2680−2682.
(338) Streltsov, V. A.; Belokoneva, E. L.; Tsirelson, V. G.; Hansen, N. K. Multipole analysis of the electron density in triphylite, $LiFePO_4$, using X-ray diffraction data. *Acta Crystallogr., Sect. B: Struct. Sci.* **1993**, *49*, 147−153.
(339) Chen, D.; Shao, G.-Q.; Li, B.; Zhao, G.-G.; Li, J.; Liu, J.-H.; Gao, Z.-S.; Zhang, H.-F. Synthesis, crystal structure and electrochemical properties of $LiFePO_4F$ cathode material for Li-ion batteries. *Electrochim. Acta* **2014**, *147*, 663−668.
(340) Barth, S.; Olazcuaga, R.; Gravereau, P.; Le Flem, G.; Hagenmuller, P. $Mg_{0.5}Ti_2(PO_4)_3$−a new member of the NASICON family with low thermal expansion. *Mater. Lett.* **1993**, *16*, 96−101.
(341) Urban, A.; Seo, D.-H.; Ceder, G. Computational understanding of Li-ion batteries. *npj Comput. Mater.* **2016**, *2*, 16002.

DOI: 10.1021/acs.chemrev.6b00614
Chem. Rev. 2017, 117, 4287−4341